A Hybrid Dynamically Adaptive, Super Spatio-Temporal Resolution Digital Particle Image Velocimetry For Multi-Phase Flows

Claude Abiven

Thesis submitted to the Faculty of the Virginia Polytechnic Institute and State University in partial fulfillment of the requirements for the degree of

Master of Science

In

Engineering Mechanics

Demetri P. Telionis, Chair

Pavlos P. Vlachos

Saad A. Ragab

July 2, 2002

Blacksburg, Virginia

Keywords: Digital Particle Image Velocimetry, Digital Particle Tracking Velocimetry, High resolution, High speed, Neural Networks

A Hybrid Dynamically Adaptive, Super Spatio-Temporal Resolution Digital Particle Image Velocimetry For Multi-Phase Flows

Claude Abiven

(ABSTRACT)

A unique, super spatio-temporal resolution Digital Particle Image Velocimetry (DPIV) system with capability of resolving velocities in a multi-phase flow field, using a very sophisticated novel Dynamically Adaptive Hybrid velocity evaluation algorithm has been developed The unique methodology of this powerful system is presented, its specific distinctions are enlightened, confirming its flexibility, and its superior performance is established by comparing it to the most established best DPIV software implementations currently available. Taking advantage of the most recent advances in imaging technology coupled with state of the art image processing tools, high-performing validation schemes including neural networks, as well as a hybrid digital particle tracking velocimeter (DPTV), the foundation for a unique system was developed. The presented software enables one to effectively resolve tremendously demanding flow-fields. The resolution of challenging test cases including high speed cavitating underwater projectiles as well as high pressure spray demonstrate the power of the developed device.

Acknowledgments

In the first place, I would like to express my deepest thanks to Dr Pavlos Vlachos, whose constant support, insightful guidance, knowledge, and encouragements led me throughout the completion of this dissertation. During one year and a half, he certainly made me benefit from his invaluable skills.

I wish to show my gratitude to Dr D. Telionis, who gave me the opportunity to come to study at Virginia Tech, and whose instructive comments greatly improved the quality of my work.

I am grateful to the Personal of the Department of Engineering Science and Mechanics, especially Loretta Tickle for her administrative assistance. I also thank the people from the fluids laboratory for their everyday presence, especially Amber Ali and José, whose kind presences made my stay in Blacksburg more pleasant, both at and out of work. Olga, I will miss you beside me and will cherish this part of the way we shared.

Very special thanks are due to Katja and Mario whose intense support and presence enlightened my semesters in Virginia Tech, along with sharing out of time instants. I shall never forget your friendship.

I am also very thankful for having such great friends as Ronan, Manu, JP, Virginie, Laurent, Alex, Kat, William and all the others. It is probably taken away from people that we realize how significant they are in our life.

I also would like to thank my family, especially my grandparents, aunt, parents, sisters, and brother, for their affection, support, and understanding throughout all these years of studies.

I will remember all these factors that made my journey delightful or distasteful, but certainly unforgettable, as well as all those with whom I happened to share a moment, a laugh, or simply a look or a smile.

To my little German girl…

Va revoir les roses. Tu

comprendras que la tienne

est unique au monde parce

qu'elle t'a apprivoisé

ANTOINE DE ST-EXUPÉRY

Table of contents

List of figures

List of Tables

Chapter 1 Introduction

During the past decade, the field of experimental fluid mechanics has been revolutionized by the emergence of Digital Particle Image Velocimetry (DPIV), a non-intrusive method that provides time- resolved velocity measurements in a plane. The method is based on the mapping of the flow field by determining the displacement of tracer-particle images during a sequence of consecutive frames. The principal strength of the method is its ability to perform spatial correlations and to analyze spatially developing flows.

This chapter contains basic principles of DPIV (Digital Particle Image Velocimetry) and DPTV (Digital Particle Tracking Velocimetry) methods, devoted to the unfamiliar readers that will be presented in the general overview. The subsequent paragraphs will discuss more advanced features, focusing on the advantages of the schemes proposed in the literature, along with their drawbacks, some of which will be tackled during the present effort.

1.1 General overview

1.1.1 Main idea of DPIV and DPTV

When a log of wood is seen floating on the surface of a creek, its speed can be more or less related to the one of the creek at the point where the log happens to be. DPIV and DPTV use this simple observation in order to assess to the velocity components of a flow. The flow is seeded with small particles the density of which is approximately equal to the one of the fluid so as to accurately respond to flow fluctuations. These particles, when properly illuminated, scatter light in all directions, which is detectable and can be use in order to tag the fluid motion.

Images of the seeded flow are then captured successively within very short time intervals such that most of the particles that appear in one frame still appear in the

following. Measuring the displacement of one particle from one frame to the other results to its velocity assuming that we know the time-separation between two frames. Two prevailing ways of resolving this displacement have been developed: DPIV and DPTV.

1.1.2 Digital images

DPIV applications now typically use digital imaging technology, for the reason that it is possible to acquire and store them in a computer in real-time, in addition to easily transform them. Digital images are characterized by their intensity pixel values corresponding to the ones given by the camera sensors. One pixel thus defines the smallest element of a digital image. In DPIV, images are usually coded in values of gray, each pixel taking a value between 0 and 255, 0 corresponding to the minimum amount of light received by a sensor (black pixel), and 255 to the maximum (white pixel).

1.1.3 Digital Particle Image Velocimetry

In DPIV, the image is divided into small subdivisions (usually square sections like 32x32 pixels) called interrogation windows. Each subdivision is then processed independently, delivering an individual displacement evaluation. Therefore, the resulting number of velocity vectors that one obtains out of the method depends on the number and size of the interrogation windows that can fit in the recorded image, as well as on the distance between these windows, which can eventually overlap each other in order to increase their population. Figure 1.1 shows on its left an image broken down into four square interrogation windows, generating four displacement estimations. The right top part of the figure shows a window (blue) inserted between two black ones, 50 percent of the blue window being already probed by the first black window. If the same overlapping is repeated for both vertical and horizontal axes, 9 velocities are obtained for the measurement areas centered on the dots shown on the bottom right of the figure.

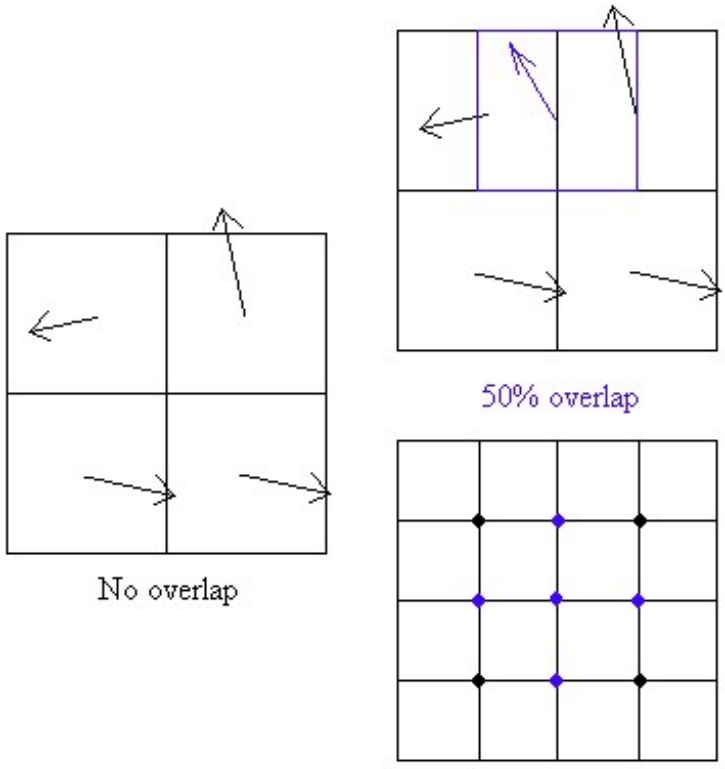

Figure1.1: Interrogation windows overlapping

In order to get a displacement out of each interrogation window, a process called cross-correlation takes place. It is a mathematical operation that is generally implemented in the Fourier domain for reasons of computational efficiency. Figure 1.2 illustrates this process. Considering the top gray windows of each frame, the cross-correlation can be viewed as the best way to superimpose the two images by horizontal and vertical translation so that the largest pattern of particles (in blue) appears in both images. The distance from which the windows are apart from each other thus gives the displacement of the pattern of particles from one frame to the other.

In practice, things are not that simple. Indeed, particles are moving in and out of a frame while particles within the same window can have diverse velocities. Also, particles might appear differently from one frame to the other in terms of light intensity or shape. The combination of all these phenomena coupled with noise constitutes a random process that prohibits a deterministic evaluation of the flow field.

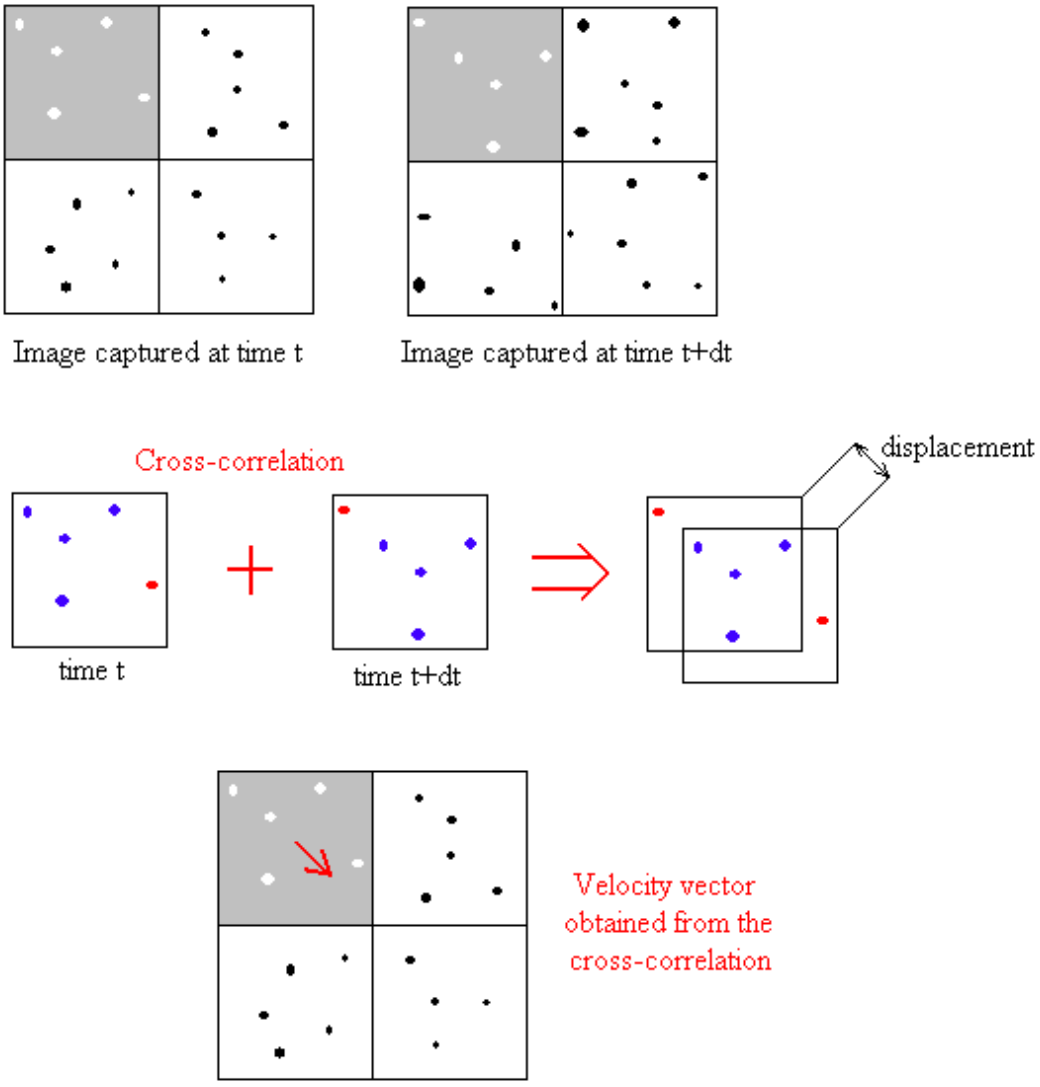

Figure1.2: Cross-correlation procedure

1.1.4 Digital Particle Tracking Velocimetry, Hybrid DPTV

DPTV stands for Digital Particle Tracking Velocimetry. It differs from DPIV in the sense that instead of trying to find the displacements using clusters of particles, each particle form the first frame is identified, and directly matched with the corresponding particle in the second frame. This can be done using size, shape, brightness, or closeness criteria for particle differentiation and identification. The corresponding displacement then simply is the difference of position of the particle between the two frames. The

drawback of DPTV clearly is the difficulty to distinguish one particle among the others. On the other hand, its advantage is its ability to resolve different velocities from one particle to another no matter how close they are to each other, while two close particles with dissimilar velocities will not be distinguishable by the DPIV. DPIV results can be used by the DPTV in order to facilitate the search task, in a procedure called Hybrid DPTV.

1.1.5 Typical arrangement of the experimental setup

Both DPIV and DPTV use digital images as an input. A usual experimental setup enabling one to capture these images is presented in figure 1.3.

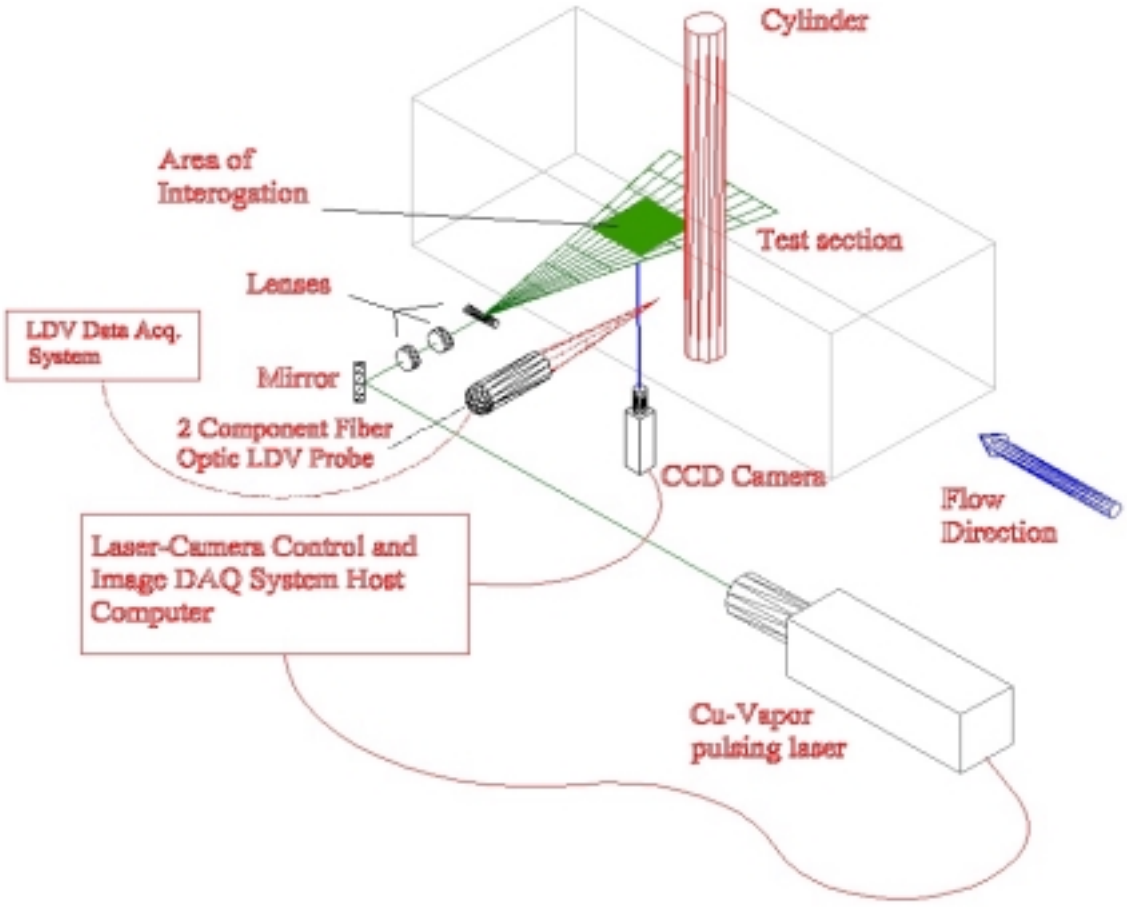

Figure1.3: General overview of an experimental setup

In the present case, the object of the study was the wake of the flow behind a cylinder. The flow was seeded with particles (usually 10 to 100 micro-meters hollow glass spheres with a density close to the density of water). These particles were illuminated by a thin sheet of light, created by a laser beam going through specific optics. Images of the particles within the flow were then captured using a digital camera. Details of the experimental parameters can be found in Vlachos et el. (1998)

1.1.6 Example: flow over a cylinder

The following set of velocity distributions in the flow-field illustrate what has been discussed earlier. Both images were obtained in the wake of a circular cylinder, using the experimental setup described above (wake of a cylinder).

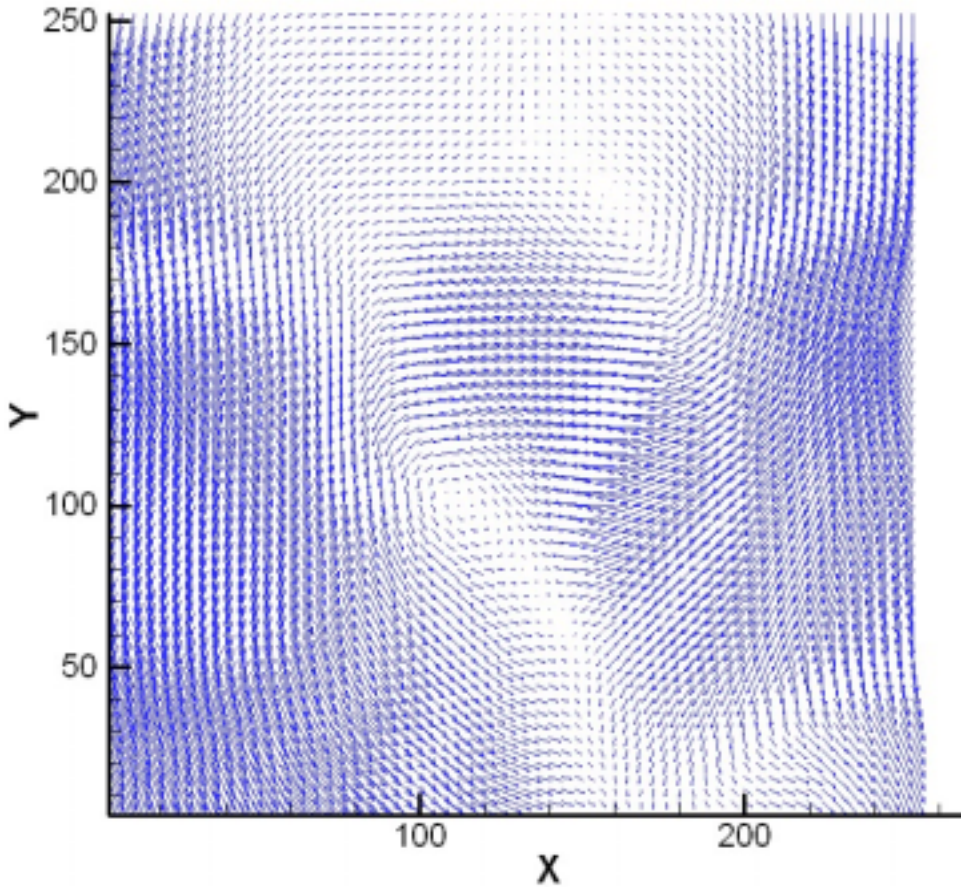

Figure1.4: DPIV (32x32 to 16x16 px windows, after smoothing)

Figure 1.4 was obtained through DPIV evaluation, while the second one was obtained using Hybrid DPTV.In this image, vortical structures (so-called Von Karman vortex street) are clearly visible. The velocity vectors have gone through a post-processing scheme involving validation, interpolation, and smoothing of the data. These features will be described later on in this work. They refine the results of the cross-correlation.

Figure 1.5 represents the same flow but treated using the Hybrid DPTV scheme. Because a velocity is found at each point where a particle is identified, velocity vectors are randomly located throughout the whole flow-field.

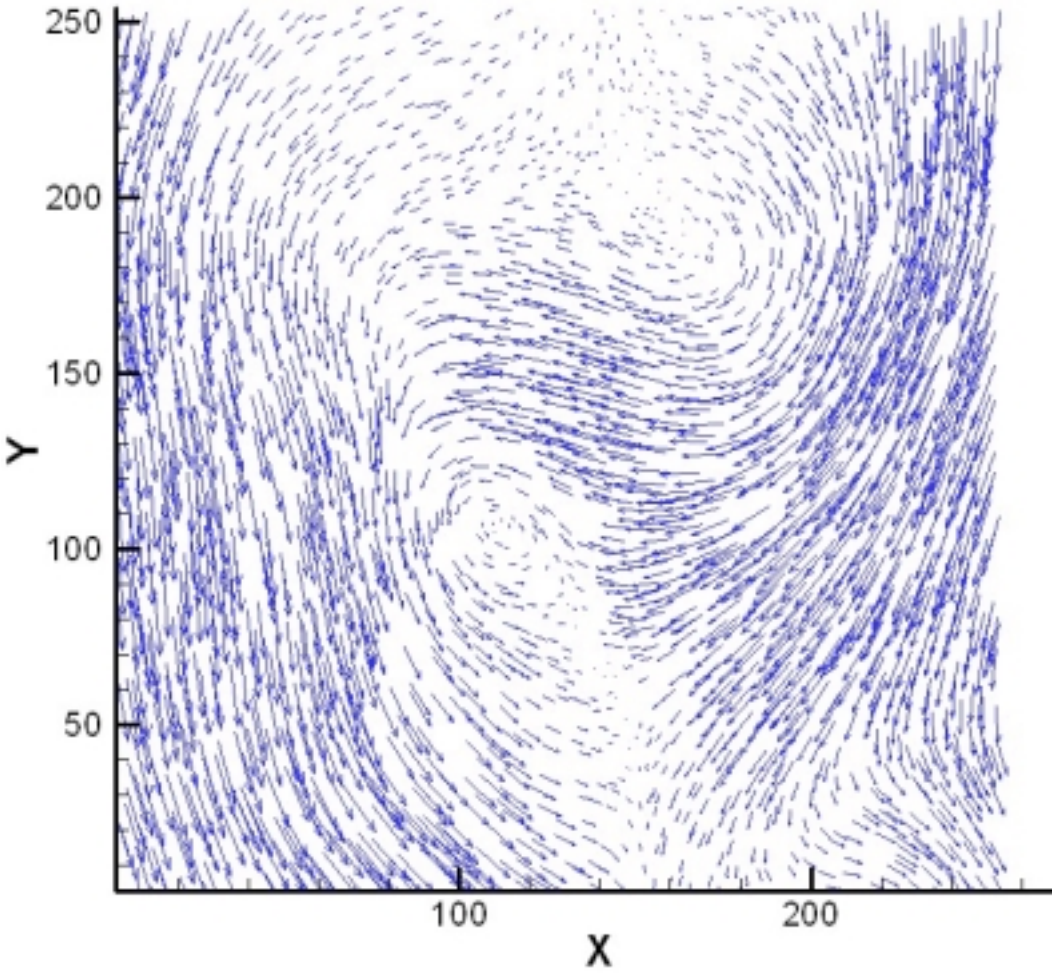

Figure1.5: Hybrid DPTV

1.2 Previous work and objectives

1.2.1 Traditional DPIV implementation

The origin of the method goes back to traditional qualitative particle-flow visualizations, however the early work of Meynard (1983) established the foundations of its present form. During the past two decades, numerous publications have appeared which present improvements on the technique as well as applications of the method to a wide range of flows, varying from low-speed liquid and two-phase flows to supersonic gas flows (Hasselinc, 1988; Adrian, 1991, 1996; Grant, 1994, 1997). It was the work of Willert and Gharib (1991), Westerweel (1993a,b), and Huang and Gharib (1997) that established the digital implementation of PIV, where the photographic film is replaced with a CCD camera. In addition, Particle Tracking Velocimetry falls in the same general category of particle-based techniques, which use a pulsed light source. In their basic implementations, both methods are limited to two-dimensional velocity measurements, but they can be extended to three dimensions (Dracos and Gruen, 1998; Hinsch and Hinrichs, 1996; Adrian et. al., 1995; Prasad and Adrian, 1993; Adrian, 1996). PIV and PTV are similar methods as they are both based on the same principle. The velocity is determined from the displacement of particles within a fixed time interval. Their basic differences are: a) in PIV, the time step is determined by the pulsing frequency of the illumination source, while in PTV, it is determined either by the frame rate of the camera used or by the number of pulses per frame for single-frame particle tracking; and b) most importantly, the PTV requires low-particle concentration so that there is no overlap between particle-image displacements (Dalziel, 1993; Perkings and Hunt, 1989). These two considerations limit the PTV to lower flow speeds and result in a smaller density of velocity vectors in comparison with the PIV. Furthermore, for single-frame particle tracking, using multiple exposures per frame requires resolution of the directional ambiguity. In contrast, conventional PIV algorithms are based on cross-correlations performed using the FFT (as illustrated in figure 1.6), which limit the application of the method in cases where multiple phases coexist.

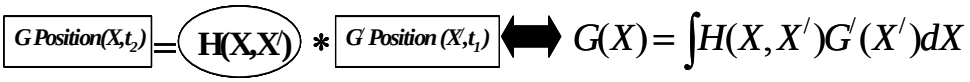

Convolution-De-convolution corresponds to
simple multiplication-division in the Fourier domain:

$$G(X) = H(X,X') * G(X') <=> \hat{G}(X) = \hat{H}(X,X')\hat{G}(X')$$

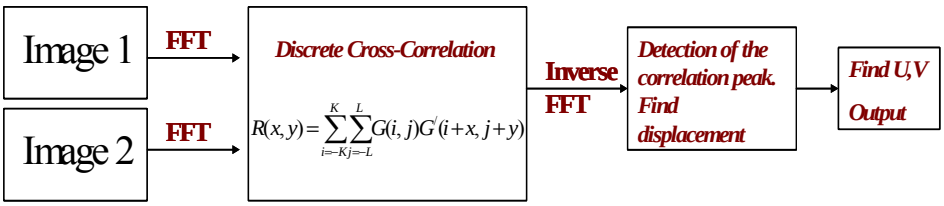

Figure1.6: A schematic representation of the statistical cross-correlation procedure for the evaluation of the velocity vectors

The most common implementation of the method (currently commercially available) focuses on a single-exposure double-frame digital cross-correlation approach. A CDD camera with high resolution (1Kx1K pixels) that can sample with up to 30 fps resulting in a 15Hz sampling frequency of the flow field is synchronized with a Nd:YAG pulsing laser, which illuminates the interrogation area. These cameras, the so-called "cross-correlation" CCD cameras, have enhanced the ability of investigating, high-speed flow fields by acquiring two fields per frame (frame straddling), separated only by a few nanoseconds (~100ns). Thus, an approach of dual-frame single-exposure cross-correlation of two consecutive frames became the most popular approach to carry out DPIV measurements. The velocity field is traditionally treated as a linear transfer function that corresponds to a flow-pattern displacement between two consecutive images. This transfer function is revealed in a statistical manner incorporating second-order statistical moments of the image patterns (Westerweel, 1993a, 1997). Therefore, a statistical cross-correlation between the particle image patterns of two successive images is performed in order to calculate the velocity field. A typical cross-correlation implementation of the velocity evaluation algorithm will result in a spatial resolution of

one vector every 16 pixels with an uncertainty of the velocity evaluation of the order of 0.1 pixels.

1.2.2 High Sample Rate Digital Cameras: CMOS versus CCD

The advantages of this approach can be summarized as follows. The use of YAG lasers provides a high-energy/pulse (>100mJoules/pulse) light source with good coherence and intensity profile. The CCD camera has a signal to noise ratio superior to that of the standard photographic film, eliminates the intermediate digitization step, and takes advantage of a fully computer-based data acquisition system. A photographic film, however, still delivers unsurpassed spatial resolution and is able to cover up to three decades of the turbulence spectrum. The most impressive results resolve a 1 m^2 area with 300 microns spatial resolution (Adrian, 1996). In addition, the accuracy of the method is greatly affected by the particle density and image size. The minimum particle-image density needs to be about five pairs of particles per window of interrogation, while the optimum particle-image diameter is approximately 1.5~2.5 pixels. The optimization of the particle-image diameter and the seeding density will increase the signal to noise ratio during the cross-correlation evaluation of the velocities (Willert and Gharib, 1991; Keane and Adrian, 1990, 1991).

A major disadvantage of this approach is its inability to provide sufficient frequency resolution, which is necessary to investigate high-frequency phenomena, which might occur in turbulent flows. This is the major limitation of the DPIV systems that are commercially available. In the system developed by the fluids group of Virginia Tech, the difficulty of high sampling frequency is overcome. The effort was directed towards the integration of a high-power pulsing laser with special type of optics and a CMOS area-scan camera, capable of acquiring over 1000 frames per sec (fps). The result is a DPIV system with a 10 KHz maximum sampling frequency.

Unfortunately, there is very limited work addressing issues arising from the use of high-speed digital cameras (above 500 fps). These cameras are somewhat different in the sense that the time interval between two consecutive frames and the transfer rate are

fixed. These two parameters effectively establish the feasible frame rate. Subsequently, the maximum possible frame rate affects the maximum velocities that can be measured. On the other hand, the increase in the frame rate results in a significant decrease in the exposure of the sensor, which limits the density of particles in the acquired images. Adrian (1996, 1997) provided an analysis of different approaches to adjust the speed and resolution of a PIV system. Multiple exposures per frame for the auto-correlation implementation of the PIV have been studied extensively (Keane and Adrian, 1990, 1991) and a procedure for optimizing the pulse separation has been proposed (Boilot and Prasad, 1996). One paradigm of multiple exposures per frame cross-correlation approach was performed by Cenedese and Paglialuga (1990). However they used an analog low-speed camera. Moreover, instead of performing a cross-correlation of the particle patterns to determine the displacement, they initially determined the centroids of the particles and then cross-correlated the projections of these centroids in each direction.

Conventional DPIV systems employ CCD cameras, which suffer from leakage effects. Namely, the excessive charge from overexposed pixels leaks to the neighboring ones saturating the whole area. In contrast, a CMOS sensor will isolate the individual pixels behaving as a cut-off filter without leaking the energy. Therefore, by employing CMOS technology we eliminate the blooming effect, allowing resolution of a multi-phase flow with direct imaging within a laser sheet. This feature is of great importance since it simplifies the experimental setup, it enhances the signal-to-noise ratio, and more importantly could allow accurate shape and size quantification of droplets or bubbles present in the flow. In addition, it improves the performance of the three-point centroid gaussian estimator, as it will be explained in the paragraphs related to the hybrid particle tracking methodology.

The quantitative flow visualization methodology that is presented in this effort is the first to fully implement CMOS technology and take advantage of the enhanced capabilities that it delivers.

1.2.3 Multiphase flow

Although Digital Particle Image Velocimetry (DPIV) is the most established global flow field measurement technique, time-resolved measurements with simultaneous velocity, shape and size characterization of multiple phases remains a great challenge. Major limitations stem from the fact that conventional DPIV systems employ low-frame rate CCD cameras that are insufficient for resolving the intrinsic time-dependent flow characteristics. Leakage effects significantly compromise the signal-to-noise ratio of the recorded images. For multi-phase flows, saturation of the image from overexposure of bubbles or droplets is a prohibitive parameter for carrying out accurate quantitative measurements. Finally, high-frame-rate cameras are limited by reduced spatial resolution, (~128x128 pixels), while the maximum measurable velocities greatly depend upon the frame rate. These limitations are very often accounted for by employing complex experimental setups.

Previous implementation of time-resolved systems employed digital sensors with limited resolution (Whydrew et al ,1999) or drum cameras that are limited both in recording times as well as frame rate (Lecordier and Trinite, 1999). Previous work by Vlachos (2000) presented a fully digital system, which however was limited to 1KHz sampling rate and 256x256 pixel resolution. Recent work by Upatnieks et al (2002) presented an analog based kilohertz frame rate PIV system capable of recording up to 4000 fps with 8000 frames per sec (fps). By employing analog recording the system delivers superior spatial resolution (>1Kx1K), however due to the fact that such high frame rates require extreme rotation speed for the film, the registration of the images is compromised by film alignment errors that are added on the common digitization errors.

The system presented in the scope of this work delivers a sampling frequency between 1KHz and 10KHz, with a total acquisition time up to 4 secs and resolution 1Kx1K pixels down to 256x256 pixels.

1.2.4 Image processing tools

Taking advantage of the unique capabilities of the imaging sensor, image pre-processing tools were developed to allow direct phase separation within the flow. Khalitov and Longmire (2002) presented an image-based approach for resolving two-phase flows between a flow tracer and a solid phase. In the present work the image processing methodologies were advanced in order to address cases where poly-dispersed distributions of gas-bubbles, solids and/or liquids coexist in the flow. In order to develop a flexible and versatile method capable of tackling complicated multi-phase flows, a wide variety of image pre-processing tools were developed, such as dynamic thresholding, Gaussian smoothing, Laplacian edge detection, filtering, erosion, multiple masking operations and many more, as it will be explained in the chapter relative to methods and facilities.

1.2.5 Dynamically Adaptive DPIV method

A velocity evaluation method for multiphase flows is developed, based on a hybrid scheme that integrates a dynamically adaptive cross-correlation method with a particle tracking velocimetry algorithm. Each phase present in the flow is processed independently, using a multi-pass dynamically adaptive algorithm.

One of the innovations of the present work resulted from the fact that for the analysis of polydispersed multi-phase flows, we have to account for the presence of multiple length scales. Very often the interrogation window will contain a large-scale droplets or bubbles, which in effect will compromise the cross-correlation resulting in erroneous vectors. In order to preserve the advantages of the adaptive algorithm without affecting the quality of the resulting velocity measurements, an improved adaptive cross-correlation scheme optimized towards multi-phase flows was developed.

1.2.5.1. Dynamic windowing

In order to satisfy the Nyquist frequency criterion, a displacement has to be smaller than one-half the length of the interrogation window in order to alleviate aliasing

effects.. However previous work (Keane and Adrian, 1990) illustrated that the statistical cross correlation velocity evaluation has the maximum confidence levels when the displacement is less than one fourth of the interrogation window size. This is illustrated by figure 1.7.

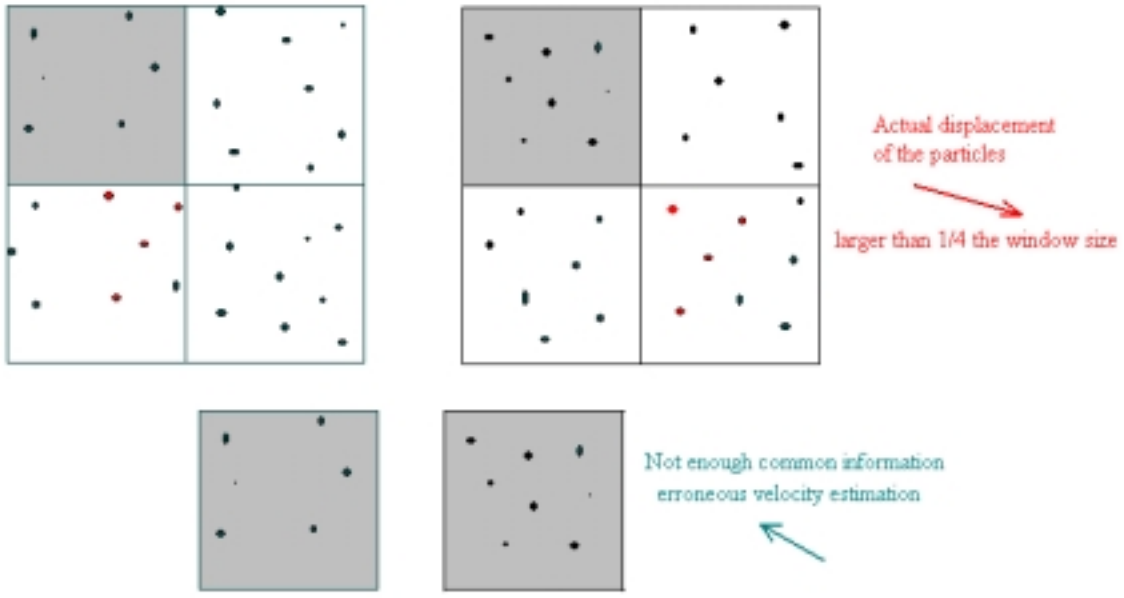

Figure1.7: Illustration of the one fourth rule.

Traditionally, iterative multigrid DPIV employs a first cross-correlation pass in order to generate an initial predictor of the velocity-field. Subsequently, the size of the interrogation window is dynamically allocated, based on the previous step results (Scarano & Rieuthmuller, 1999) as shown by figure 1.8.

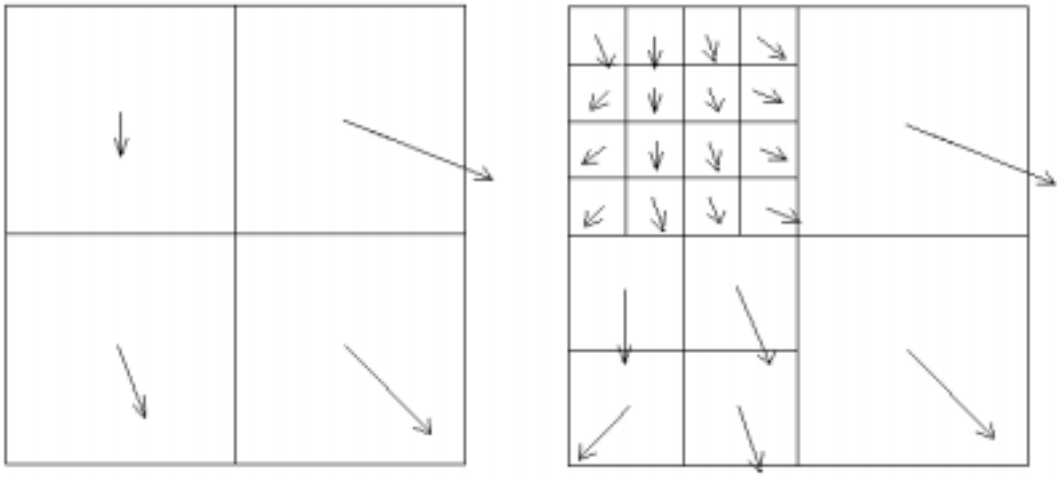

Figure1.8: Window break

Each original window is thus broken down into several windows, the size of which depends on the velocity obtained from the first pass.

1.2.5.2. Dynamic window offset

The window offset feature (Westerweel, 1997) represents a real breakthrough in DPIV, significantly improving the method, as it will be shown later. Taking advantage of a rough velocity flow field determined in a first pass, a second pass is applied shifting the interrogation window in the second image by the displacement found during the first pass. While the first pass was subject to particles going in and out of the interrogation area, the second pass dramatically reduces this effect, as illustrated by the figure 1.9. The top part of this figure represents the first cross-correlation that takes place, giving an initialization of the particle displacement, subject to random motion as illustrated by the presence of one particle that enters the gray square and another one that leaves it during the time dt. The second cross-correlation pass after shifting the second image interrogation window by the previously estimated displacement results in a more accurate velocity evaluation, since the same particles are now present in both gray squares (bottom of the figure).

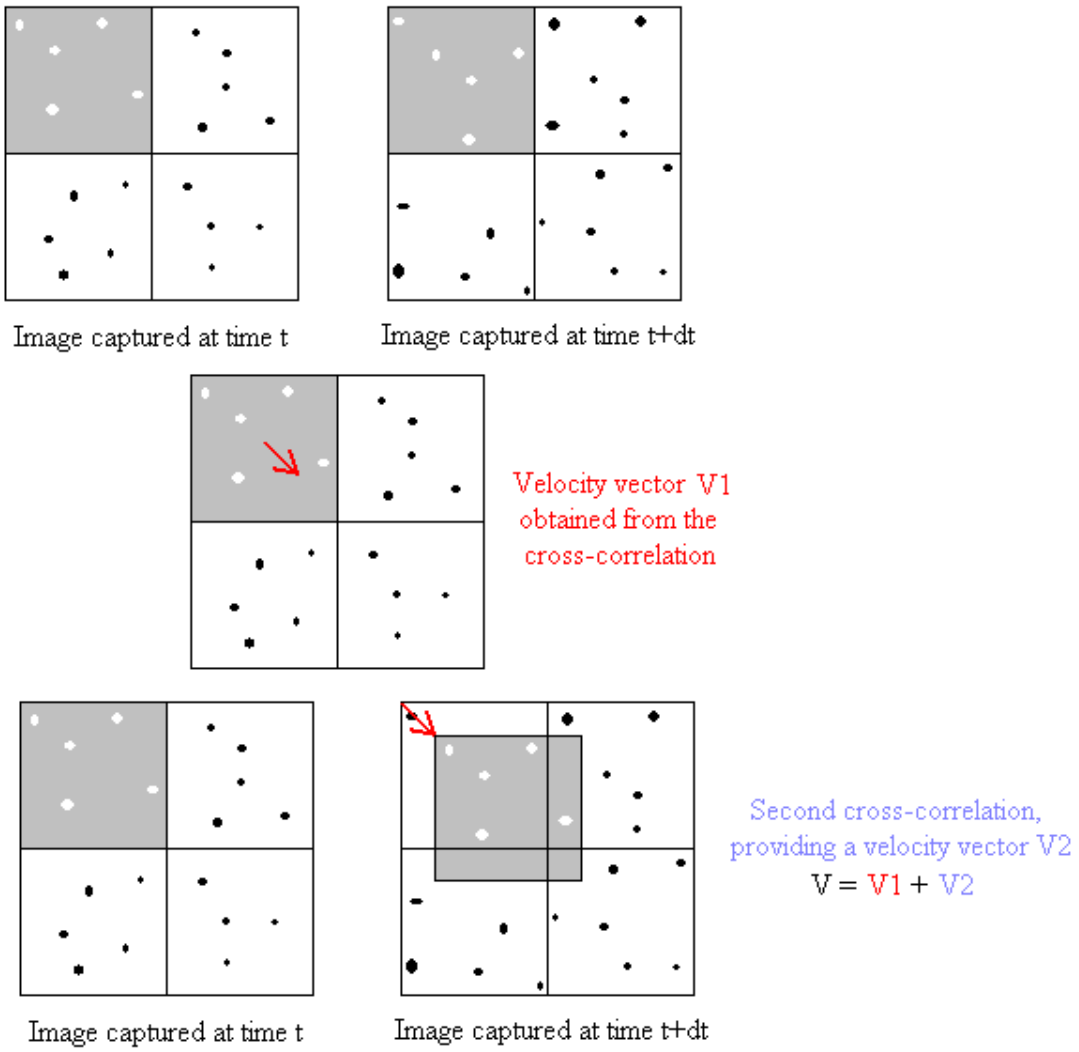

Figure1.9: Dynamic window offset

The second cross-correlation thus is preformed between two windows that contain particles that are more likely to be the same. Therefore, the signal to noise is drastically increased during this operation. In presence of large velocities or large velocity gradients the velocity evaluation is independent from the one-fourth rule. As a result, the velocity is resolved at points defined by the minimum interrogation window size and the maximum allowable window offset. The iterative nature of this process significantly reduces the spatial averaging effects, improving resolution and accuracy of system.

1.2.5.3. Drawbacks of conventional implementations

Both dynamic window offset and dynamic windowing were implemented during this effort. One of the major drawbacks of the window offset feature is that any incorrect evaluation of the velocity during the first pass inescapably leads to erroneous velocity estimations for any velocity vector that was computed using this velocity offset. Indeed the steps subsequent to the first pass refine the velocity evaluation assuming that it was originally properly evaluated. Two original approaches to overcome this problem were developed. The first one is minimizing the effect of the erroneous offset by using a specific offset for each sub-window, and the second is checking the validity of the offset.

1.2.6 Hybrid particle tracking method

1.2.6.1. Particle detection

Every particle detection scheme takes advantage of image processing tools. A clean image that ensures proper particle detection significantly affects the particle tracking performance.

Guezennec and Kiritsis (1990) proposed a method to ensure the particle detection. It consists in examining each pixel of the image line by line. For each pixel above a certain threshold, its eight neighbors are recursively examined. If they don't belong to any particle, a new particle number is assigned to the pixel. If they belong to a previously identified particle, the current pixel is added to the list. In some cases, the neighbor pixels belong to two different particles. In this last case, the "two" particles are actually one, and need to be reconnected. All the pixels belonging to one of them have thus to be assigned to the other, as well as the current pixel. This algorithm links each pixel of the image to a particle.

In the scope of this work, this algorithm is significantly improved, accounting for overlapping or neighboring particles that would appear as one if conventional processing were used.

1.2.6.2. Particle pairing

Since the work by Guezennec and Kiritsis (1990), DPTV is tightly related to DPIV, using the results from the cross-correlation in order to initialize the hybrid particle-tracking scheme. Indeed, based on the results from the cross-correlation, estimating the displacement of each particle (from frame one) is straightforward, leading to the expected position of the particle in the second frame, and considerably narrowing the radius of search for each particle pairing. This scheme usually ensures the pairing of most of the particles present in the flow.

An enhancement was proposed by Cowen and Monismith (1997) who suggested to correlate a window centered on each remaining particle (in frame one) with another one centered at the expected particle location (in frame two) before checking if the result of this correlation would lead to a corresponding close enough particle in the second frame.

Taking advantage of the cross-correlation methodologies developed for the DPIV, a method similar to the one by Cowen and Monismith is proposed, avoiding any interpolation in order to estimate the velocity of the particles, an issue common to every DPTV scheme.

Chapter 2 Methods and facilities

In this chapter, the methods and facilities employed during the realization of this work are presented. It includes the hardware components involved in the test cases, the way artificial images are generated, a description of the image processing techniques employed all along this effort, and an explanation of the statistical analyses used to validate the software's performance.

2.1 Hardware facilities

2.1.1 Hardware components

The following provides a basic description of all the basic hardware components involved in the experimental test cases.

Copper Vapor Laser: High frequency, high-power laser: This laser was the workhorse of the DPIV system developed in the ESM Fluid Mechanics Laboratory. This is a copper vapor 55-Watt pulsing laser with nominal range of operation of the laser is at 10KHz. However, the repetition rate is controllable using an external signal. Previous work performed by member of our group (Vlachos 2000) with the collaboration of the laser manufacturing company resulted to a customization of the pulse generation components of the laser extending the range of operation from 100 Hz to 30 KHz. Near its operational limits, the laser experiences power loses. At a frequency of 10KHz (nominal frequency) the power output per pulse is in the order of 5mJ. This number is low compared with the low frequency Nd:YAG lasers that are commonly used.

Phantom IV CMOS 512Kx512K-30000 fps Digital Camera: Two of these cameras are currently available to the Virginia Tech Fluid Mechanics Laboratory. The second camera provides color capabilities. It is the first commercially available optical sensor based on CMOS-technology that delivers repetition rates up to 1000 fps with full frame and up to 30,000 fps with reduced image format. In addition, it is more sensitive and eliminates entirely the leakage effect of conventional CCD sensors increasing the

signal to noise ratio by almost two orders of magnitude. More specifically, this camera delivers 100,000:1 blooming ratio with no pixel-to-pixel spill over. In other words, the saturation of the CCD sensor that results from over exposure or from illumination of droplets or bubbles is entirely eliminated. The sensitivity of the sensor is quantified with the following equivalent ASA rating: with 0 contrast and 0 illumination the camera scores an amazing 800ASA. This translates to a very important feature. The increase of the frame rate results into a significant reduction of the light allowed on the surface of the sensor. However, this is no longer an important problem since the sensitivity of the camera compensates for the reduced illumination as well as for the low energy output of the Cu-Vapor laser. These unique capabilities of the camera are essential to allow PIV measurements and droplet/bubble sizing with such high sampling frequency.

Phantom V CMOS 1Kx1K-60000 fps Digital Camera: This is the current state of the art camera, the generation after Phantom-IV. Delivers identical imaging capabilities as the previous version with the additional advantage that it increases the spatial resolution by a factor of four and doubles the maximum frame rate. It also delivers shorter exposure time, thus higher sensitivity and faster image buffer transfer rate. This camera was on loan from the manufacturing company for a short period of time during which it was used to carry out part of the two-phase flow experiments that serve as test cases of the system under development.

D/A timer controllers: Two Digital/Analog Input Output boards will be used during this project. A Computer Boards PCI-CTR05 timer counter board that provides five independent counters with TTL signals and time resolution of 100nsec. Second, a National Instruments multifunctional board that provides two counters, analog inputs and outputs, and most importantly time resolution down to 50nsecs. The later is the primary board on which the data acquisition control scheme was developed developed.

Three Image processing and data reduction workstations: high-end PC's were used as workstations to provide the computer processing capabilities necessary.

Camera Lenses: Four different types of lenses are available:(1) Schneider 25mm wide-angle lens with a continuously variable *f#* down to 0.95. (2) Nikkon 55mm lens with *f#* 1.2 (3) Nikkon 80-300mm telephoto lens with *f#* 2.8. (4) Nikkon 16-100mm *f#* 1.9.

2.1.2 Hardware integration

In order to perform accurate DPIV measurements it is essential to synchronize the laser with the cameras. The current system configuration successfully integrates the laser with the camera and accurately synchronizes the two with timing uncertainty in the order of +/-25nsecs. DPIV data acquisition with kilohertz sampling rate requires accurate timing. The use of the multifunctional data acquisition board allows not only the control of the systems, but also the recording of feedback signals that will monitor and document the timing-synchronization data acquisition process. Figure 2.1 illustrates the complete

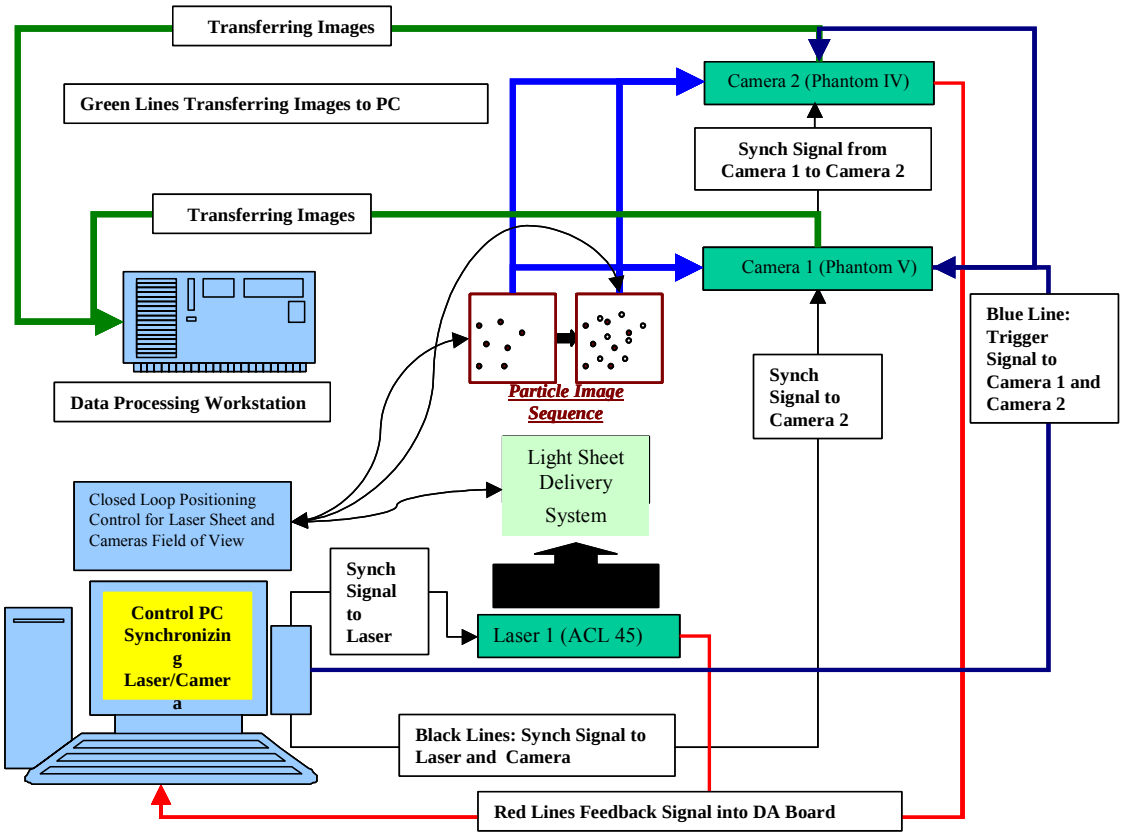

Figure 2.1: Hardware integration

generic data acquisition and control scheme layout incorporating two cameras and all the additional components necessary to carry out high speed, stereo DPIV measurements, including triggering and feedback signals.

2.2 Image processing tools

Image pre-processing tools were integrated in the software to enhance its capabilities. Namely, basic image processing functions, standard and local dynamic thresholds, sharpening, smoothing, edge detection, Gaussian and Laplacian filters, erosion, masking and wavelet image decomposition are integrated in the overall package. These functions facilitate the pre-processing of the images in order to remove background noise, unwanted reflections and increase the signal to noise ratio. In addition these functions are designed in a "user-programmable" way to allow the user to develop its own scripts thus customizing the application. Moreover these functions carry the load of determining the phase's present and decomposing the images, thus allowing the determination of the velocities of the different phases present in the flow as well as their shape and size.

Image pre-processing tools are developed to allow direct phase separation within the flow and subsequent processing of each individual phase separately. In order to develop a flexible and versatile method capable of tackling complicated multi-phase flows, a wide variety of image pre-processing tools such as local dynamic thresholds, Gaussian blur smoothing, Laplacian of Gaussian (LoG) edge detection filtering, erosion, multiple masking operations and many more were developed. The software developed allows the user to define in real time the sequence of function calls and generate scripts for carrying out the operations. Any combination of all the available functions in any order and with any number of iteration is possible.

Apparently, different experimental parameters would result into different image properties. Therefore there is no unique combination of image processing operation that would perform sufficiently for all cases. The present work aims at addressing poly-dispersed distribution of bubbles, droplets or solids in the carrying phase. Therefore the

image-based phase separation needs to be dynamically adaptive to the temporal and spatial changes of the recorded images. In the following paragraphs we will describe only the most important of these operations used in one suggested processing scenario that serves to separate the different phases and store them in individual images that will be processed independently. It is important to note that the image processing function is taking advantage of the capabilities of the CMOS imaging sensor in order to accurately determine the boundaries of droplets or bubbles, as well the size and distribution of the flow tracers.

2.2.1 Usual image processing tools

The full discussion of the image processing tools used is beyond the scope of this work. Image processing remains a vast issue. Researchers have spent years in order to develop and improve an arsenal of image processing strategies. The present work uses most of them as ready to use utensils. Tools commonly used with Particle Image Velocimetry methods developed during this effort are referenced below.

- ***Binarization:*** assign to 0 pixels under a certain pixel, and 1 to others.
- ***Threshold:*** removes every intensity pixel under a certain threshold.
- ***Dynamic threshold:*** automatically applies local thresholds to 3x3 squares based on the pixel values inside the square.
- ***Erosion:*** removes boundaries of objects pixel layer by layer leaving single pixels center of the object at the end of the erosion process.
- ***Filters3x3:*** modifies pixels inside a 3x3 square in terms of the 9 considered pixel values.
- ***Logical and basic operations:*** AND, OR, addition, subtraction...
- **Maximum:** detects local maximums.

The aforementioned tools are very customary in image processing, and were implemented following the methods by Jahne (Image Processing for Scientific Applications 1991 and 1997).

A general algorithm that segregates the different phase within the flow is presented in the following paragraphs. Although each particular case needs to be processed specifically, the subsequent scheme can be viewed as a starting point from which the user can add or remove image-processing operations in order to tackle each flow's specificity. It consists in cleaning the image using thresholds, before applying smoothing and edge detection in order to separate the phases in the flow, and eventually tracking the resulting particles using a particle segmentation method.

2.2.2 Thresholding

2.2.2.1. Histogram based thresholding

Background noise is a significant issue in both DPIV and DPTV. In the case of DPIV, it mingles with the signal (particles) and contributes to inaccurate estimations of the actual cross-correlation peak. In the case of DPTV, confusing noise and particles can result in pairing imaginary particles, ensuing erroneous velocity estimations. Therefore, a specific and original image-processing tool, namely histogramming, was developed during the present effort in order to dynamically cope with background noise.

Considering images of a seeded flow-field coded in values of gray, one can plot its histogram, that is, the number of realizations of each value of gray over the whole image. As shown below, background noise generally appears as a peak in the low intensity values of the histogram.

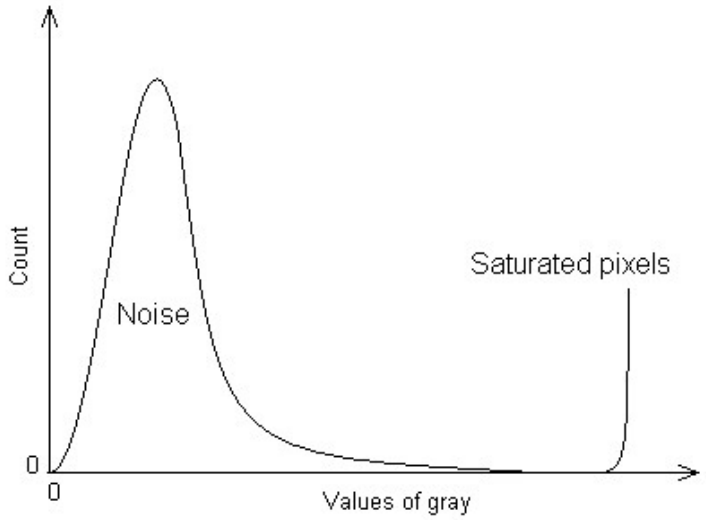

Figure 2.2: Standard histogram obtained with a DPIV image

Consequently, after such a histogram has been computed by scanning each image's pixel, the noise peak can be easily evaluated, as well as the value of gray for which the peak's slope is small enough and corresponds to the background noise level. A threshold can then be performed, followed by a second histogramming and so on until the peak level reaches a satisfying value. As it will be seen in the last chapter, this method is extremely powerful and has been proven to give particularly satisfying results.

2.2.3 Dynamic Image Thresholds

The coexistence of multiple phases in the flow because of reflections significantly increases the recorded noise levels especially in the vicinity of bubbles or droplets. In addition, the mass fraction of droplets or bubbles is continuously changing with time. Therefore it is important to filter out high-frequency noise both in time and space domain. This is accomplished by applying two types of adaptive filtering.

$$H\left(I_{ij}\right) = \begin{cases} I_{ij} \ if \ I_{ij} > h_{\max} \\ 0 \ if \ I_{ij} < h_{\max} \end{cases} \qquad (1.)$$

Let Ii,j be the intensity value of each discrete point in the image domain (pixel). We compute the intensity histogram for each image. The value of the lowest intensity

peak (hmax) is used as a criterion. If the intensity of each pixel is higher than the threshold value defined by the histogram, the value is preserved otherwise it is set to zero. This operation serves to remove the low-level background noise with a threshold value that adapts to each image. In practice, we apply this filter in an iterative manner depending on the image noise levels. Typical value of three iterations is usually sufficient.

2.2.4 Smoothing and Edge Detection

Area-base operations are preformed within windows of 3x3 pixels. Our objective is to separate the dispersed phases present in the flow without altering the information of the flow tracers. Once the low-level background noise is removed, the flow tracer particles correspond to small wavenumber (~3pixels) high frequency elements in the pictures. However, noise could still be present in the image, while it is important to consider the fact that the application of gradient-based edge detector in the subsequent step always amplifies the noise levels. Therefore, it is necessary to apply a smoothing filter. Khalitov and Longmire (2002) proposed a classic blur filter defined as:

$$I_o^{new} = \frac{1}{c+4}\left(cI_o + I_{i-1\,j} + I_{i+1\,j} + I_{ij-1} + I_{ij+1}\right) \qquad (2.)$$

This effort incorporated and tested the above filter. However, our experimentation showed that a Gaussian kernel that incorporates all the pixels in the 3x3 stencil performs better for most cases. This filter is defined as:

$$I_{ij}^{new} = \frac{1}{c_o + \sum c_{ij}}\left(c_o I_o + \sum c_{ij} I_{ij}\right) \qquad (3.)$$

Where Iij and cij correspond to the intensity value and the corresponding coefficient for all the pixels within the 3x3 window except the center one which is denoted with co and Io, where rij is the distance of each pixel in the stencil from the center one. The center pixel coefficient can take a value of 1 for very strong smoothing however arbitrary values can be used, depending on the images.

The Gaussian smoothing defines the first part of our LoG filter. We define a Laplacian operator that is convolved in the two-dimensional image domain with the 3x3 pixel windows. For small wavenumbers this filter is defined as:

$$I * L \quad where\, L = \frac{1}{4}\begin{bmatrix} 1 & 2 & 1 \\ 2 & 12 & 2 \\ 1 & 2 & 1 \end{bmatrix} \quad (4.)$$

This operation will perform as a high-pass spatial filter, practically eliminating image elements bigger than 3x3 pixels. Subsequently we perform an area binarization, which will set the value of the center pixel to zero or one, respectively, based on the area information. This area binarization is defined as:

$$\mathrm{I_{ij}} = 1 \text{ if } \mathrm{I_{sum}} = \iint_A \mathrm{I}dA \geq coef * 9 * I_{\max} \qquad (5.)$$

An image inversion and subtraction from the original image results in recovering the original image but with the dispersed flow elements removed. At this point we have decomposed the original image into two. The first image contains the flow tracers, and it will be used for performing the cross-correlation and the hybrid particle tracking velocity field evaluation. Typically one more image-processing step is performed.

2.2.5 Particle erosion

Particle erosion is used to identify every particle using only the highest intensity pixel. This step is extremely important during the process of particle tracking. The subsequent figures show an example of the above described image decomposition process using artificially generated images containing flow tracers and dispersed phase elements. Image (a) shows the original image, (b) shows the flow tracers after the erosion process and (c) the subtracted dispersed flow elements.

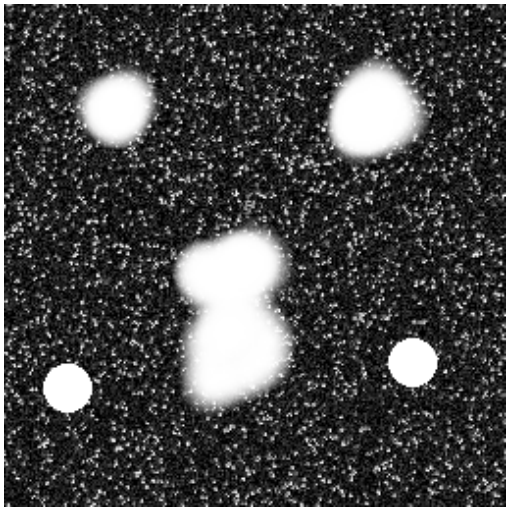

Figure 2.3: Original image (a) before decomposition

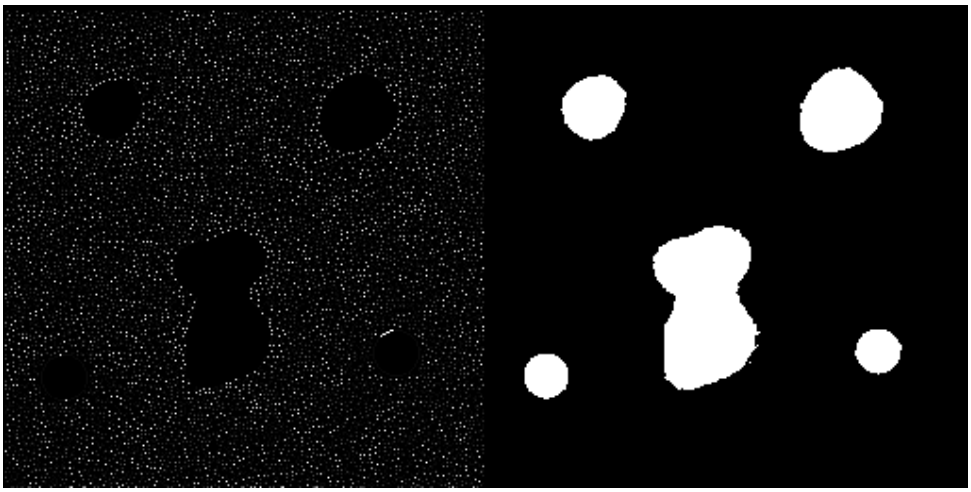

Figure 2.4: From left to right: images (b) and (c) after decomposition

The image containing the dispersed phase can be further processed. Different schemes can be employed to identify different size distributions. Recursive search is used to classify pixels that are connected to each other, thus defining a single element. Subsequently the apparent areas can be sorted with increasing size order and classified to the different phases if more than two are present in the flow.

2.2.6 Big particle segmentation

These last operations can be done using the scheme by Guezennec and Kiritsis (1990) for particle tracking velocimetry that was described earlier (paragraph 1.2.6.1. particle detection) and that ensures particle detection. The example below (figure 2.5) illustrates the performance of the algorithm.

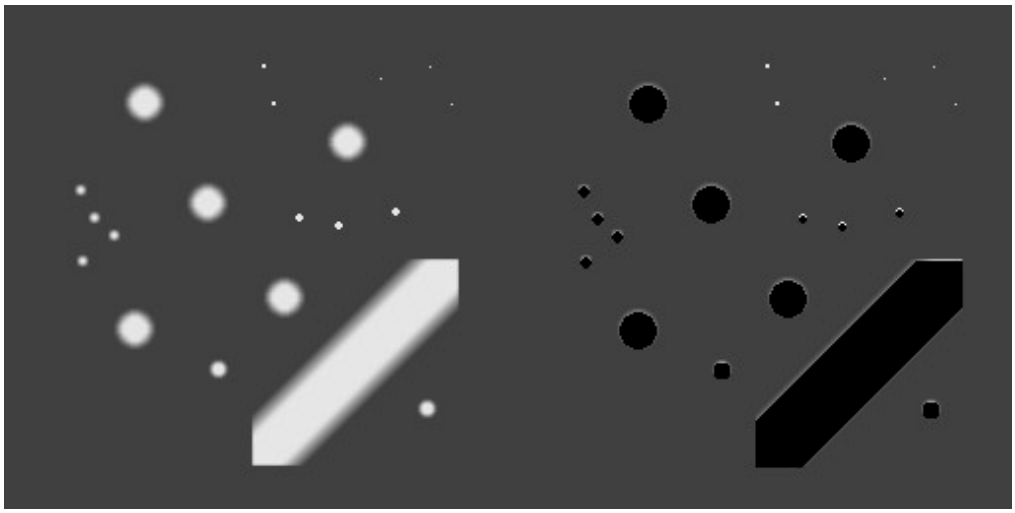

Figure 2.5: Big particle segmentation

Objects of different size and shape were artificially generated within an image with a uniform background. The scheme described above enables the detection of every object in the picture, including its shape and size. In this example, particles with area of 5 pixels (this number was arbitrarily chosen) were automatically removed, producing the image to the right.

2.3 Generation of artificial images

2.3.1 Purpose of the artificial images

In order to be able to quantify the accuracy of the presented system, so-called artificial images needed to be generated. The purpose of these artificial images is to provide a known flow-field with controlled experimental parameters such as noise, particle diameter and displacement. Knowing the deterministic description of the flow

field (for instance a uniform displacement, a Couette flow, or a vortex), it is possible to compare the expected value of any displacement in the flow (using the mathematical model) with the results given by the software. It is necessary to simulate a realistic experimental configuration, since in practice every recording of the flow field will contain noise due to setup inaccuracy, camera limitations, etc. Therefore, by controlling the experimental details via the generation of artificial images we can quantify the relative weight of each parameter and perform detailed error analysis revealing the total the bias and the random error of our measurements.

2.3.2 Particle generation, particle displacement

As shown by Adrian and Yao (1985) particle images can be approximated as Gaussian. Therefore, a number (selected by the user) of points are randomly generated within the image frame. Around each of these points and within a certain range, each pixel's intensity is evaluated based on a perfect Gaussian shape:

$$I(r) = I_0 \exp^{-br^2} \qquad (6.)$$

I_0 is the maximum intensity, b a coefficient related to the particle size, and r the distance from the particle's center. It is also possible to add artificial Gaussian noise to the image, in order to create artificial images closer to real ones. Although several tests were performed using noisy images all along this work, no investigation with this type of images will be discussed here.

Once particles have been generated for the first frame, a mathematical description of the flow field is used in order to determine the position of the particles within the second frame. Since each particle location is known from its generation, the expected displacement is derived based on the initial position of the particle, thus providing the location of the particle within the second frame. For instance in the case of a vortex, the distance from the center of the particle to the core of the vortex is computed, giving the displacement of this particle (based on the theoretical equation of a vortex), and therefore its new location. However, one has to be careful concerning the particles that leave the

interrogation domain between two consecutive frames: indeed, the image needs to be reseeded in order to maintain the same number of particles from one frame to the other. Therefore, each time a particle leaves the frame, it has to be reallocated to a new random position where particles are supposed to appear on the frame. If we keep the example of a vortex, the core of which is at the center of the image, particles would leave on the edges. In the case when it wouldn't be reseeded, or reseeded in the central part of the vortex, a lack of particles would be noticed on the edges of the artificial images. One could also account for this issue in seeding a larger area than needed. This would be conceivable in the case of a vortex where every particle remains at the same distance from the center. However, in the case of a uniform displacement for instance, no matter the original size of the seeded area, particles would inevitably end up leaving the domain.

2.3.3 Generation of uniform flow fields and ALI (Artificial Linear Increment) images

In the scope of this work, we will focus the error analyses on uniform displacements (at 45 degrees inclination), as well as on pseudo-vortical flows. Uniform displacements are traditionally used for DPIV error analyses. We chose 45 degrees inclinations in order to make sure that the software was performing correctly in both directions.

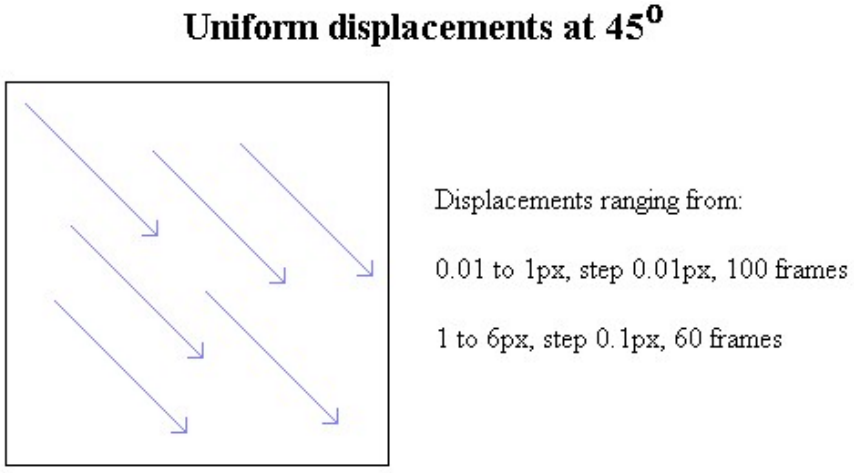

Figure 2.6: Images concerning uniform displacements

Indeed, numerous features (like offsets) are implemented independently for each axis, so that verifying the correct functioning of these features in a single direction does not provide a full certification of the system's performance As shown in figure 2.6, uniform displacements were generated using 0.01 pixels steps from 0.01 pixels all the way to 1 pixel. Also, sixty other pairs of images were generated with displacements going from 1 to 6 pixels using steps of 0.1 pixels. Because of the discrete window offset feature, the error pattern between zero to one pixel displacement has to be repeated with a wave number of one pixel for all the higher displacements.

Uniform displacement analyses are very common in the literature. However, this is too uncomplicated of a test compared with realistic flow fields in order to reveal the actual performance of a scheme. Therefore, we artificially generated pseudo-vortical flows (ALI images), consisting of a linear increment of the velocity up to a maximum displacement (V_{max}), followed by a linear reduction of the velocity, in terms of the distance of the particle from the center of the image, as shown below in figure 2.7.In this figure R_f represents the length of the half diagonal of the image. Therefore, the resulting displacements start from zero at the center of the image (core of the vortex), reach a peak at $R=R_o$, before decreasing down to zero at the corners of the image.

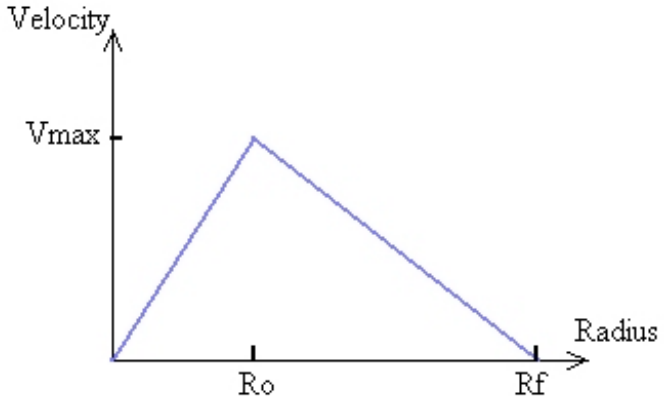

Figure 2.7: Linear increment displacement

$$\begin{cases} 0<|R|<R_0 \Rightarrow V = V_{\max}\dfrac{R}{R_0} \\ R_0<|R|<R_f \Rightarrow V = V_{\max}\dfrac{R_f - R}{R_f - R_0} \end{cases} \qquad (7.)$$

Applying these formulas over the whole flow fields leads to the representation shown in figure 2.8. As a result, varying V_{max} or R_0 modifies the velocity gradient in the flow-field. The images used for the tests in the scope of this work were generated using $R_0 = R_f/3$, thus providing a stronger gradient within the center of the image than on the sides.

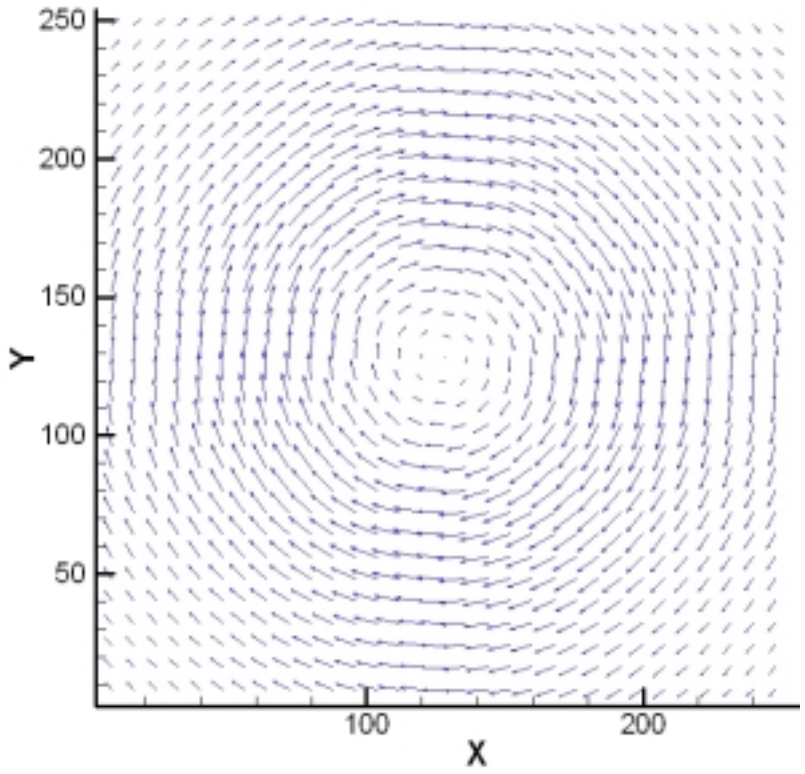

Figure 2.8: Example of ALI image (Umax = 4, $R_0 = R_f/3$)

This was done in order to be able to study two different gradients within one image. Also, the maximum velocity point is expected to be difficult to resolve due to the presence of two opposite gradients in the same area, together with the center of the

vortex, where a high gradient is combined with small velocities, within smaller and smaller areas when approaching the very center of the flow-field. As shown in figure 2.9, two maximum displacements were used for the comparisons, 4 (ALI4) and 8 (ALI8) pixels. The displacement gradients of the ALI8 images are twice the ones of the ALI4 images. Therefore, ALI8 images are our toughest experiment, likely to generate higher errors than ALI4 images.

Although the uniform displacement artificial images will be used in order to be able to compare our results with the ones commonly found in the literature, the most important part of the analysis will be carried out using the ALI images.

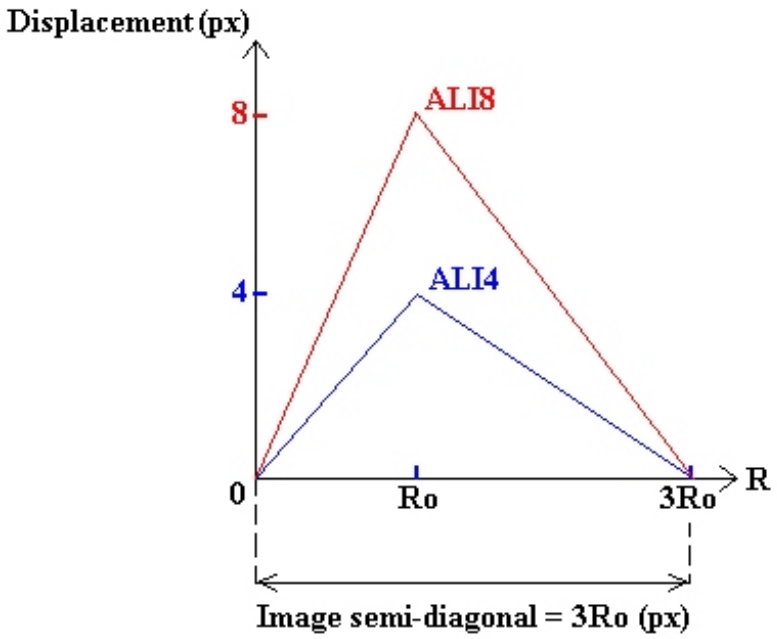

Figure 2.9: ALI images

2.4 Error-analysis using Monte-Carlo simulations

The artificial images described in the previous paragraph were employed to carry out Monte Carlo simulations. These simulations constitute a statistical characterization of the performance of the various implementations by varying one or more independent parameter. For the purpose of this investigation the only parameter considered was the

displacement field. These simulations will allow us to validate our results, become aware of mistakes inherent to the programming scheme and compare our results to previously published ones.

Two different sets of Monte Carlo simulations were used in the scope of this work: in the case of uniform velocities, the error was calculated in terms of the particle displacement, whereas in the case of the ALI images, one hundred consecutive frames depicting the same flow field were artificially generated providing an error estimation at each point of the flow field.

2.4.1 Uniform displacements

Initially the accuracy of the method was evaluated using Monte-Carlo simulations with artificially generated images of uniform displacement fields. In order to have a basis for future comparisons we followed the analysis of Huang and Gharib (1997) and Huang et al. Therefore a mean particle diameter of 2.8 pixels and particle density of 0.05 particles/pixel was selected. A Gaussian-intensity laser sheet was simulated and the particles were uniformly distributed in all direction (x,y,z). Background white noise with intensity of 5% was applied to simulate realistic recording conditions. The pixel resolution was 256x256 and the vector grid spacing was 4 pixels resulting to 61x61 (3721) vectors from the cross-correlation with a minimum window of 16x16. Uniform displacements between 0-1 pixels with displacement steps of 0.01 pixels and displacement between 1-6 pixels with displacement step of 0.1 pixels were examined. It is important to mention that due to the DWO application, after the first iteration, the evaluated displacements are always between 0-0.5 pixels. The hybrid evaluation resulted in approximately 3000 vectors for each case

For each one of the displacements under consideration, the bias, rms (root mean square), and total error are computed over the whole flow field.

The bias error is defined as the difference between the averaged measured velocity over the whole flow-field and the expected (known) velocity:

$$\varepsilon_{bias} = u_{mean} - u_{\exp} = \frac{1}{N}\sum_{n=0}^{N} u_n - u_{\exp} \qquad (8.)$$

The root mean square error (the definition of which was chosen so as to be in agreement with the publication by Huang and Gharib (1997)) is then defined as the standard deviation of the measured velocity to its mean:

$$\varepsilon_{rms} = \sqrt{\frac{\sum_{n=0}^{N} (u_n - u_{mean})^2}{N}} \qquad (9.)$$

Finally, the total error can also be computed, based on the aforementioned definitions:

$$\varepsilon_{total} = \sqrt{\varepsilon_{bias}^2 + \varepsilon_{rms}^2} \qquad (10.)$$

In the case of uniform displacements, pairs of images were artificially generated, ranging from zero to one pixel displacement using a 0.01 pixel step (so that a hundred pairs of images were in fact generated). Because most of PIV schemes use the window offset (described in chapter 3), many error analyses found in the literature do not present the error above one pixel displacement. However, programming mistakes in the implementation of the discrete window offset or stray vectors due to noise are extremely likely. Therefore for completeness of this analysis as well as for confirming the accurate implementation of the various schemes it seemed particularly reasonable to incorporate in our error analysis a range from 1 to 6 pixels displacement using a 0.1 pixel step. An example of the statistical results obtained follows in figure 2.10 (this example doesn't represent results discussed in this effort).

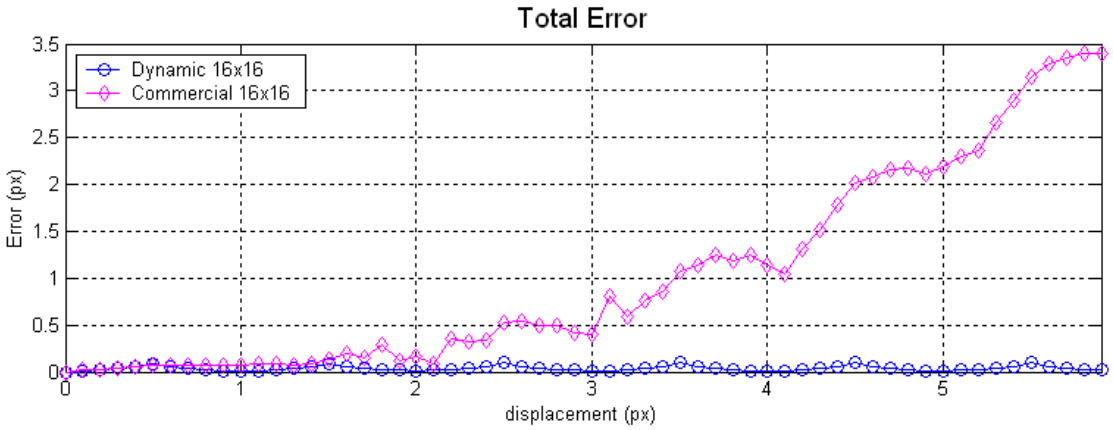

Figure 2.10: Example of statistical plot

2.4.2 Statistical analysis for ALI images

Numerous publications comport error analyses based on uniform displacements. However, realistic applications require resolving vortical flows, flow reversals or step velocity gradients. A scheme that would perform well in the case of a uniform flow field can be proved to be insufficient for real data. Therefore, ALI images presented in the previous paragraphs were used in order to carry on more realistic statistical analyses. Indeed, ALI images represent vortical flows with high step velocity gradients. Starting from an image containing randomly located particles, the position of these particles within the following image was computed using the set of equations (7). The operation was repeated from frame to frame until a hundred frames were generated.

For each point in the flow-field, its radius (distance from the point to the center of the image) was calculated leading to the expected velocity at that point. Then, taking in consideration all the points being at the same position within the hundred generated frames, the bias, rms, and total errors were computed.

A curve representing the variation of these errors in terms of the radius was considered, however after implementing this approach, we realized that data presentation miscommunicated the results. Therefore, a graphical way was finally employed using

color contoured plots of the corresponding errors to facilitate their reading. Figure 2.11 illustrates the sort of plots that were obtained by means of this routine.

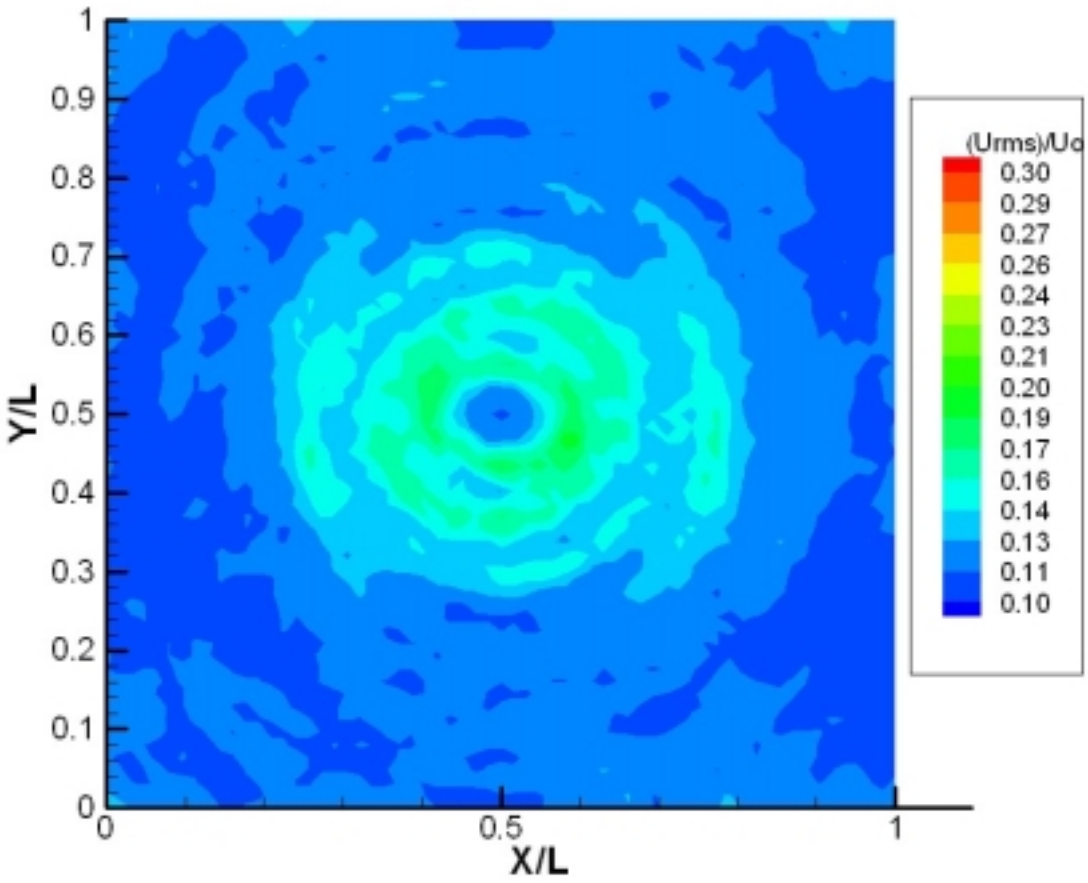

Figure 2.11: Example of the statistical analysis of ALI images (hybrid-ALI4)

A mean bias, rms, and total error were also computed by averaging the results over the flow field, providing direct means of comparison of the performance of each considered technique.

Chapter 3 DPIV Methods

In this chapter, we will focus on the development of the novel DPIV scheme developed in this effort. Starting from a very basic cross-correlation, we will discuss step by step the improvements brought to the method, as well as their effect on the accuracy of the method. Firstly, implementations of methods presented in the literature will be presented(dynamic adaptive window, dynamic window offset, second order offset), followed by the original contribution of the present effort (ultimate cross-correlation and ultimate off-check schemes).

Improvement of the cross-correlation velocity evaluation algorithms is critical for the improvement of the performance of the system. The dynamically adaptive cross correlation is a stand-alone module that evaluates the velocities present in the flow and also initializes the hybrid particle-tracking scheme. Therefore, accurate estimation of these velocities will increase the accuracy and reduce the number of stray vectors thus minimizing the need of validation, data filtering and interpolation schemes.

3.1 Original DPIV

3.1.1 Features

We started with the very basic algorithm by Gharib and Willert (1991). This scheme follows the standard ideas mentioned in the first chapter of this work. Figure 3.1 gives an idea of the original algorithm that was used.

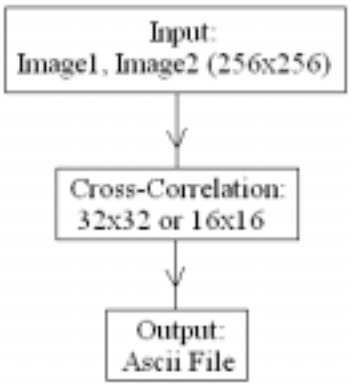

Figure 3.1: Original algorithm

Given two images, cross correlations were performed using 16x16 or 32x32 pixels interrogation windows using an overlap fixed to 75 percent.

3.1.2 Advantages and drawbacks

Taking into account the one-fourth rule, the maximum displacement that this scheme can possibly accurately resolve is one of 8pixels (using 32x32 interrogation windows). However, the use of large windows introduces space-averaging effects. Since DPIV is unable to resolve rotational components of the flow, space-averaging can have a significant impact on the resolution of small length scales. Besides, using a unique cross-correlation pass, it can be shown (Westerweel, 1997) that the error increases linearly with the particles displacement. Also, such a scheme could be affected by the peak-locking phenomenon, namely the tendency of the displacement evaluation to “lock” on the nearest integer value, as it will be explained in the fifth chapter of this thesis.

The major advantage of using such an algorithm is that it has been validated and tested by others. However, two major drawbacks can be pointed out: first, the code used the very basic ideas of PIV providing an imprecise method as it will be shown in the chapter relative to statistical analyses. Then, with the purpose of implementing some of these, we had to deal with an unfamiliar code. This starting version was extremely rigid, lacking of basic flexibility and user interaction. Several parameters were hard coded. For instance, the size of the images was required to be 256x256 pixels, which happens not to

be the case for many standard cameras on the market. Also, the window size was hard-coded to 32x32 pixels. It was therefore user intensive to modify each parameter when required. In addition no validation, interpolation, or smoothing features were incorporated to the scheme.

Consequently, the main goal of the present effort was to improve on the basic aforementioned version, in order to obtain a scheme subject to a reduced amount of drawbacks.

3.1.3 Performance

3.1.3.1. Monte-Carlo simulations

Using the Monte Carlo simulations discussed in the second chapter of the present work, we were able to quantify the error of this scheme. The error analysis presented in figure 3.2 was carried out employing the uniform artificial images, and the DPIV scheme used interrogation windows of 16x16 pixels. As we can see, the error is quite low for small displacements. However, the overall error significantly increases with the displacement. The mean total error (right of the figure, averaged form 0 to 7 pixels displacements) is 2, which is significant. According to the one fourth rule criterion the interrogation window size has to be at least four times the displacement of the particles within that window while displacements up to one half of the window size are resolvable. In this case, a 16x16 window thus should be performing correctly up to four pixels displacement. If the bias error seems to follow that rule quite precisely, the rms error (and consequently the overall error) begins to increase significantly for displacements larger than two pixels.

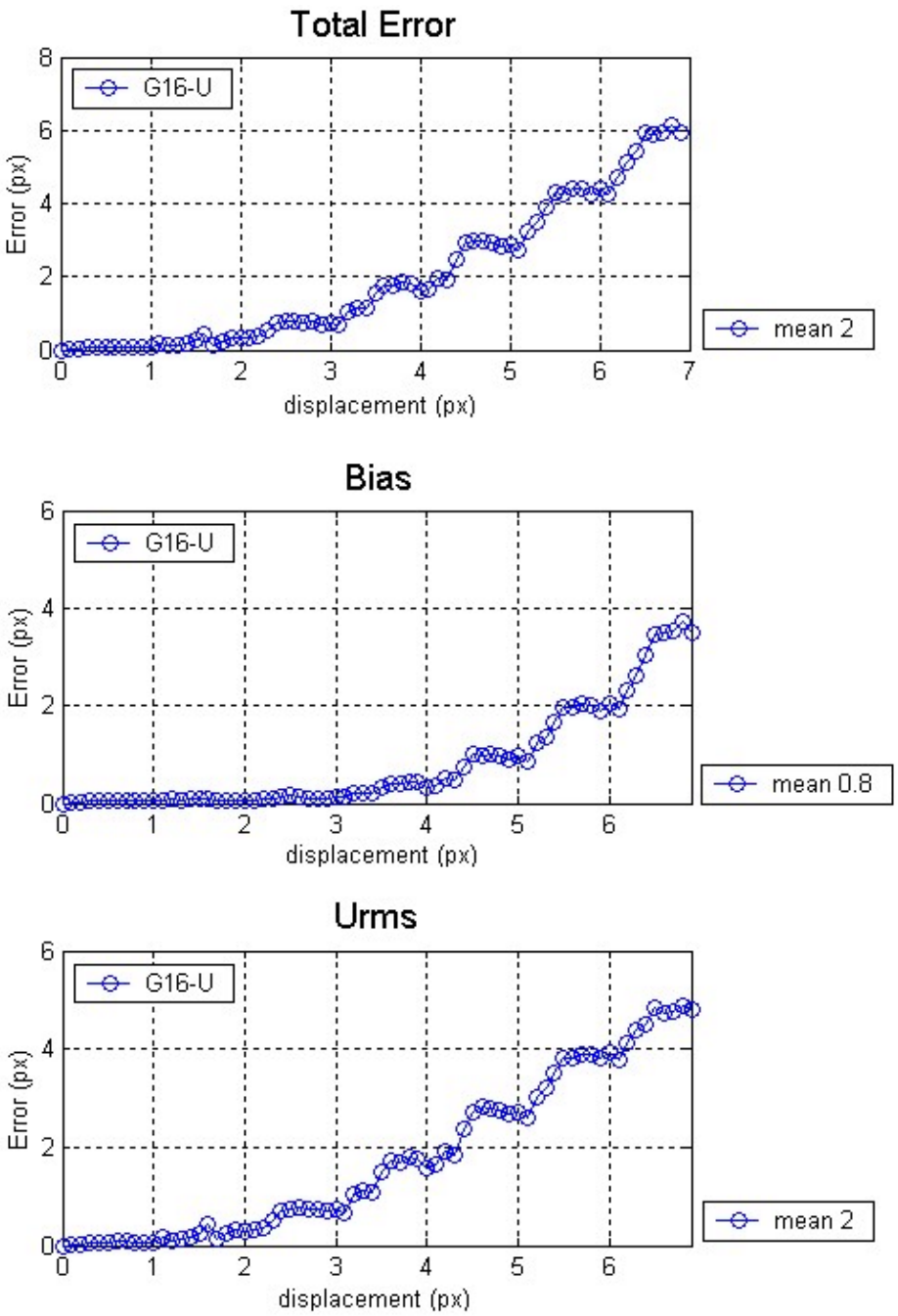

Figure 3.2: Error analysis (G16-U: Original scheme, 16x16px interrogation windows, Uniform flow)

3.1.3.2. ALI images

Tests were performed using ALI images. The figure below represents the recovered flow field for ALI images with a maximum displacement of eight pixels.

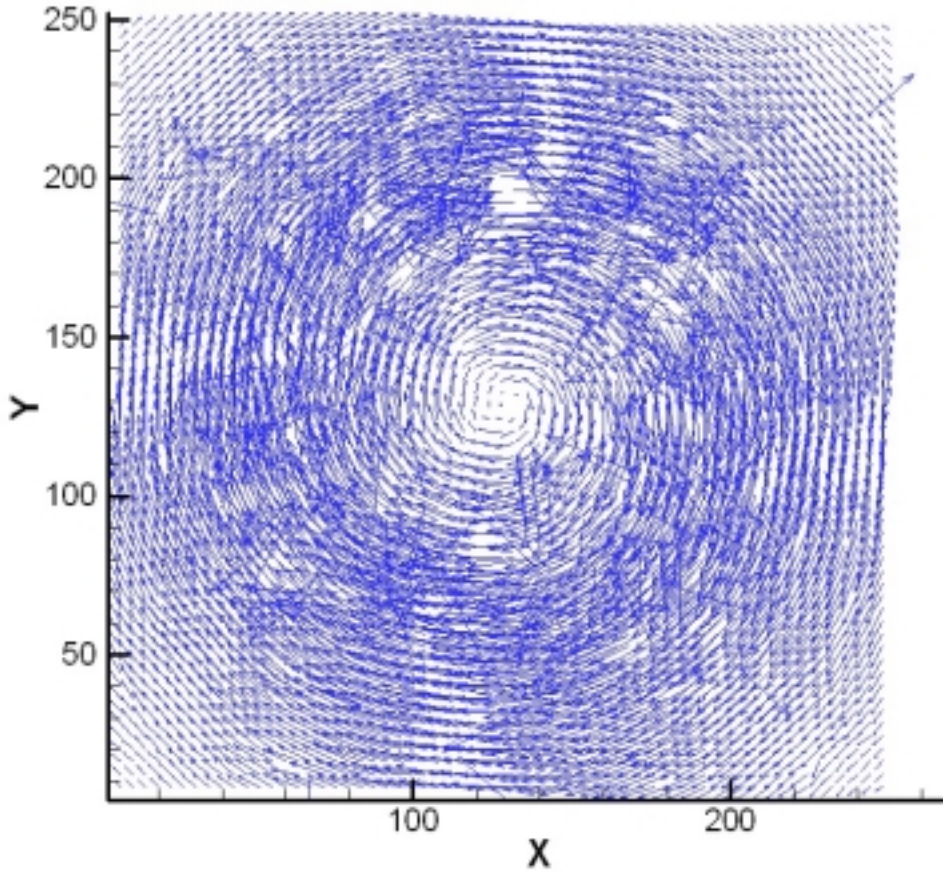

Figure 3.3: ALI8 using the original DPIV scheme

Figure 3.3 confirms the existence of major drawbacks inherent to the aforementioned method. High displacements are far from being accurately resolved.

3.2 Dynamic adaptive window

3.2.1 Scarano & Rieuthmuller's method

A first improvement to the method was implemented using the scheme proposed by Scarano & Rieuthmuller (1999). In the basic scheme previously studied, the window

size was depending on the highest velocity present in the flow field. As a result the velocity has to be at most one fourth of the window length in order to give a satisfying estimation of the displacement. In Scarano & Rieuthmuller's method, a rough first pass is performed using large enough interrogation windows, as described in the original scheme. Then, a second pass is carried out, using the results of the first pass as an initialization for the adaptive process, where the size of the window of interrogation is dynamically allocated based on the previous step results. The velocity obtained from the first pass gives the minimal window size that can be used in order to provide a reasonable estimation of the displacement. Figure 3.4 gives an example of the windows used during the first pass (on the left), and the windows used on the second pass (on the right).

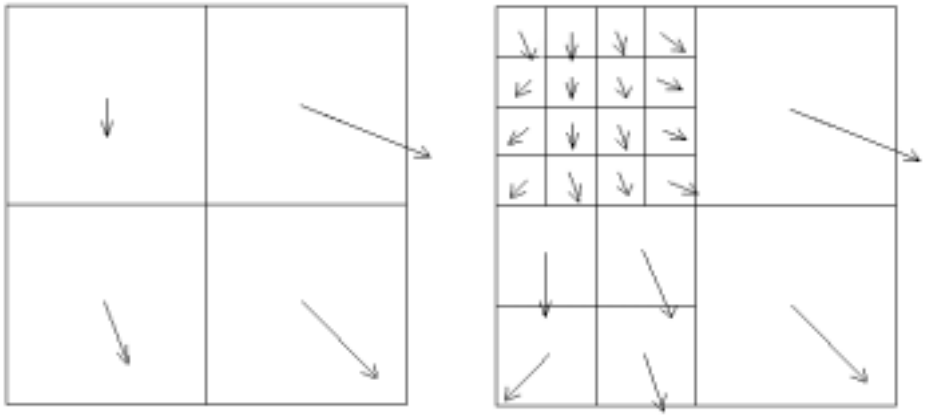

Figure 3.4: Window break

Each original window is thus broken down into several windows. A great advantage of this implementation emanates from the fact that successive reductions of the window size results in minimizing the spatial averaging effect inherent in the cross correlation process. Because velocities are different from one window to the other, two contiguous windows might be broken down into a different number of sub-windows, resulting in a non-uniform grid.

In order to avoid the need of reconstructing a uniform grid from an unevenly sampled domain , one can simply take the smallest possible step between two windows

(function of the smallest possible window size plus its overlapping) as a fixed grid, and center a window of desired size at each point of it to perform the correlation. This simple idea is an improvement upon Scarano & Rieuthmuller's approach that was exploited in this effort. Despite the obvious advantage of controlling the number of grid points independently of the velocity field it will be demonstrated that this approach is superior because the successive passes are initialized by displacement predictors that are evaluated in the same measurement point as the new ones. This feature improves the performance when vortical flows or flows with high shear are evaluated. This feature will be described in detail in a following paragraph. Here we will focus on the basic multigrid approach.

3.2.2 Resulting improvement

Investigations were carried out using the ALI images. Figure 3.5 represents the dynamic adaptive window performance in the case of ALI with a maximum displacement of eight pixels.

A first pass was performed using 64x64 pixels interrogation windows, with no overlapping, resulting in sixteen velocity vectors describing the flow field. Depending on these velocities, windows of 32x32 down to 16x16 pixels were used during the second pass. In the center of the image as well as on the sides, the velocities were small enough, so that 16x16 windows could be used (blue vectors). On the right side of the center however, the velocities found during the first pass were higher than eight pixels. Therefore, interrogation windows of 32x32 pixels were used in that section (cyan vectors).

During the second pass, after a displacement has been computed, its value is compared to the window size. It is then rejected if it doesn't satisfy the one-fourth rule, and the result of the first pass is used instead. In figure 3.5 presented below, all the vectors on the sides should have been blue if the displacement obtained throughout the cross-correlation process had been found to be less than four pixels. Thus, all the red vectors correspond to velocities the magnitude of which were found to be higher than

four pixels. Because they would have been likely to be erroneous velocities estimation, they were then replaced by the result of the first pass.

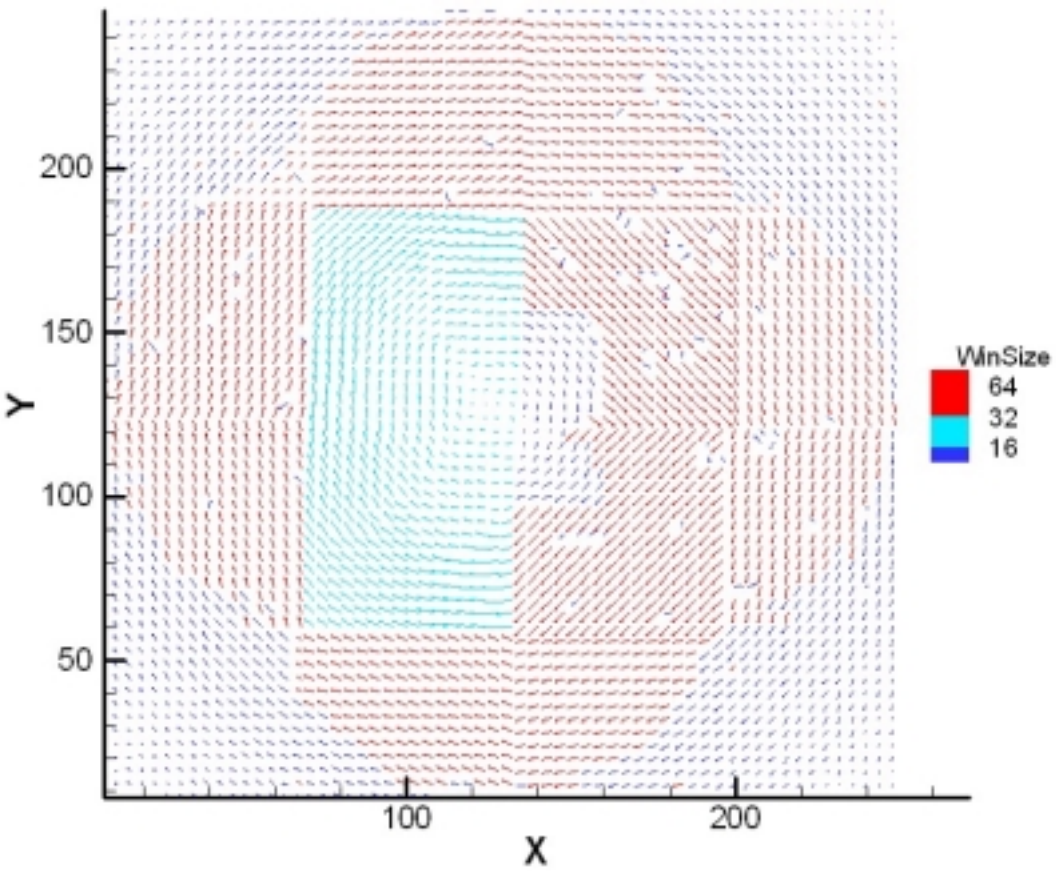

Figure 3.5: Dynamic adaptive window

If we compare the results obtained to the ones from the original scheme that was discussed in the previous section, we notice that high velocities are much better evaluated. However, in order to get better results, one should avoid replacing erroneous velocities with the first pass results. Instead, a final pass using the initial window size should be carried out centering each interrogation window at the points of interest.

3.2.3 Drawbacks

The aforementioned scheme is interesting, but is of feeble effect when the following dynamic window offset is incorporated. The window offset enables one to get

predicted displacements during the second pass which are under one pixel: therefore, the second pass can be implemented with any window size, as it will be seen in the following paragraph.

3.3 Dynamic window offset (DWO)

3.3.1 Original idea

In the scheme discussed above, two images are correlated, providing an estimation of the velocity at the center of each window. In order to obtain more accurate values, DPIV algorithms use a first pass as an initial predictor of the flow field. The resulting flow field initializes a discrete window offset to compensate for particles that move outside the window of interrogation (Westerweel J., 1997), subsequently resulting in a more accurate predictor of the flow field.

Figure 3.6: Initial predictor, velocity refinement

The initial predictor provides an approximation of the displacement of the particles from one frame to the other (first two frames of figure 3.6). However, particles that were located in the interrogation window in frame1 moved (approximately by the displacement given by the cross-correlation). Consequently, the particles that are present in frame 1 are correlated with a different set of particles in frame 2. The dynamic window offset pass considerably reduces this error. Knowing the location of the particles in frame 2, a second cross-correlation is performed, between the original window in frame 1, and a shifted window in frame 2 (see figure above). This last window corresponds to the location of the particles that were in frame 1 at time t that changed location during the time dt. The fact that particles are correlated with themselves considerably reduces the noise level, thus providing a better approximation of the flow field.

3.3.2 Implementation

Originally, we wanted to use the window offset coupled with Scarano & Rieuthmuller's technique. Therefore, as shown in figure 3.7, a first pass serves as an initialization for the second pass. However, the first pass actually consists of two steps: a first rough estimation of the velocity, followed by a refined velocity based on the dynamic window offset. In a second pass, following Scarano & Rieuthmuller's method, each of the above window is broken down into several windows, the size of which is found based on the Nyquist frequency criterion.

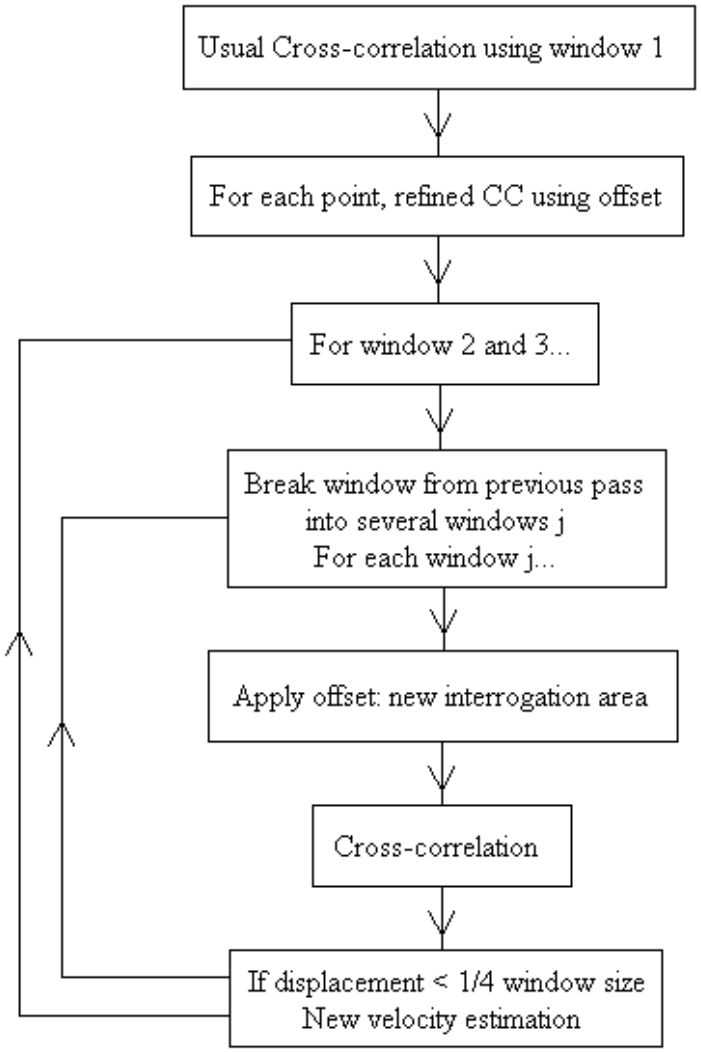

Figure 3.7: Implementation of the dynamic window offset

Thanks to the window-offset feature, the window size is not limited by the Nyquist criterion: indeed, the first pass is supposed to give an estimation of the velocity with an error below one pixel. Therefore, the window size can be as small as four pixels. This size being too small to provide any reasonable estimation of the velocity, it can be said that any window size (typically above 8 pixels) can be used in a pass that uses the window offset feature.

Therefore, each original window can be broken down several times into smaller ones, as shown in the algorithm o figure 3.7. Each result has to verify the Nyquist criterion. If this criterion is not satisfied, for whatever reason (noise, too small window), the value is not recorded.

3.3.3 Global improvement

3.3.3.1. Monte-Carlo simulations

Focusing on figure 3.8, we can easily notice the significant improvement brought to the method compared with the basic scheme (figure 3.2). The former gives a mean total error of 0.05 while the latter goes up to 2. As expected, the window offset enables one to get an accurate estimation of the velocities for any displacement. Bias and rms error are found to be consistently under 0.05 pixels, except for the .5 values. This is to be attributed to the peak locking effect, as it will be seen in the chapter on error analysis. It is important to note that since after the second pass all the displacement refinements are between 0 and 0.5 pixels the error demonstrates a periodic behavior with a wave number of 1 pixel and appears to be linearly increasing and decreasing.

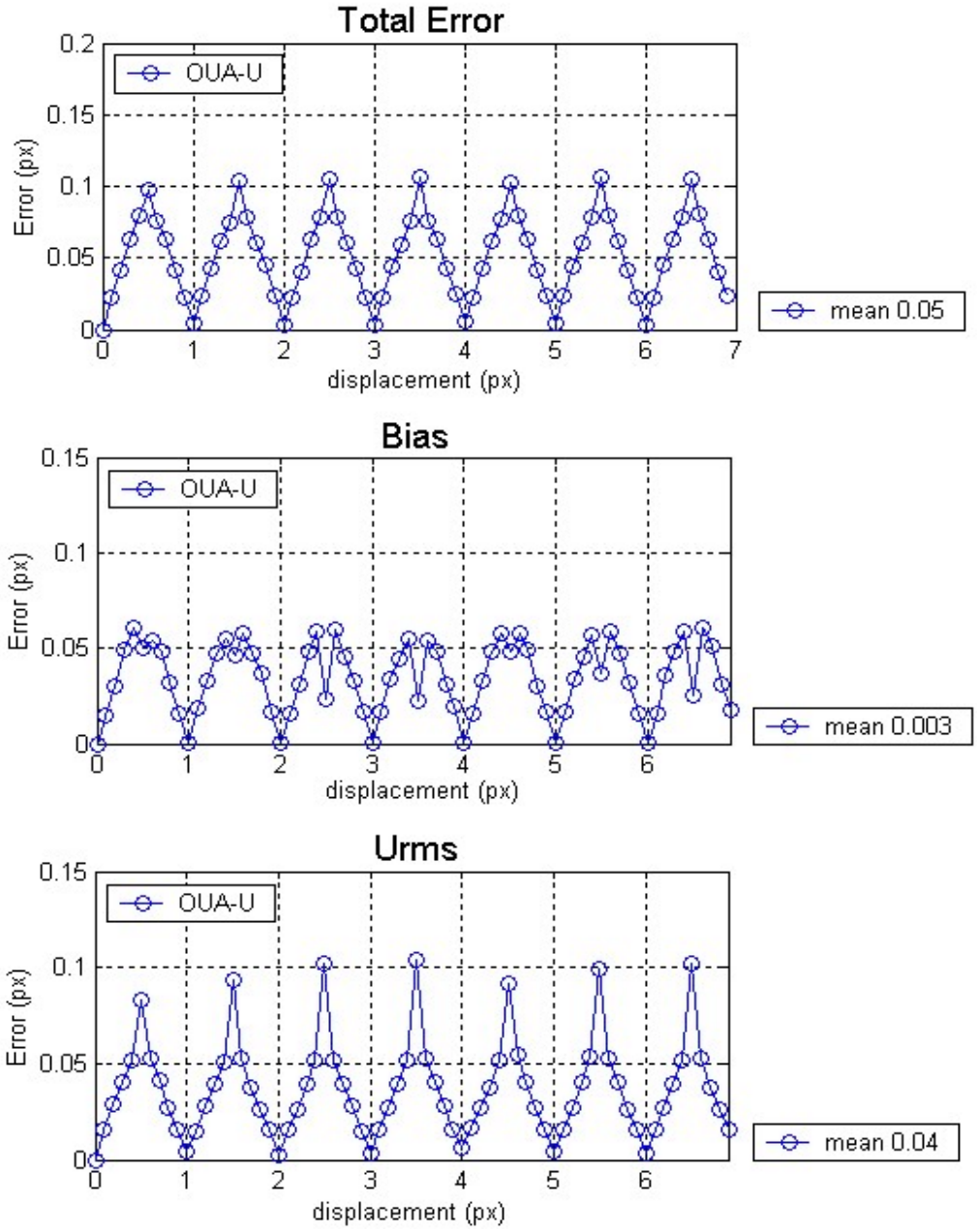

Figure 3.8: Monte-Carlo simulations concerning the Dynamic Window Offset scheme

3.3.3.2. Analysis with the ALI images

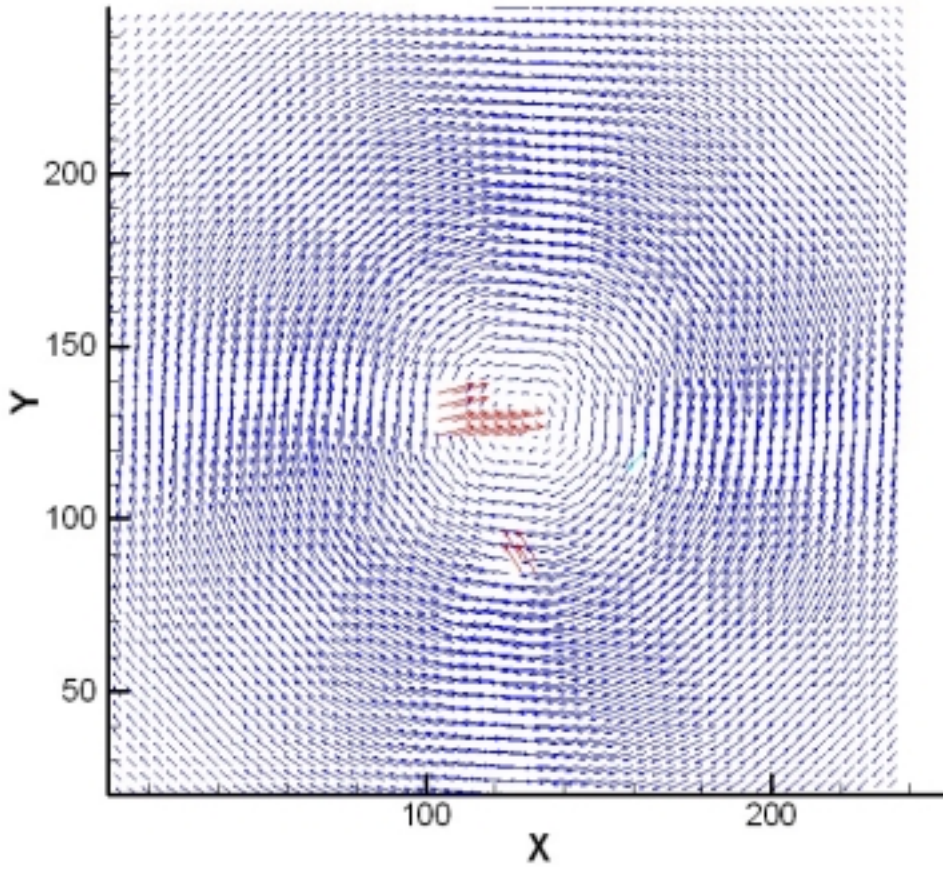

Figure 3.9: ALI image processed using the Dynamic Window Offset scheme

A simple glimpse at figure 3.9 shows the resulting improvement compared with figures 3.3 and 3.5. The vectors in red were found using 64x64 pixels interrogation windows, since smallest windows were found not to fulfill the Nyquist criterion. They occur in the area where the velocity gradient is the strongest, and where the velocity reaches a peak: two regions where the cross-correlation is challenged. Indeed, within these regions, the interrogation windows will include particles with significantly diverse displacements. Overall, the velocity flow field is extremely well defined. Moreover, the spurious vectors are quite obvious ones, and would easily be detected using a validation scheme of any sort.

3.3.3.3. Drawbacks

Inevitably, any incorrect evaluation of the velocity during the first pass leads to erroneous velocity evaluations for any velocity vector that was computed using this velocity offset. All the wrong vectors from the previous picture stand together: a wrong evaluation was done during the first pass, so that breaking the original window into a smaller one lead to several wrong estimations. However, these major disadvantages are inherent to all the existing DPIV schemes. In the following paragraphs a scheme developed during the present effort that overcomes these key weaknesses will be presented.

3.4 Second order window offset

3.4.1 Second order accuracy

A second order DWO (Dynamic Window Offset) as proposed by Wereley and Meinhart (2001) was also implemented. In their work, for micro-DPIV, they illustrated the effectiveness of performing the DWO by employing an adaptive, second-order finite-difference scheme. The principle is based on translating the interrogation windows for both images forward and backwards respectively by ½ of the displacement estimated from the previous cross-correlation step. This is illustrated schematically in figure 3.10.

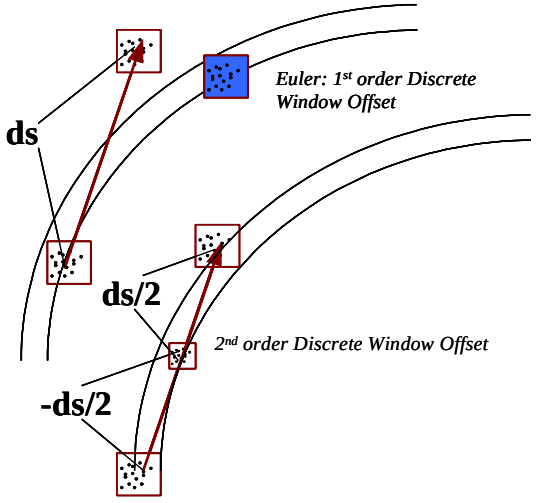

Figure 3.10: Second order window offset

By performing a second order shift we predict with higher accuracy the new position of the particle pattern and thus increase the signal-to-noise ratio of the next cross-correlation step. In addition, this can be a very important element for resolving vortical flows, where a forward difference DWO scheme will probably predict an erroneous position for the pattern of particles (see figure 3.10).

3.4.2 Resulting improvement

The results obtained from Monte Carlo simulations were very similar for both the first and second order window offsets, but analyses carried out using ALI images showed a significant improvement due to the second order offset. Their detailed analyses and comparison will be seen in the chapter dedicated to error analyses.

3.5 Ultimate adaptive window

The following method was developed and implemented in the present work in order to improve on aforementioned usual DPIV schemes as well as to adapt DPIV to multi-phase flows.

3.5.1 Ultimate cross-correlation method

Usual DPIV schemes are based on the ones seen above. However, when analyzing poly-dispersed multi-phase flows, we have to account for the presence of multiple length scales. Very often, the interrogation window will contain a large-scale droplet or bubbles. The image pre-processing procedure described earlier will remove the dispersed flow elements. But these regions will not contain any particles, which in effect will compromise the cross-correlation in their neighborhood, resulting in erroneous vectors. In order to preserve the advantages of the adaptive algorithm without affecting the quality of the resulting velocity measurements, a modified adaptive cross-correlation is employed. Following the image processing operations, the boundaries of the areas of interest are defined. An interrogation mesh is generated such that the windows do not contain the regions where bubbles or droplets exist. The mesh can be adjusted such that the cross-correlation process generates velocity vectors around the droplets or bubbles with

resolution defined by the user. For each point in the mesh, a first cross-correlation is performed, providing a first estimation of the actual velocity. The subsequent step reduces the size of interrogation window, while employing a discrete window-offset (DWO) (Westerweel 1997). This last operation is repeated using smaller interrogation-windows, until a specified minimum window size is reached (typically 8x8 pixels), or the criterion of the maximum measured displacement is in the order of one fourth of the window size. Practically this condition is always satisfied since the use of the discrete window offset results in displacements in the order of 0-1. This process is illustrated in figures 3.11 and 3.12 below.

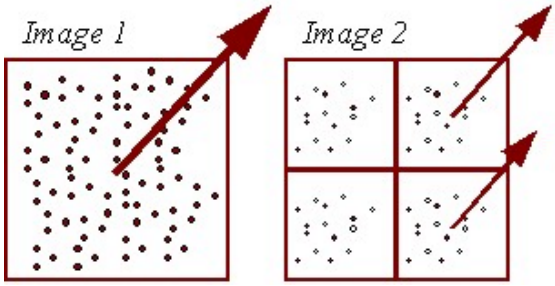

Figure 3.11: Classic approach

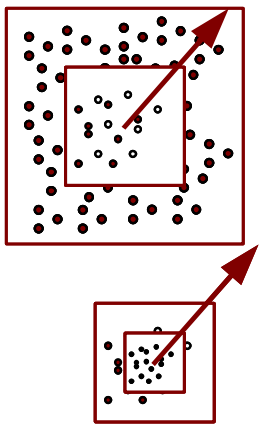

Smaller Window 8x8 pixels

Figure 3.12: Modified adaptive window scheme

The proposed method is improved compared with conventional adaptive schemes (Scarano & Rieuthmuller, 1999) in the sense that the velocity evaluation points are

determined based on the image information about the shape, size and distribution of the dispersed phase and not with the window size and the overlap ratio. In addition, by fixing the position where we evaluate the velocities, each subsequent step is initialized by the results of a previous correlation of particle patterns that are a superset of the current ones, thus continuously refining the same velocity without changing the measurement point.

In addition, as it was demonstrated earlier when employing the conventional multigrid approach an erroneous estimation during the first pass will subsequently affect all the resulting vectors. With the proposed approach every velocity evaluation becomes independent from its neighborhood.

Figure 3.13 presents the algorithm of the original ultimate cross-correlation method. It can be compared to figure 3.7 that presents the algorithm used by standard DPIV schemes. The former appears much simpler, and is therefore much more flexible.

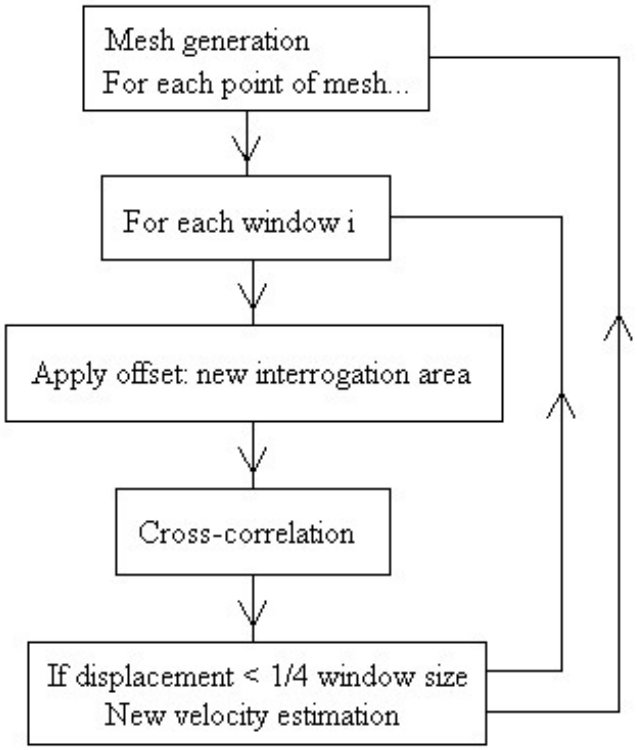

Figure 3.13: Ultimate Cross-correlation algorithm

3.5.2 Resulting improvement

At this level of improvement, the statistics discussed in the section dedicated to the error analysis will show the actual enhancement of the method. However, several other major improvements can be pointed out: first, the ability of getting velocity vectors at the desired location. Second, an impressive flexibility: indeed, a first pass can eventually be carried out using a smaller window than during the second pass for instance. This flexibility appears as well in the programming source code, which happens to be much more transparent than the one dedicated to the adaptive method. Moreover, any sort of grid specified by the user can be easily processed, a feature that is not available in usual DPIV schemes.

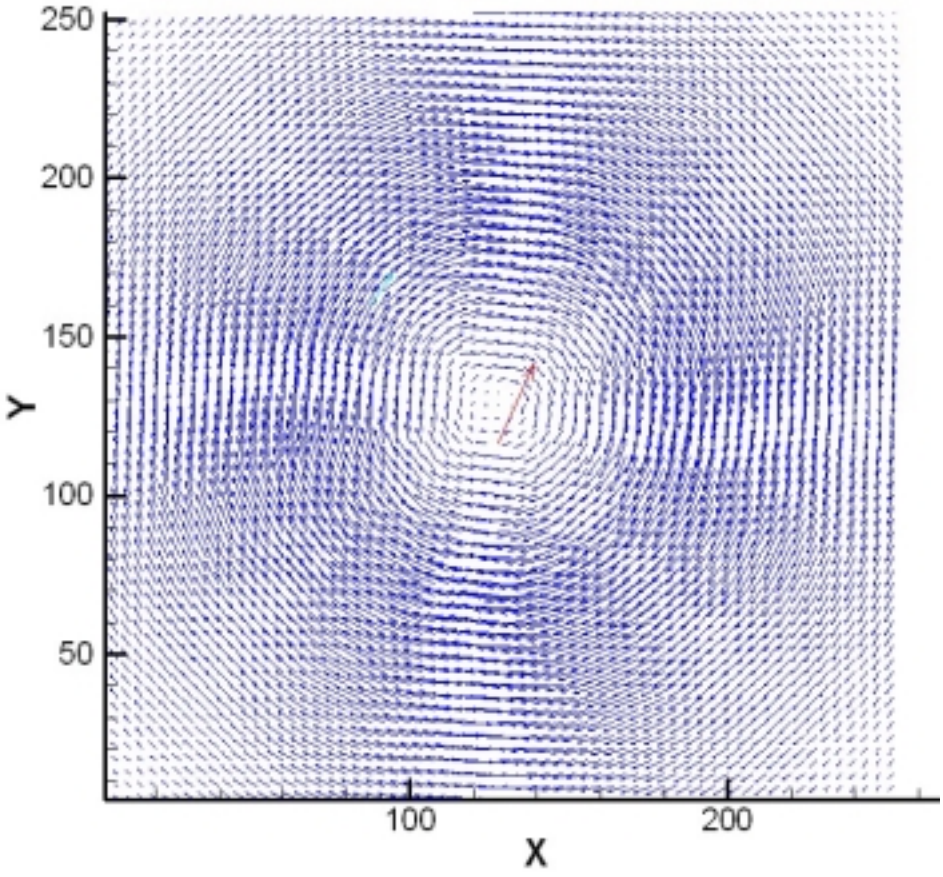

Figure 3.14: ALI image processed thanks to the Ultimate scheme

Processing the same images as before gives only a single spurious vector (see figure below). This improvement is likely to be due to the fact that the velocity estimation takes place at the exact same location during each step of the process, providing a more accurate velocity offset than usual DPIV systems. But also, a wrong velocity estimation doesn't lead to several wrong vectors, as in common DPIV schemes: it leads only to one, as it can be seen in figure 3.14.

3.6 Ultimate scheme with automatic offset verification

Taking advantage of the outstanding flexibility of the ultimate method another method -the implementation of which was hence fairly straightforward- was developed, providing an automatic validation of the offsets as well as an automatic choice for the window size. In other words, this method detects the specific window size that is to be used in order to obtain the best possible estimation of the offset at each point of the flow-field. Also, the user is informed if no realistic value could be found, preventing flow-fields to be overrun with erroneous vectors.

3.6.1 Automatic offset verification

The weakness of the offset scheme is obviously that in the case when the offset estimation is incorrect (this can happen when an inadequate window size is used), the chances of recovery are slight. Therefore, detecting whether an offset has been correctly evaluated or not could result in an immense improvement of the method. How can this be achieved? Theoretically, the offset feature is supposed to provide a first estimation of the particles displacement with an error smaller than one pixel. Therefore, the cross-correlation that is performed right after the offset evaluation must give a velocity evaluation within one half pixel. Consequently, if this requirement is not fulfilled, we can assume that either the window size used for the offset evaluation was incorrect, or that cross-correlation cannot be performed at the location for reasons such as a lack of particles or a major level of noise.

As a result such observations lead one to the following line of attack: at each location of the previously generated mesh a first pass is carried out using the first window

size selected by the user, providing a first guess of the velocity. Using this velocity as an offset, a second pass is then carried out. If the result of this second step is found to be within one pixel, the displacement is recorded. If this is not the case, the offset is set to zero and the same procedure takes place using the next window size elected by the user, and so on. A flowchart o thtis algorithm is presented in figure 3.15.

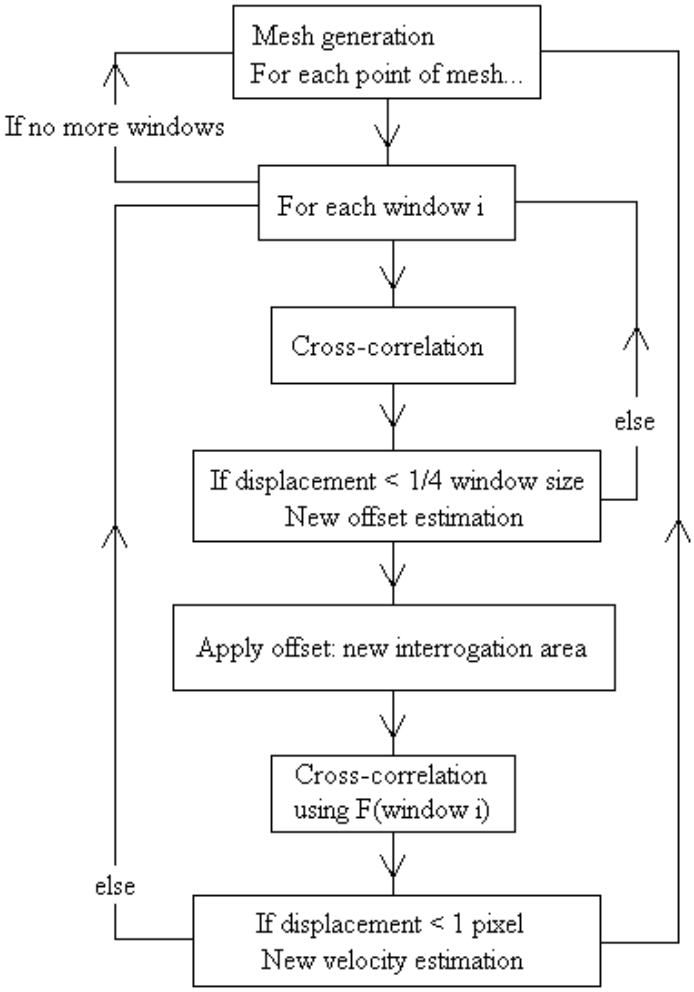

Figure 3.15: Off-check scheme

An alternative would be to check every possible offset and compare their accuracy before choosing the window size that is to be used. It would then seem natural to use the same window length for the second pass in the case of all window sizes Indeed an offset that would have been established using a 16x16 pixels window size and checked using a 8x8 pixels one would be more likely to be less accurate than an offset established

using a 32x32 pixels window size followed by a 16x16 pixels one. However this would be done to the detriment of the speed of the procedure.

3.6.2 Resulting improvement

The next image was obtained processing ALI8 images by means of the off-check scheme. The vector color corresponds to the window size with which the offset was computed: blue for16x16, green for 32x32, and red for 64x64.

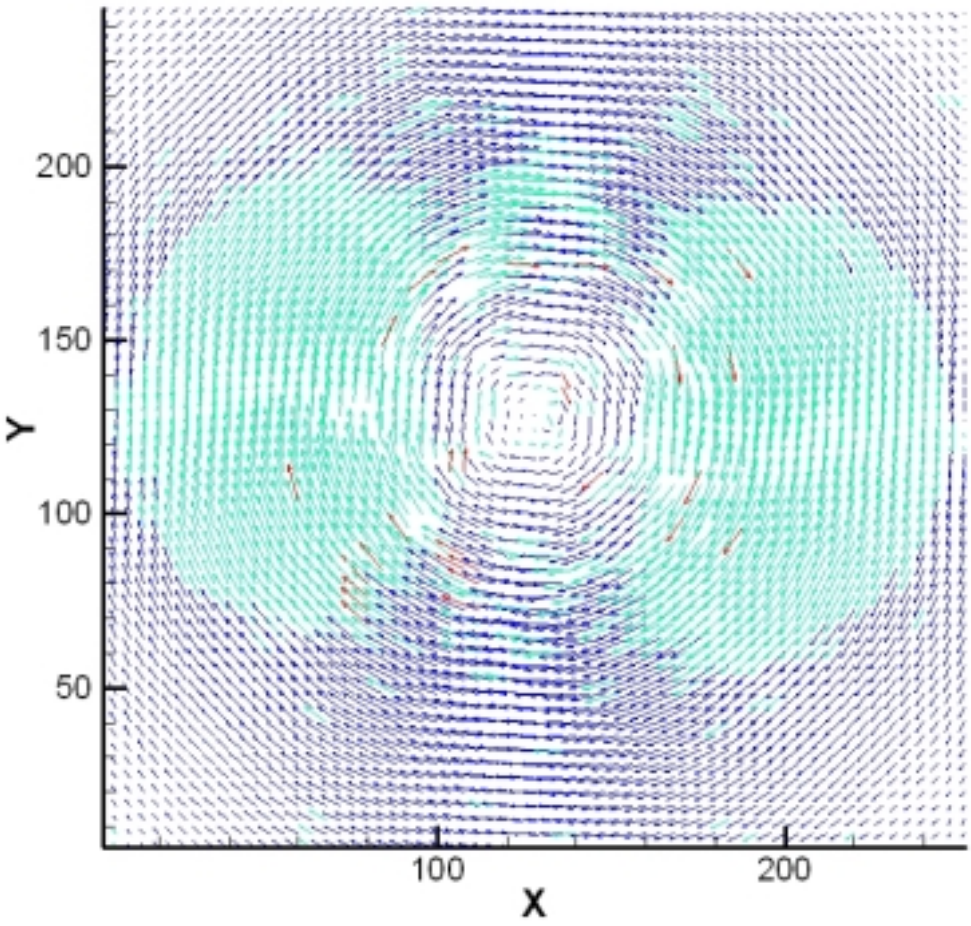

Figure 3.16: ALI image processed using the off-check scheme

As previously explained, this new method presents the ability to automatically select the window size depending on the offset accuracy. In this case, red vectors can be observed where high displacements are expected, whereas blue vectors are effectively

located where smaller displacements are expected. This method shows a remarkable ability to remove spurious vectors, and is therefore independent of the offset-based error, unlike usual DPIV schemes. Around 2.5 percents of the vectors were removed (corresponding to locations for which no reasonable offset value could be computed), and would need to be interpolated. However, further experimentations need to be carried on before the method uncovers its full potential.

3.7 Validation

Because of noise due to particles moving in and out of plane, to the optics and camera limitations to name a few sources of error, the cross-correlation can result in vectors that do not correspond to the actual flow field. In order to remove these erroneous vectors, a so-called validation scheme is usually applied as a post processor. Two methods were studied in the present effort: a simple straightforward dynamic mean value operator and a more advanced system based on artificial neural networks. Comparisons between the two different methods were carried out and are presented after the description of each scheme.

3.7.1 Dynamic mean value operator

3.7.1.1. Principle

This method is based on the work by Adrian and Meinhart (1995). It consists of selecting eight nearest neighbors around each vector to be validated. The vector is rejected if the difference between its magnitude and the average magnitude over its neighbors is above a certain threshold ε_{thres}. The magnitude can be replaced by the u and v components of the vectors, thus validating the vector direction.

For N=8 neighbors (when applicable), the following expressions are calculated:

$$\mathrm{A}(i,j)=\frac{1}{N}\sum_{n=1}^{N}U(n)$$

$$\text{and } S^2(i,j)=\frac{1}{N}\sum_{n=1}^{N}\left(A(i,j)-U(n)\right)^2 \quad (11.)$$

The criterion for data validation then is: $\left|A(i,j)-U_{2D}(i,j)\right|<\varepsilon_{thres}$,

where $\varepsilon_{thres} = C_1 + C_2\, S(i,j)$ with C_1, C_2 constants.

3.7.2 Using Neural networks

3.7.2.1. Introduction

Derou and Herault (1994), developed a more sophisticated validation scheme based on graph theory and pulsed neural networks. In this approach, the flow field is characterized by two matrices Q and C (where Q_{ij} represents the compatibility between the vectors i and j while C_{ij} represents the incompatibility associated with the vectors i and j). Using these two matrices, vectors are labeled as correct or erroneous based on a maximization of the vectors compatibility, using a specific kind of neural network. The advantage of their neural network is that it doesn't need any training. Its main inspiration is based on the human perception of a flow field.

3.7.2.2. About Neural Networks

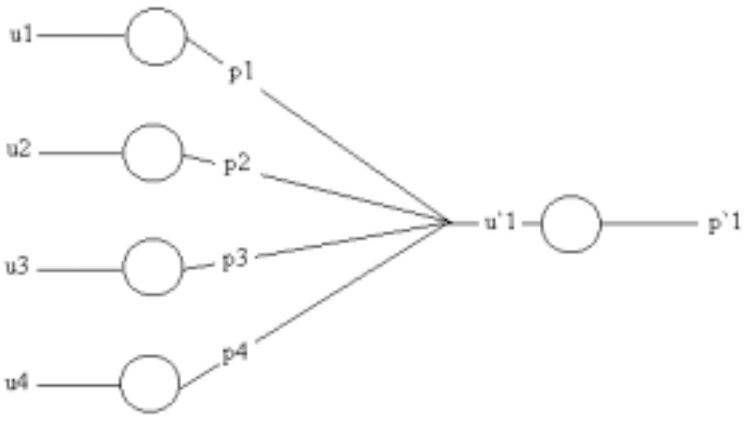

Figure 3.17: Synapses interconnections

The basic principle of the neural networks is shown below: It consists in multi-input nodes with weighted interconnections, as indicated. If $\mathbf{u_i}$ is the input and $\mathbf{p_i}$ the output of a neuron **i**, we can define a function H:

$$p_i^{(z+1)} = H(u_i^{(z+1)}) = \begin{cases} 1 & if \quad u_i^{(z+1)} > \alpha \\ 0 & if \quad u_i^{(z+1)} < \beta \\ p_i & otherwise \end{cases} \qquad (12.)$$

Parameters α and β are thresholds that describe the ability of a neuron to modify its output. If $p_i = 0$, the neuron is deactivated, otherwise, it is activated. In the pulsed neural network, the input of a neuron is a function of the output of the other neurons:

$$u_i^{(z+1)} = u_i^{(z)} + F_i(p_1^{(z+1)}, \ldots, p_N^{(z+1)}) \qquad (13.)$$

3.7.2.3. The matrices

Two matrices are created. Each coefficient m_{ij} of the n^2 matrix represents a comparison between vectors i and j.

The first matrix, Q

If the pair of vectors i and j contribute to the perception of the global movement, of the fluid elements that correspond to their respective positions there should be able to define a coefficient q_{ij} which will have high values; this coefficient is a function of three additional coefficients corresponding to: similarity, good continuation, and proximity.

The similarity coefficient:

It compares the lengths of the two vectors l_i, l_j, and their angle, as indicated by figure 3.18.

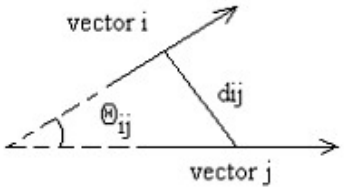

Figure 3.18: Similarity coefficient

A mathematical formulation of this coefficient can be:

$$S_{ij}\left(1-2*\frac{\theta_{ij}}{\pi}\right)*\left(1-\frac{\left|l_i-l_j\right|}{\max\left(l_i,l_j\right)}\right) \qquad (14.)$$

The proximity coefficient:

The proximity coefficient must vanish smoothly as the two trajectories are far from each other. We use: $D_{ij} = \exp\left(\frac{-d_{ij}^2}{2\sigma^2}\right)$, where σ_d^2 represents the standard deviation of all the distances over the image and d_{ij} is the distance between vectors i and j as shown in figure 3.18.

The good continuation coefficient:

It favors trajectories that contribute to the visual perception of streamlines. Given a vector i, we consider vectors j which are in a specific neighborhood (in dark gray on the following figure).

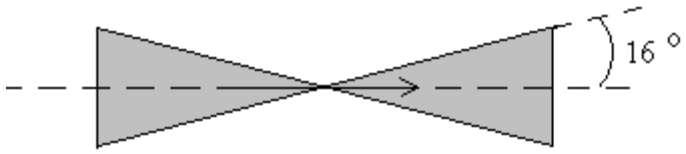

Figure 3.19: Good continuation neighborhood

Indeed, psycho-experimental studies have demonstrated that human eye perceived a discontinuity in an extension of two segments as soon as the angle between those two segments were more than nearly 16 degrees. The good continuation coefficient uses the radius of curvature as a parameter. We define ρ_{ij} as ρ_{ij} = di*dj/2 (see figure 3.20), and $\rho_{prevailing}$ is a mean of the ρ of the neighborhood. Finally,

$$G_{ij}^{goodcontinuation} = \exp(-\delta \cdot \frac{\left|\rho_{ij} - \rho_{prevailing}(i)\right|}{\rho_{prevailing}(i)}) \quad (15.)$$

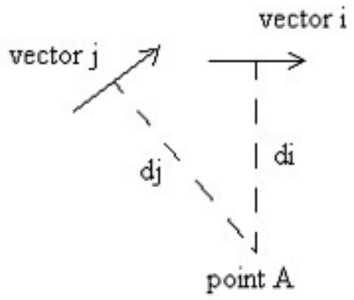

Figure 3.20: Distance to radius of curvature

The q coefficients

Finally, the actual matrix coefficients are set up using a weighted function of the three aforementioned coefficients. $q_{ij} = f(G_{ij}, D_{ij}, S_{ij})$, with $0 < q_{ij} < 1$.

The second matrix, C

C is a binary matrix: C_{ij} is set to 1 if two vectors are incompatible: if they cross each other, or if the angle between two vectors is larger than 90 degrees. Otherwise, C_{ij} is set to 0.

3.7.2.4. Formulation of the problem

In order to eliminate the bad vectors, let's consider the following problem:

Let's $p = (p_1, \ldots, p_N)$ be a vector, in which $p_i = 1$ if the trajectory i is labeled as a good one, and 0 otherwise. We have to find p maximizing E(p):

$$\begin{cases} E(p) = \sum_{i=1}^{N} \sum_{j=1}^{N} q_{ij} p_i p_j \\ \forall i, p_i \in [0,1], \forall i, j, p_i = p_j = 1 \Rightarrow C_{ij} = 0 \end{cases} \quad (16.)$$

This general case can be solved using a neural network following the standard scheme described above. In our case, the neuron i represents directly the vector i. Therefore, if this neuron is deactivated (i.e. $p_i = 0$), the corresponding vector is considered as erroneous. The function F mentioned earlier is chosen to respect the following conditions: a deactivated neuron can be activated only if its new state contributes towards an increase of the quality function E(p), and all the neurons incompatible with this one must be deactivated. The neural network synapses, after several iterations, converge to a maximum for E(p). This binary output corresponds directly to the vectors, labeled as validated or erroneous.

3.7.2.5. Neural networks algorithm

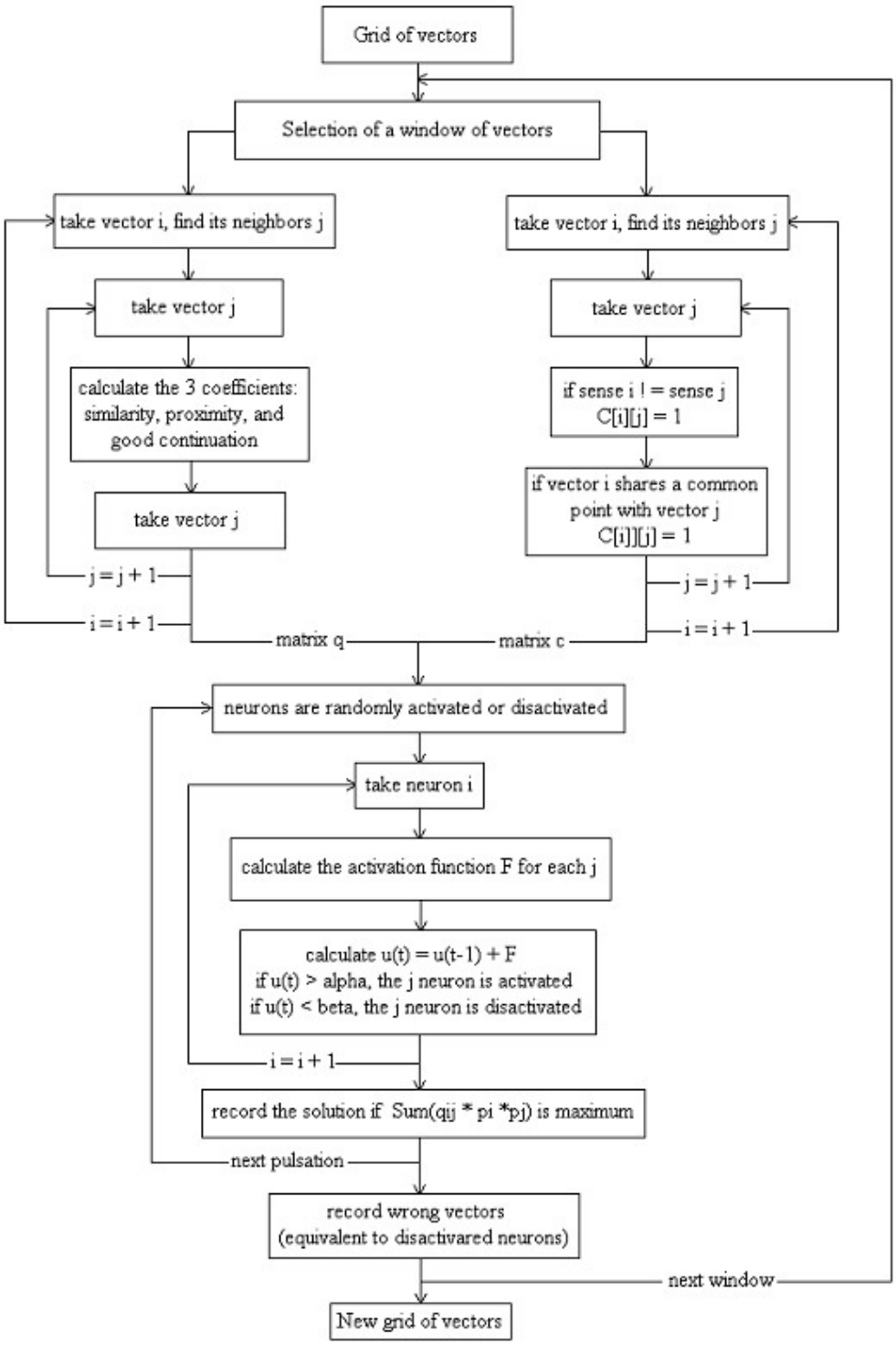

Figure 3.21: Neural Networks algorithm

3.7.3 Discussion

The comparison between the basic validation scheme and the one employing neural networks was realized employing images of the wake of a cylinder (Vlachos, 2000). The corresponding images were processed with the help of the ultimate scheme discussed in the previous sections of the present chapter. The windowing strategy involved two passes with 32x32 pixels interrogation windows, followed by a pass using 16x16 pixels windows, and finally a last pass by means of 8x8 pixels windows. The result of this procedure is shown in figure 3.22.

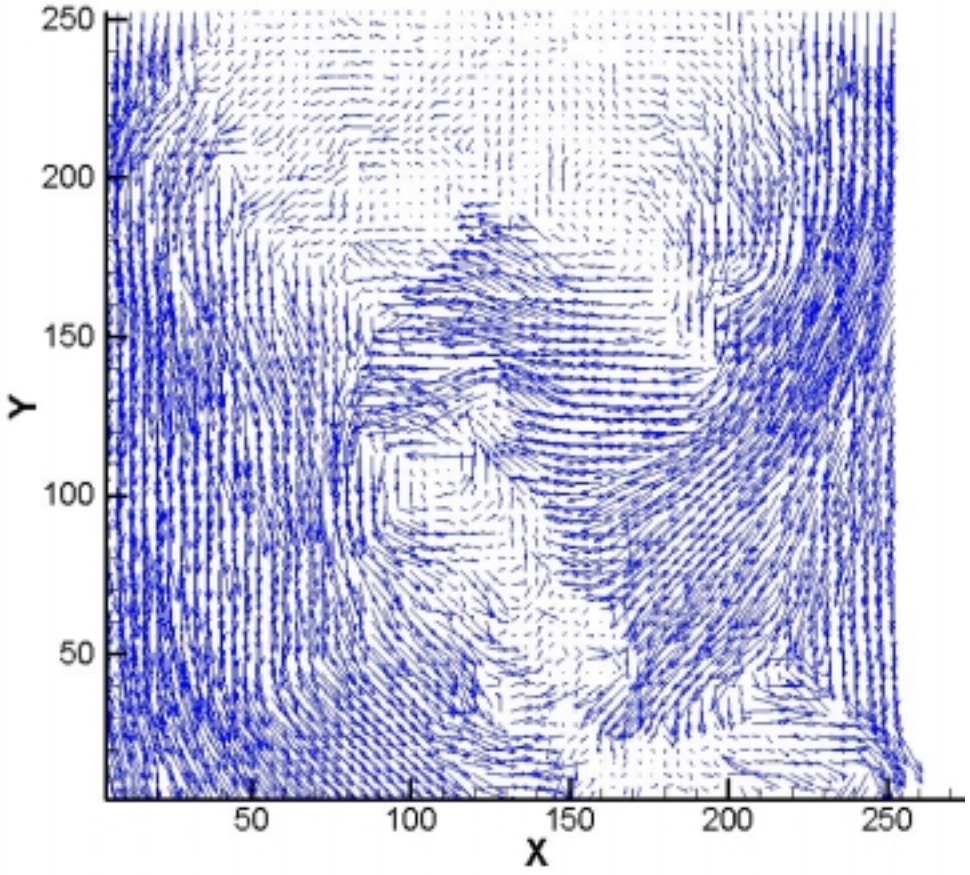

Figure 3.22: Image of the wake of a cylinder after cross-correlation

Visibly, the cross-correlation procedure produced several erroneous vectors. In the first place, we applied the dynamic mean value operator to this flow. In order to get reasonable results with this method, it was necessary to manually adjust the coefficients

$C_1$and C_2 of the basic validation scheme. The following figure (figure 3.23) presents the obtained results.

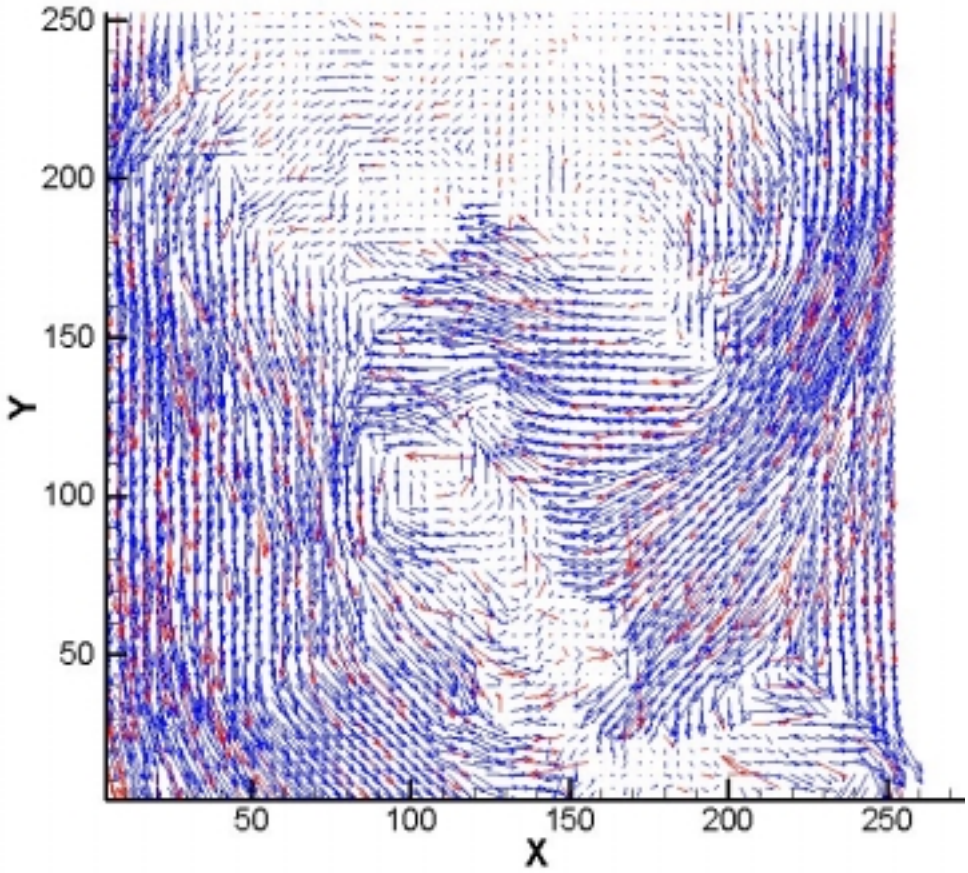

Figure 3.23: Flow-field after validation

The vectors in red are the one identified as wrong by the procedure. The blue ones are the remaining vectors. Manifestly, some obvious vectors were correctly identified as wrong. However, from our human perception, we also notice vectors that seemed correct that were removed. Also, some erroneous vectors still remain. One could use other coefficient in order to remove these; nevertheless, more vectors that were in fact exact would then be considered as stray ones.

Figure 3.24 depicts the neural networks performance. Clearly, fewer vectors were removed during the operation, preserving the original nature of the flow. In addition, vectors that appeared erroneous were effectively removed.

Therefore, it can be concluded that the neural networks perform better than the usual validating methods, especially while preserving the nature of the flow. Indeed, when an important number of vectors is removed, the image appears smooth after interpolation. However, the removed information cannot be retrieved; interpolation only fills the holes with the remaining information, but does not and cannot re-generate the flow! The essential drawback of neural networks being its slowness, the first method would be used in the case of clean outcome from the cross-correlation, while the neural networks would be preferred in the case of more intricate flows.

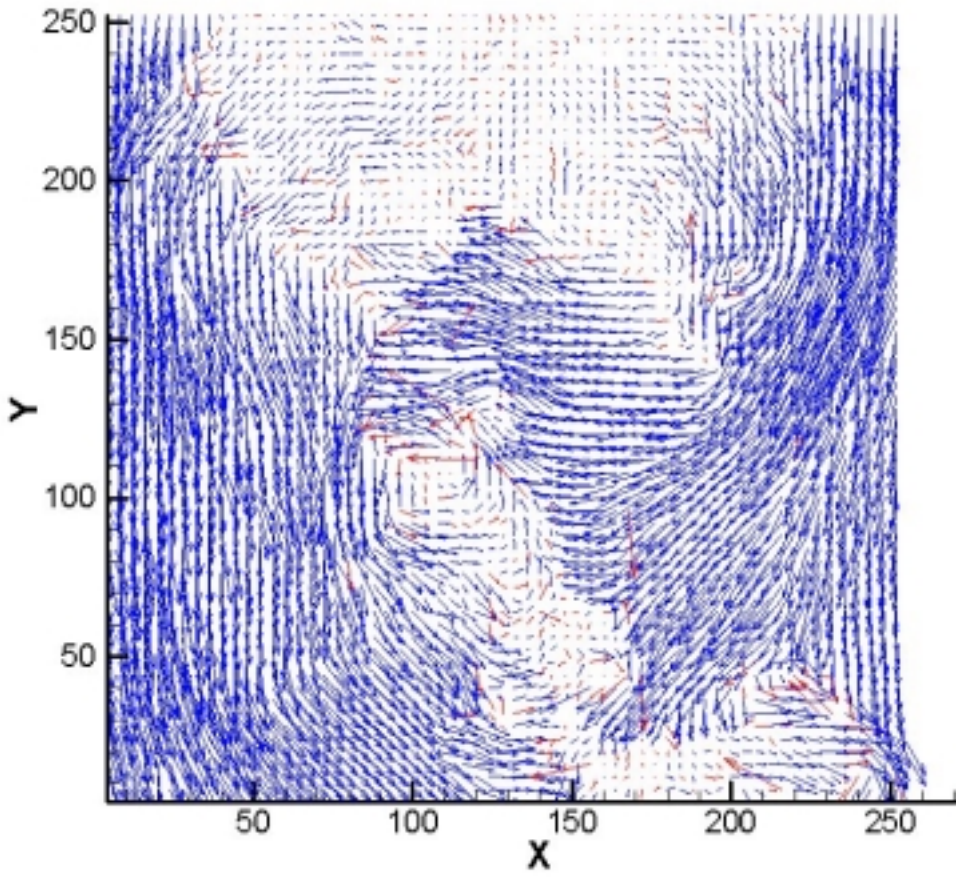

Figure 3.24: Validation by means of the neural networks

3.8 Interpolation, smoothing

Interpolation as well as smoothing is often necessary in order to be able to present smooth data. Indeed, a flow-field with empty areas is not extremely practical, especially in the case the derived parameters such as vorticity need to be computed. Therefore, basic but yet efficient schemes were developed in order to carry out interpolation and smoothing procedures

3.8.1 Interpolation

In order to speed up the procedure, only the vectors that were identified as wrong during the validation process are interpolated. The interpolation consists of a weighted average of validated vectors that are within a certain radius of the point to be interpolated. In our case, the interpolation function is defined as:

$$V(r_0) = \frac{\sum_{i=1}^{N} V(r_i) \cdot e^{-\alpha(r_i - r_0)^2}}{\sum_{i=1}^{N} e^{-\alpha(r_i - r_0)^2}} \qquad (17.)$$

Considering the same example as used during the validation, the recovered flow-field after validation by the neural networks and interpolation is shown in figure 3.25 (the interpolated vectors are shown in red):

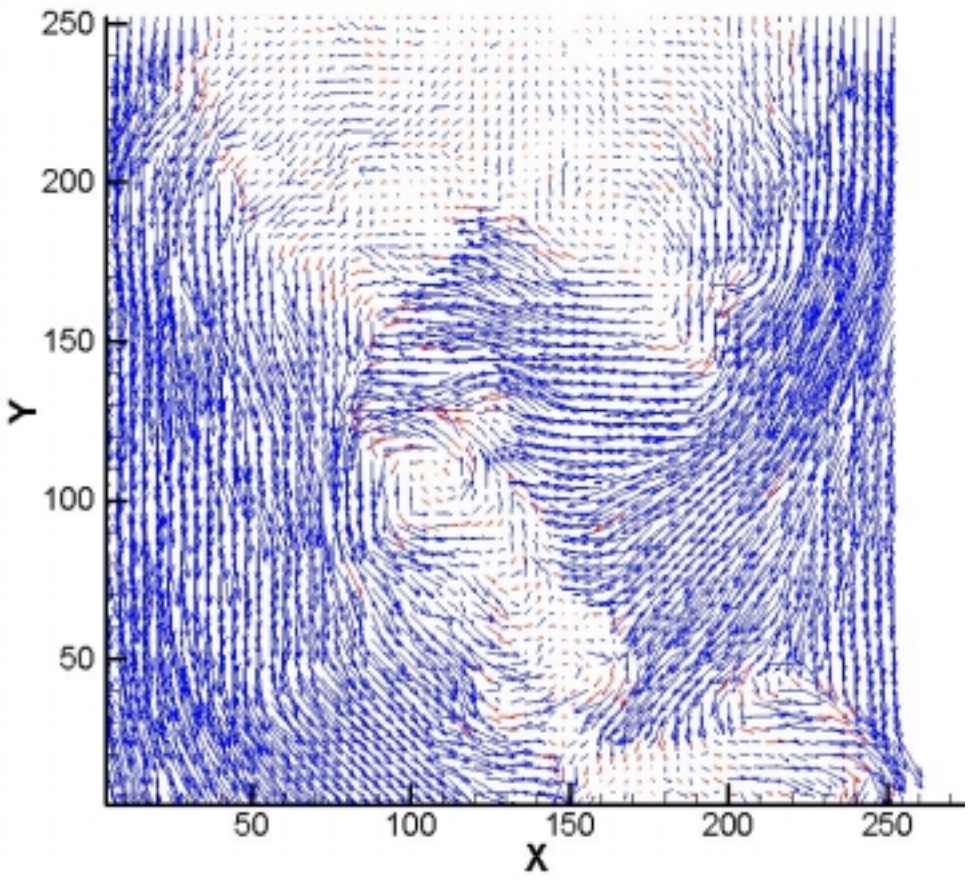

Figure 3.25: Flow-field after validation and interpolation

This weighted type of interpolation is fairly fast and efficient.

3.8.2 Smoothing

After both validation and interpolation, the flow-field is ideally free of stray vectors. Sometimes, especially when the cross correlation is implemented using large interrogation windows, the flow-field will look clean and smooth. In general however, this won't be the case. Therefore, in order to obtain nice-looking images, a procedure of smoothing is applied. The smoothing procedure is similar to an interpolation. Therefore, we used the same function as the one seen above for the interpolation. Each vector of the flow-field is smoothed one by one, taking into account its closest neighbors (always using the original vectors that were not smoothed). Depending on the α coefficient which

appears in the formula, the user can control the weighted average function, thus control the smoothing. Once α is chosen it stays constant for the entire flow field.

Smoothing, as interpolating, is a deceiving procedure. Indeed, they can both lead to beautiful flow fields, but can be thoroughly far from the reality. As a result, one should view cautiously any attractive DPIV result that went through validation and interpolation. The percentage of validated vectors can be an interesting gauge of the fraction of authenticity.

Smoothing the aforementioned results from the interpolation leads one to the following picture (figure 3.26):

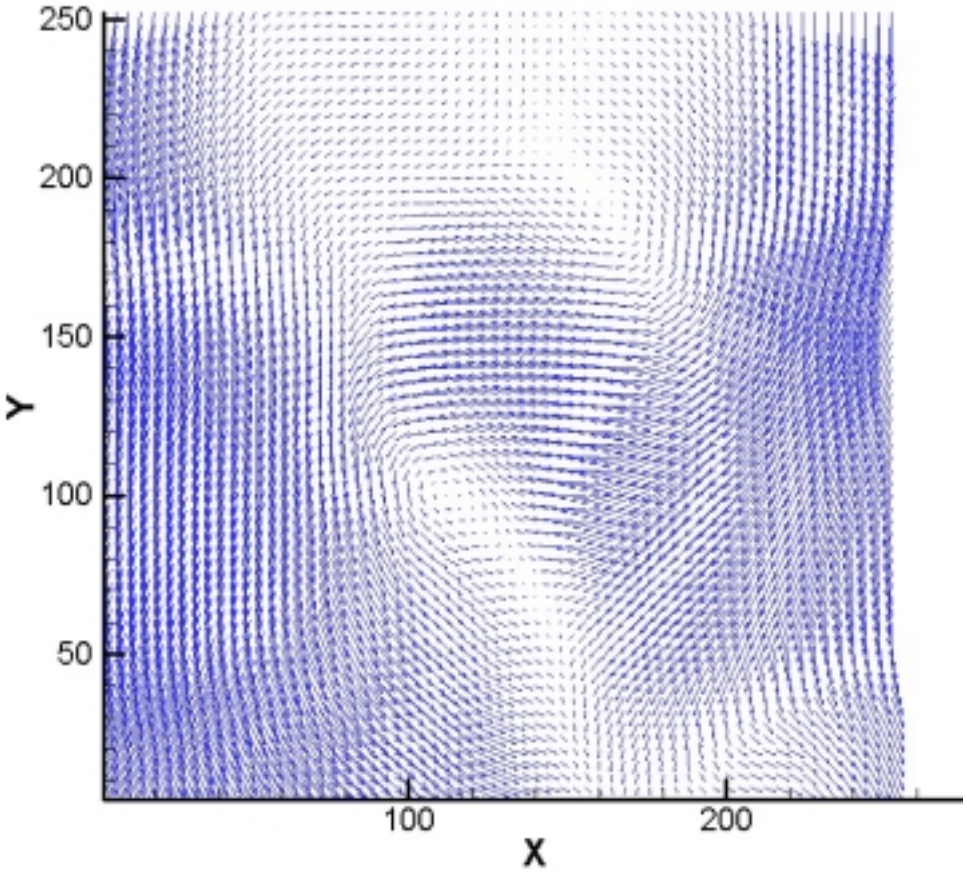

Figure 3.26: Flow-field after smoothing

3.9 Concluding DPIV scheme

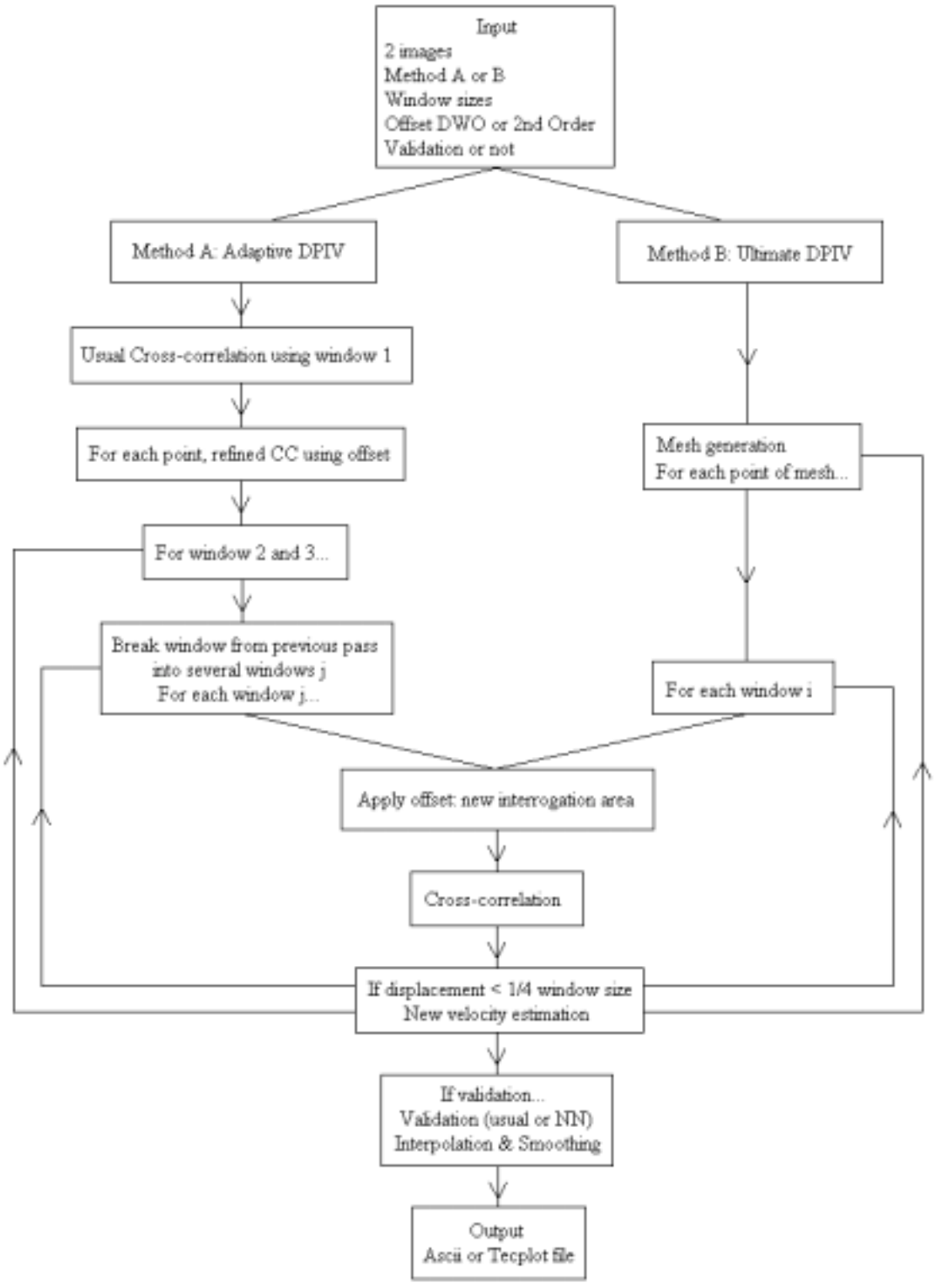

Figure 3.27: Global DPIV scheme

The algorithm presented in figure 3.27 shows the global DPIV scheme, after implementation of all the methods discussed in this section. It is to be compared to the basic system presented at the beginning of this chapter. The method presented here is much more flexible, and much more accurate, as it will be seen in the following paragraphs.

Chapter 4 DPTV Methods

In this section, we describe a particle-tracking scheme. It consists of two main steps: an identification of each particle in the flow for the pair of images, followed by a matching of each particle from the first frame with a particle of the second frame.

4.1 Particle identification

4.1.1 Image processing

In order to distinguish the actual particles present in the flow from noise or other phases like bubbles, particles, and solid bodies, the image processing tools described in the second chapter of this report are extremely useful. Depending on the flow properties, one needs to choose image-processing tools in order to keep as many flow tracers as possible while removing noise and the other phases. However, a global scheme will be presented here, which was proved to provide satisfactory results for most test cases.

4.1.1.1. Noise removal

In real cases, the images always present a level of background noise, due to the camera limitations, the depth of field, the laser beam Gaussian distribution. In order to distinguish actual particles from noise, one main image-processing tool is commonly used: the histogram thresholding. This method was previously described in the chapter 2.

4.1.1.2. Big particles segmentation

In the case of the presence of big particles (droplets, bubbles, solid bodies) in the image, it is necessary to remove these objects, which would appear as a cluster of particles if they were left in the image. This method, described in the second chapter of this work, can be used before or after having removed the background noise

4.1.2 Particle identifier

Two different schemes were developed: a standard method similar to the one proposed by Guezennec and Kiritsis (1990), followed, after analysis, by a maximum intensity identifier.

4.1.2.1. Guezennec and Kiritsis scheme

We accurately followed the scheme proposed by Guezennec and Kiritsis (1990). It consists in scanning the image pixel after pixel. For each pixel above a certain threshold, its four neighbors that were already scanned are examined. If none of them is above the specified threshold, a new particle number is assigned to the pixel. If they belong to one single particle, the current pixel is added to the list of pixels that belong to the particle. In some cases, the neighbor pixels belong to two different particles. In this last case, the "two" particles are actually one, and need to be reconnected. All the pixels belonging to one of them have thus to be assigned to the other, as well as the current pixel. This algorithm is very efficient, and links each pixel of the image above a certain threshold to a particle.

4.1.2.2. Maximum intensity identifier

A major drawback can be pointed out from the aforementioned method: its inability to distinguish a single particle from a cluster of particles in case these particles are very close to each other. In order to overcome this difficulty, we focused on the maximum intensity locations. Indeed, since a particle intensity distribution can be assumed to be Gaussian, a maximum must exist. After pre-processing as seen above, each pixel of the image is scanned using a 3x3 mask. If the center pixel of this mask corresponds to a local maximum or is saturated, the pixel is set to a saturated value. After the whole image has been scanned, a threshold is applied in order to keep only the saturated values. This process leaves only local maxima and plateaus in the image, leading to the corresponding particles.

Thus, the algorithm is significantly improved in order to identify all the particles present in the flow and accounts for overlapping or neighboring particles that would appear as one if conventional processing were used.

4.1.2.3. Median filtering

Another approach is the use of a combination of a median filter with local dynamic thresholds, a variable-size masking method and finally a particle erosion filter in order to identify all the particles present in the flow. Like the previously mentioned maximum intensity identifier scheme, this method also accounts for overlapping or neighboring particles and represents a major enhancement compared with usual particle identification schemes.

4.2 Centroid calculation

For each detected particle, the coordinates of its centroid are evaluated, based on the original image. Adrian and Yao (1985) showed that particle images could be approximated as Gaussian:

$$A_i = A_c e^{-br_i^2} \qquad (18.)$$

Based on this assumption, a three-point Gaussian estimator can be derived in order to approximate the particle center:

$$x_c = x_0 + \frac{\ln G(x_0-1,y_0)-\ln G(x_0+1,y_0)}{2(\ln G(x_0-1,y_0)+\ln G(x_0+1,y_0)-2\ln G(x_0,y_0))} \qquad (19.)$$

Where G(x, y) is the intensity of the pixel located at (x, y). Particle tracking algorithms commonly employ this approximation. However, the use of CCD sensors inherently introduces errors due to the leakage effect and the read-out noise resulting in an incorrect estimation of the particle center. To the best of the authors' knowledge, there is no model that simulates numerically the effect of the saturation of the pixels and the leakage effect. However, by employing the CMOS camera we eliminate these errors.

Thus the intensity value of non-saturated pixels corresponds to the true intensity. As a result, we can analytically reconstruct the true two-dimensional Gaussian intensity distribution subject to the assumption that we have unsaturated pixels. This can be achieved by employing the equation seen above with:

$$r_i^2 = (x_i - x_c)^2 + (y_i - y_c)^2 \quad (20.)$$

Here (x_i, y_i) are the non-saturated pixel positions. In effect, we resample in a continuous domain in order to retrieve the particle centroid. The unknowns are $\boldsymbol{x_c}$, $\boldsymbol{y_c}$, $\boldsymbol{A_c}$ and $\boldsymbol{b}$. Four equations corresponding to four unsaturated pixels of the particle can be derived and used to evaluate the true coordinates of the centroid ($\boldsymbol{x_c}$, $\boldsymbol{y_c}$) and $\boldsymbol{A_c}$, $\boldsymbol{b}$. One advantage of this approach is the fact that it can be employed also in the presence of a plateau, where the particle diameter exceeds three pixels. As a result, the only uncertainty is introduced from the imaging sensor.

4.3 Velocity estimation

Once the particles from each frame have been identified, particles from the first image are paired with the ones from the second image, using four different steps, which can be used independently, or one after the other depending on the user's will. When the cross-correlation gives accurate enough velocity estimations, the first step enables the evaluation of most of the particles present in the flow field. Once particles have been paired in one of the multiple passes, they are removed from the list of particles and only the particles that could not be matched are further processed. Once particles have been paired, the displacement follows by subtracting the centroid position of the particle in the second frame to the centroid location of the corresponding particle in the first frame.

4.3.1 First step, Guezennec and Kiritsis approach

A linear interpolation based on the velocities from the cross-correlation provides a prediction of the expected location of each particle in the second image. If one and only

one particle is found within one pixel of the expected position, the new velocity is calculated and the paired particles are removed from the list of particles.

In their 1990 paper, Guezennec and Kiritsis then use a plain tracking, enlarging the radius of search up to a prescribed limit. However, other refinements can be considered, as seen in the following.

4.3.2 Second step, cross-correlation refinement

Linear interpolation introduces an error, and in the case of strong gradients, this error on the velocity can be significant. Since the search for the matching particle is done within one pixel, a slight error on the velocity can have important consequences on the pairing.

The cross-correlation refinement is used right after the first step. For the remaining particles, a refined correlation is performed, centering an 8x8 cross-correlation window at the particle location in frame one. Using the previously interpolated velocity as an offset, the second cross-correlation window is centered at the expected location in frame two. Since the refined cross-correlation takes place at the exact location of the particle, the velocity prediction is independent of any interpolation. Similarly, to the precedent step, a search is performed by means of this refined velocity, followed by a particle pairing, if only one particle from frame two is found within one pixel of this new location.

4.3.3 Third step, Cowen and Monismith approach

For the remaining particles, a third step is employed, similar to the one proposed by Cowen and Monismith (1997) where a 9x9 pixels window is centered at the particle location, and another one at the expected location of the particle in the second image. Based on the results of the cross-correlation of these two images, a 3x3 window is centered on the second image; once again, particles are paired in the case of the presence of one single particle in this last window. In practice, the third step is rarely required and the majority of the particles are paired within the previous steps.

4.3.4 Fourth step, plain Tracking

The fourth step simply consists in searching for the nearest particle to the expected location within a certain radius. The expected location can be initialized by the cross-correlation, or without any initialization. In this last case, the particles from the first frame will be paired with the closest particle from the second frame. This scheme can eventually be useful when particles move slowly from one frame to the other, or when the results from the cross-correlation are questionable.

4.4 Sample results

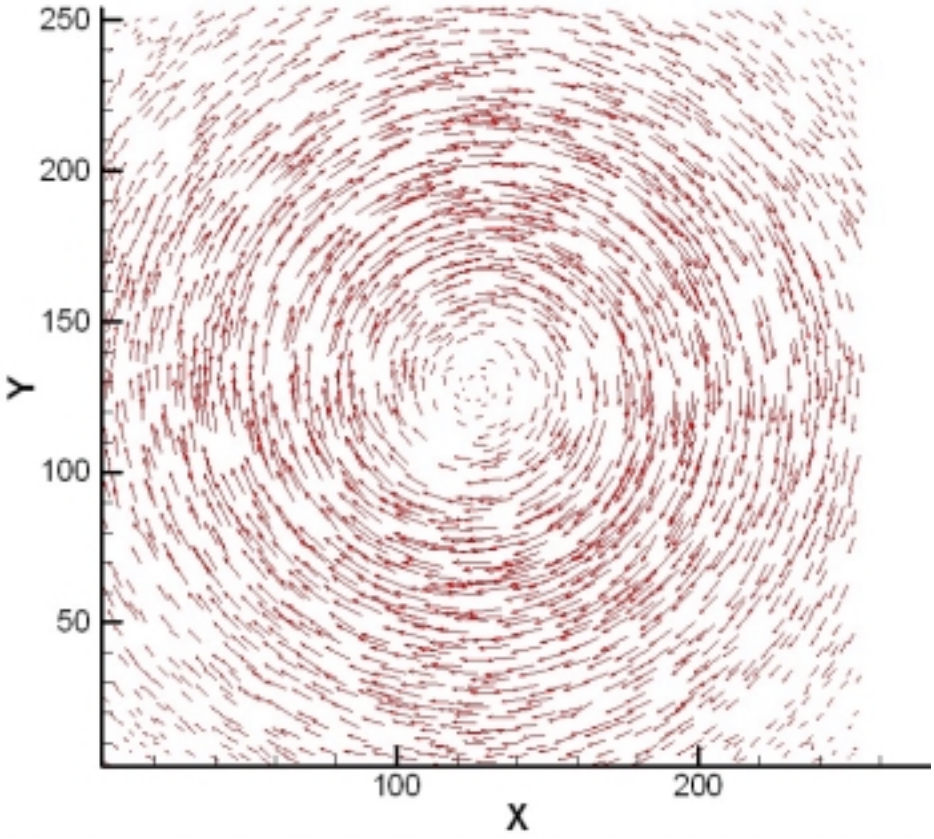

Figure 4.1: Results of the tracking for ALI images

The picture presented in figure 4.1 gives an idea of the kind of images given by the tracking. The difference with the cross-correlation is essentially that the position of the points is randomly distributed throughout the whole flow-field. Also, the rotational

character of the flow field is preserved, alleviating the linearity inherent in the cross-correlation, giving a more representative realization of the flow.

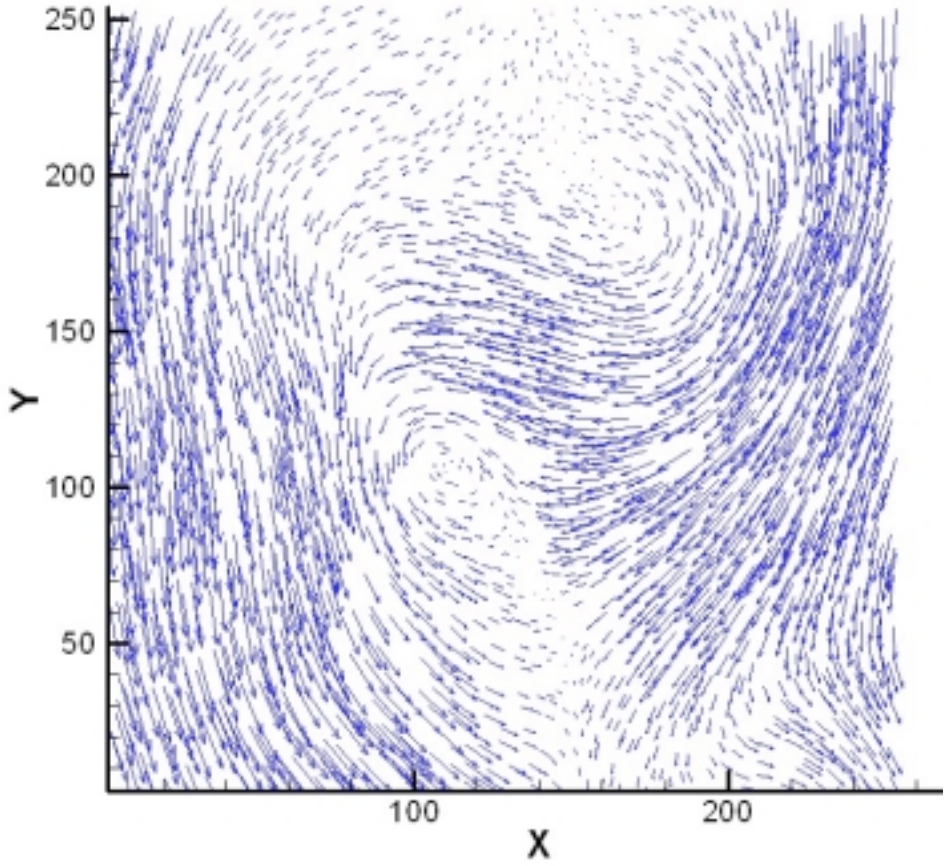

Figure 4.2: Wake of the circular cylinder.

Figure 4.2 is to be compared with the ones given by the cross-correlation. The figure was obtained after smoothing, which can be used, as well as the validation, along with the hybrid particle tracking. The natural wavy character of the flow is resolved generating more physically representative measurements than cross-correlation.

Chapter 5 Statistics and comparisons

This chapter is dedicated to the comparisons of the different methods presented in the two preceding chapters. In order to determine the quality of the proposed methodologies, Monte-Carlo simulations were preformed for different versions of our DPIV and DPTV systems, along with one of the best DPIV software's in the market.

Three major lines of comparisons were defined: uniform displacements, test with ALI images, and finally peak-locking effect (namely, the tendency of the cross-correlation evaluation to lock on the closest integer value).

5.1 The compared software

Table 5.1 is referencing the different versions that were compared during this effort. One section deals with cross-correlation and another with hybrid particle tracking. Since the particle tracking presented throughout the present work was the only available version, its performance was discussed comparing it to the cross-correlation schemes. However, differences between these two methods are significant, so that hybrid and cross-correlation should be considered as two different and complementary tools rather than two ways to achieve the same result.

Concerning the cross-correlation, the main implementations investigated were the basic scheme by Gharib, the version that was developed during this work, and Dantec's. Dantec Dynamics is a Danish group, leader in DPIV technology, and their program can be considered as a top-performing software package used as reference for the following statistical analyses. Three main interrogation schemes were employed: a 32-32-16 windows system was generally applied, but a scheme employing 64-64-32-16 pixels interrogation windows was used when expected displacements were above 8 pixels (ALI images with 8 pixels maximum displacement), and in order to test the performance of the system in resolving smaller length scales, a 32-32-16-8 method was considered. These versions were evaluated using the two types of offsets described earlier.

Table 5.1: Compared versions of the diverse software

Acronyms	*Scheme*	*Interrogation windows*	*Offset*	*Validation*	*Developer*	*Additional*
Cross-Correlation						
UCS	ultimate CC	64-64-32-16	***second order***	No	Abiven/Vlachos	regular offset on sides
UCNR	ultimate CC	16-32-64-32-16	***regular***	No	Abiven/Vlachos	scd order offset on sides
UCN	ultimate CC	64-64-32-16	***regular***	No	Abiven/Vlachos	scd order offset on sides
UBS	ultimate CC	32-32-16-8	***second order***	No	Abiven/Vlachos	regular offset on sides
UBN	ultimate CC	32-32-16-8	***regular***	No	Abiven/Vlachos	scd order offset on sides
UAS	ultimate CC	32-32-16	***second order***	No	Abiven/Vlachos	regular offset on sides
UANR	ultimate CC	16-32-32-16	***regular***	No	Abiven/Vlachos	scd order offset on sides
UAN	ultimate CC	32-32-16	***regular***	No	Abiven/Vlachos	scd order offset on sides
OUC	4 adaptive passes CC	64-64-32-16	***regular***	No	Abiven/Vlachos	
OUB	4 adaptive passes CC	32-32-16-8	***regular***	No	Abiven/Vlachos	
OUA	3 adaptive passes CC	32-32-16	***regular***	No	Abiven/Vlachos	
GA	1 pass CC	16	***no***	No	Gharib	
DCSH	adaptive CC + high accuracy module	64-64-32-16	***second order***	No	Dantec	
DCNH	adaptive CC + high accuracy module	64-64-32-16	***regular***	No	Dantec	
DBSH	adaptive CC + high accuracy module	32-32-16-8	***second order***	No	Dantec	
DBS	adaptive CC	32-32-16-8	***second order***	No	Dantec	
DBNH	adaptive CC + high accuracy module	32-32-16-8	***regular***	No	Dantec	
DBN	adaptive CC	32-32-16-8	***regular***	No	Dantec	
DASH	adaptive CC + high accuracy module	32-32-16	***second order***	No	Dantec	
DAS	adaptive CC	32-32-16	***second order***	No	Dantec	
DANH	adaptive CC + high accuracy module	32-32-16	***regular***	No	Dantec	
DAN	adaptive CC	32-32-16	***regular***	No	Dantec	
Hybrid/Tracking						
T	3&4 pt Gaussian + center of mass			No	Abiven/Vlachos	Initialized using UCN or UBN
T3	3pt Gaussian			No	Abiven/Vlachos	Initialized using UCN or UBN
T34M	3&4 pt Gaussian + center of mass			No	Abiven/Vlachos	Initialized using UCN or UBN
T3M	3pt Gaussian + center of mass			No	Abiven/Vlachos	Initialized using UCN or UBN
TM	center of mass			No	Abiven/Vlachos	Initialized using UCN or UBN

In order to compare the actual repercussion of the ultimate system with the standard cross-correlation schemes, we analyzed two versions (UCN and OUA) the core of which was exactly the same, the only difference being that UCN calculates the offset at the exact same location as the final velocity estimation, while standard cross-correlation methods break windows into smaller ones, resulting in an approximation of the offset at a different position than the final evaluation

5.2 Uniform displacements

Two major computer experiments were carried out concerning uniform displacements: one with interrogation window sizes successively being reduced to 16x16, and the other to 8x8 pixels. This was necessary due to the difference between the two schemes. The first one is expected to give a better accuracy. Indeed, more particles are susceptible to be found within the window, consequently, the final velocity is averaged taking into account more tracers. On the other hand, smaller windows reduce spatial averaging effects thus allowing the resolution of smaller length scales.

5.2.1 Uniform displacements resolved with16x16 window size

5.2.1.1. Global performance

A first comparison was carried out with the basic scheme presented in the third chapter of this work (GA) along with two schemes using the dynamic offset feature (UAN and DANH), as well as the hybrid technique (T). The results of this comparison are plotted in figure 5.1. The advantage of the offset is apparent. Indeed, after 0.5 pixels displacement, the error for the basic scheme (GA) keeps on increasing, while for all the dynamically adaptive schemes (three other methods) it goes down until the next integer is reached, and repeats the same pattern independent of the displacement. The mean error that appears on the right of the figure shows a difference of an order of magnitude between GA (mean error of 2) and the other schemes (mean errors below 0.1). This shows the profound influence of the dynamic window offset feature. It also illustrates the high accuracy of the tracking. Indeed, tracking every particle without any mistake is a task that is far from easy. Many errors can occur along the way, such as confusing one

particle with a pattern of particles, or non-identification of a particle, or identification of a particle that was actually noise.

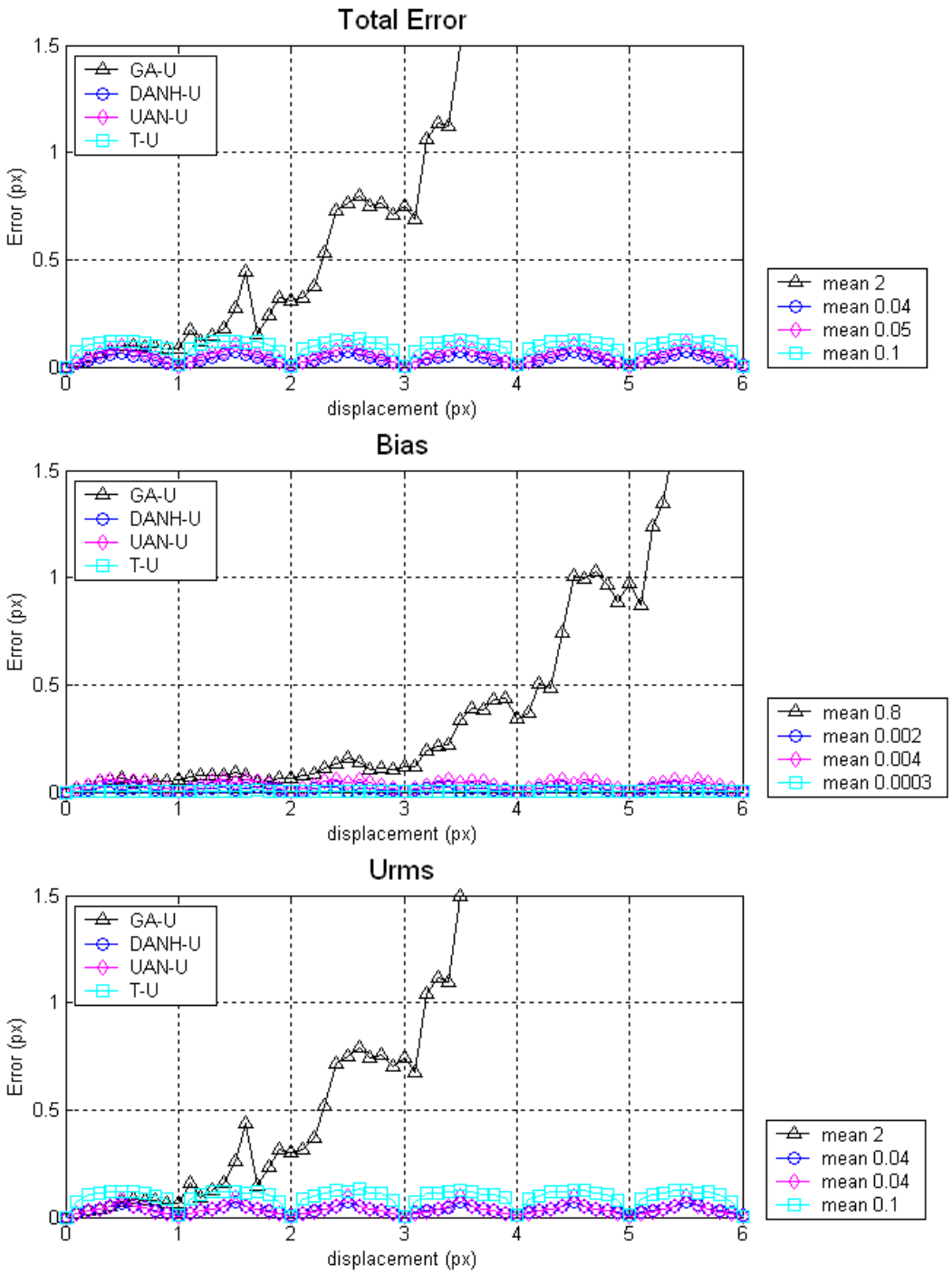

Figure 5.1: Basic scheme versus offset schemes

5.2.1.2. First and second order offsets

In this section, four cases were studied: two different types of offsets for two different implementations.

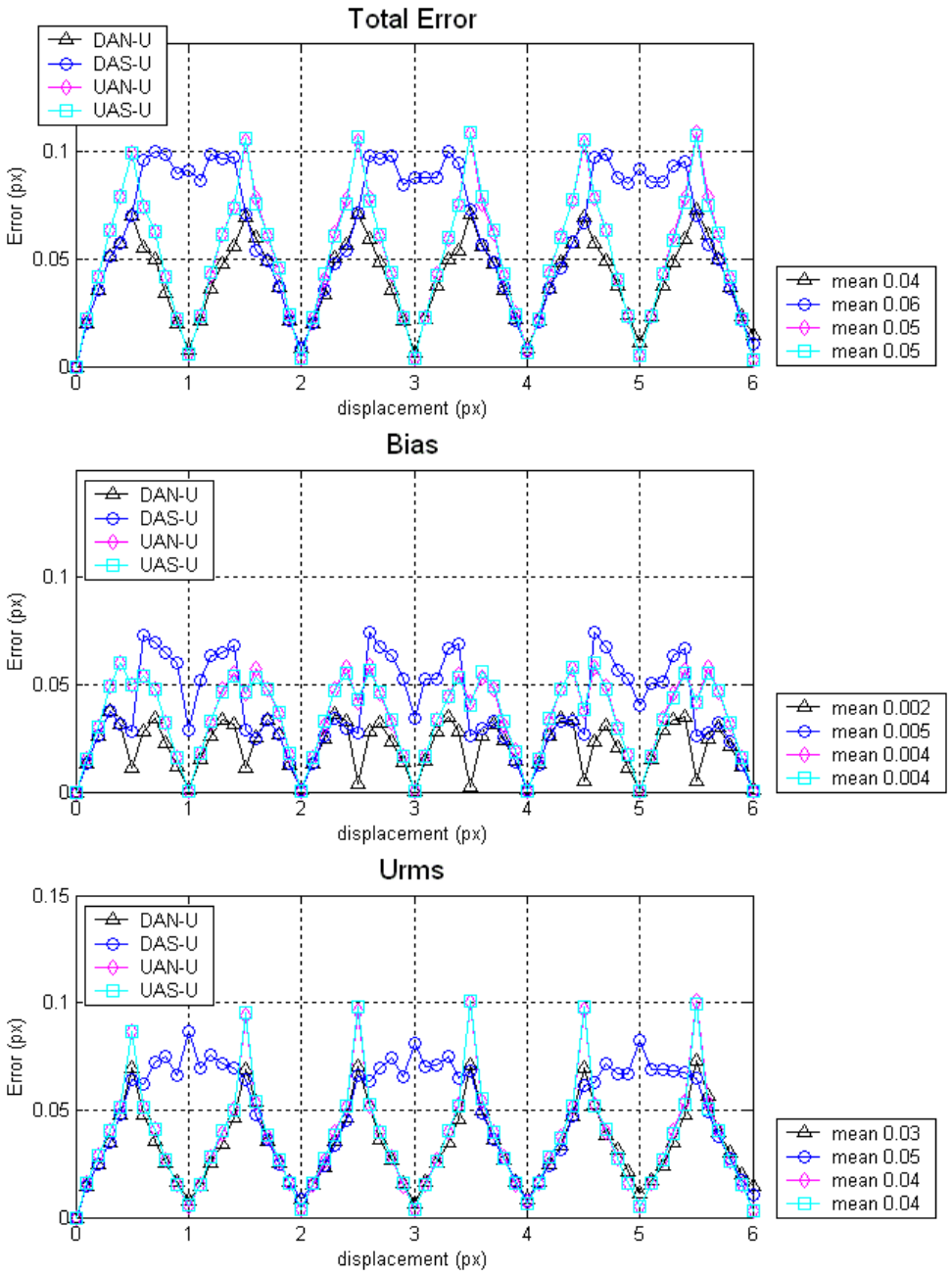

Figure 5.2: U and D with normal and second order offsets

As shown in the figure 5.2, U and D schemes perform very similarly, except for the 0.5 pixels, where the U scheme seems to be subject to a peak locking effect, as it will be explained further in this chapter. Second order and normal offsets perform equally in the case of our software, which was expected since the second order is expected to improve the results in the case of rotational motion. However, the use of the second order window offset for the case DAS shows an obvious problem in the implementation of this feature. This is very likely to be explained by the following:

Let's consider a first pass where the displacement would be 2.345 pixels. The second order offset actually consists in two offsets, one upward (U), and one backward (B), the value of which can be calculated by: (2.345/2). However, the offset needs to be an integer, in order to shift the interrogation window by a certain amount of pixels. Therefore, the offsets will be: U = nearest integer (2.345/2) = 1, and B = -nearest integer (2.345/2)= -1. The total offset then is T = U-B=2. T, by definition of the normal offset, is also equal to T=nearest integer (2.345)=2. Now, let's consider a first pass with a displacement of 2.674 pixels. This time, U = nearest integer (2.674/2) = 1, and B=-nearest integer (2.674/2)=- 1. The problem comes from the fact that the total offset T_m = U-B=2 is different from T=nearest integer (2.674)=3. The right way to do it (as implemented in the Uniform scheme) is to calculate B from: B=U-T=1-3=-2.

This mistake, in a software designed by a team of engineers illustrates the complexity of the adaptive DPIV procedure implementation, where each detail has to be understood and validated in order to achieve a significant performance improvement..

5.2.2 Uniform displacements down to 8x8

Figure 5.3 was obtained using window sizes going down to 8x8 pixels. As expected, the mean error is higher compared to 16x16 pixels windows: 0.1 for the former case, and 0.05 for the latter, using the ultimate scheme. Therefore, it can be said that using 8x8 pixels, we pay the price of resolving smaller length scales by a higher resulting error.

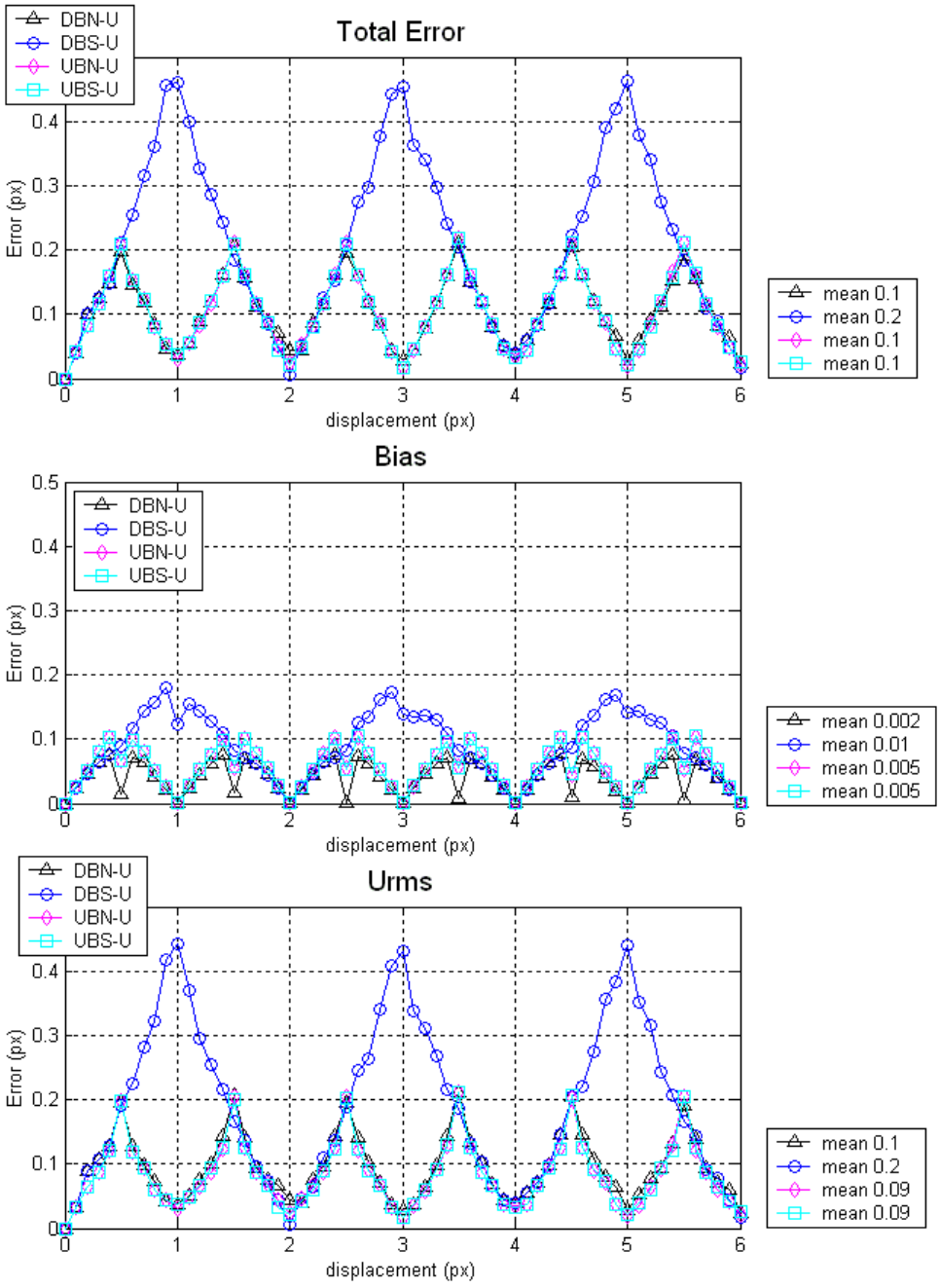

Figure 5.3: Error analysis going down to 8x8 interrogation windows

Interestingly, the blunder on the second order offset inherent to Dantec's software is now amplified, while it was previously damped, when using 16x16 windows. The object of the following plots (presented in figure 5.4) was to identify the influence of a novel high accuracy module proposed by Dantec. Proprietary information issues deprived

us from the details of this algorithm, which we compared with the developed software. Visibly, the high accuracy module enhances the inaccuracy by orders of magnitude.

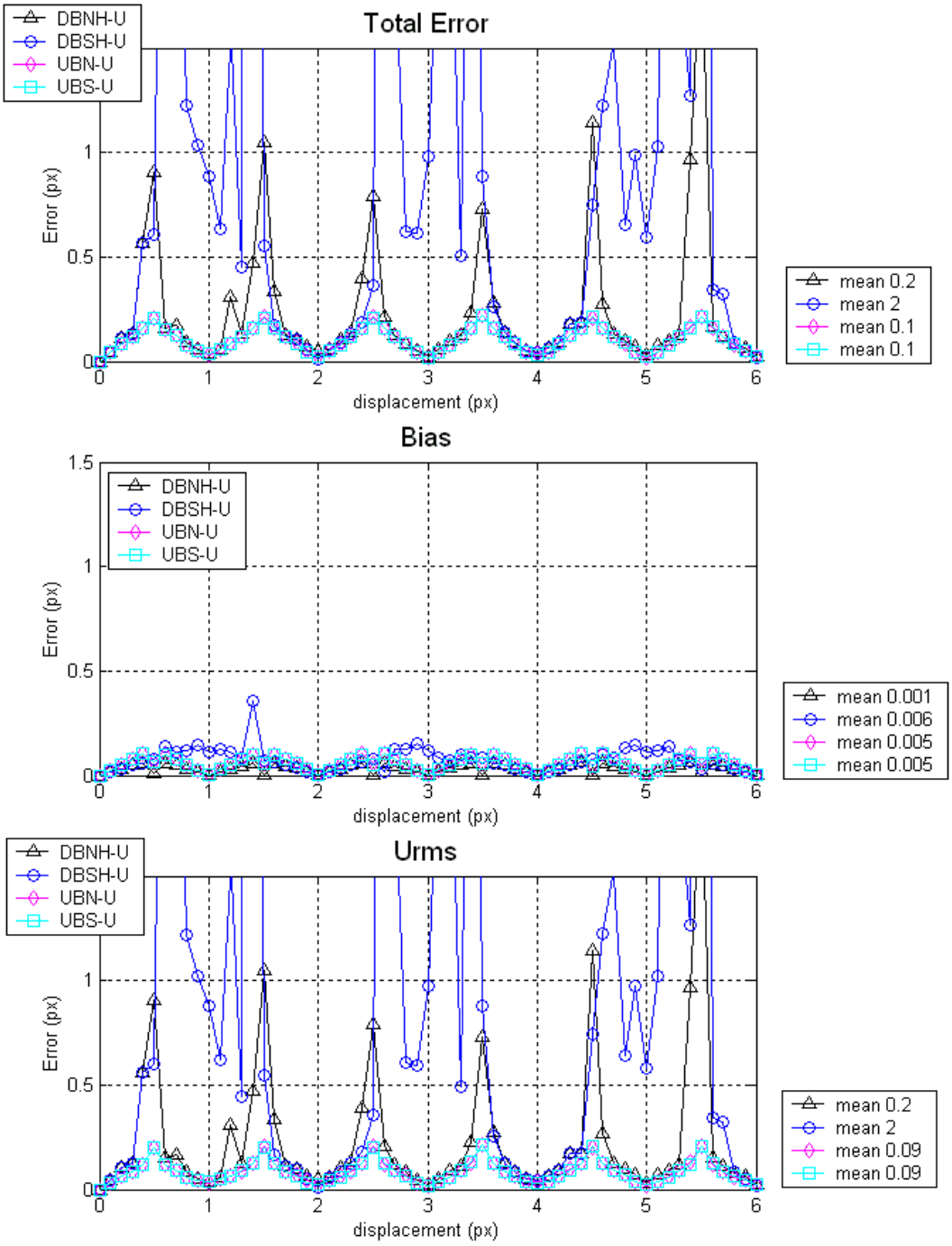

Figure 5.4: Results of the investigation concerning the high accuracy module

5.2.3 Comparisons of several versions of the developed software

As it can be observed from figure 5.5, results from one version of the software we developed to the other show significant consistency.

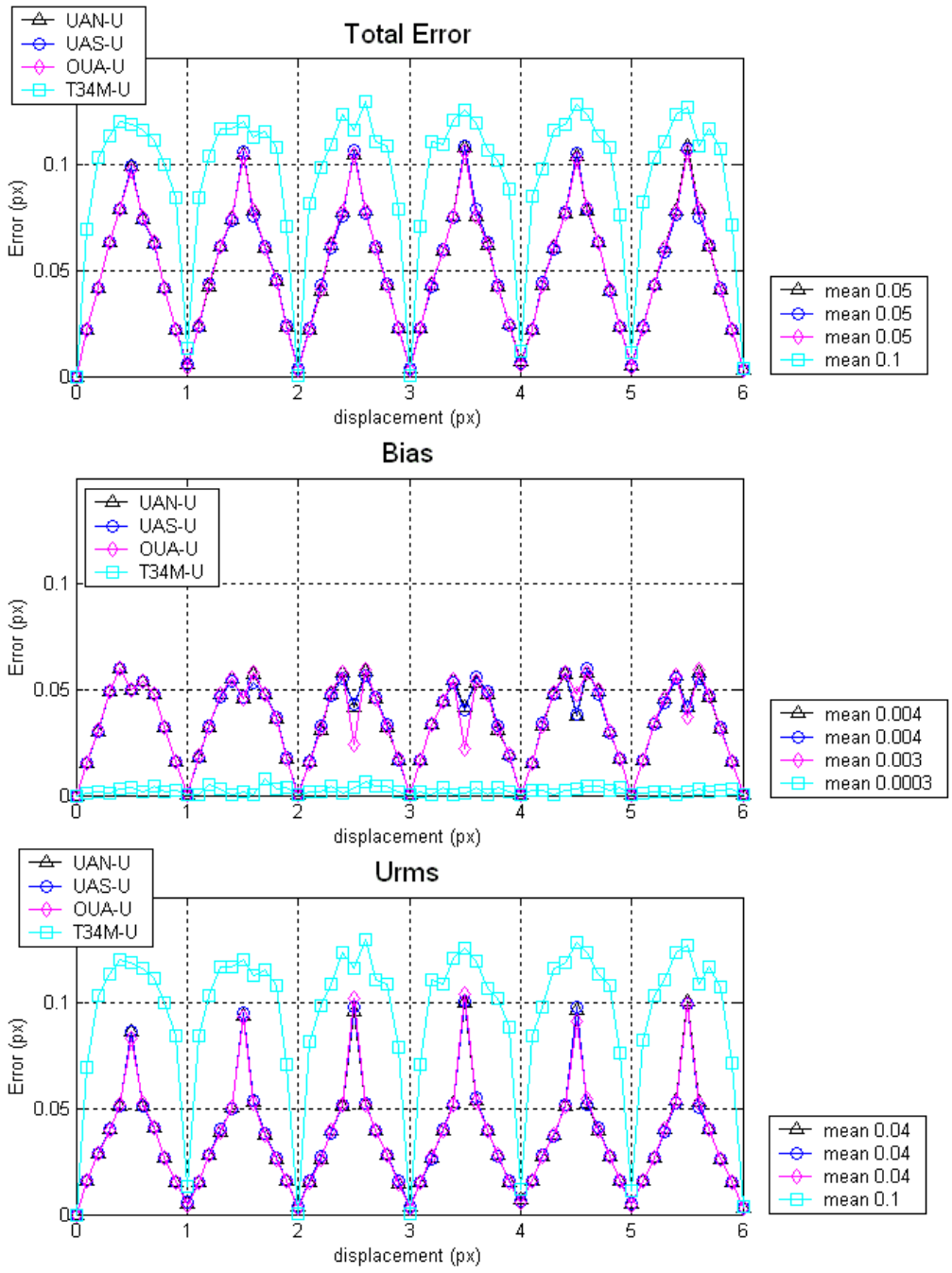

Figure 5.5: Several versions of the developed software

This was expected, due to the uniform flow field that was the object of this analysis. Indeed, the second order offset is not supposed to perform better than the regular offset in this case (but not worse either), neither is the ultimate scheme versus the adaptive (OUA) version. The tracking scheme presents a highest error, with a mean of 0.1 versus 0.05 for the cross-correlation. However, it needs to be emphasized that the hybrid gives the same results when initialized with data obtained using 16x16 and 8x8 windows. Therefore, the use of 16x16 windows in order to initialize the tracking scheme seems to prevail here. Indeed, using smaller windows implies more inaccuracy in the results as well as computational inefficiency. Also, let's highlight the fact that the mean error is nearly zero while the total error is primarily attribute to random error. This element implies an alleviation of the peak locking effects (this will be discussed in detail in a following paragraph), which by it self is a significant improvement on the accuracy of the system.

5.2.4 Particle-tracking

Figure 5.6 shows a larger error when a center of mass is used as an identifier (For the TM case, the centroid of a particle is calculated based on a center of mass of the pixels belonging to this particle). The smallest error was obtained without any center of mass identification (T34 scheme), but also without taking into account particles with several saturated pixels. The only way we found to resolve them accurately was by using a center of mass.

The difference between T34M and T34 is small, especially if we consider the fact that T34 tracks only those particles with a maximum of one non-saturated pixel, while T34M tracks every possible one. However, the use of T34M takes more particles into consideration, since centroids of particles without any saturated pixel (resolved using a 3 points Gaussian estimator), particles with a single saturated pixel (resolved using a 4 points Gaussian estimator), and particles with several saturated pixels (resolved using a center of mass) are identified.

It is extremely interesting to notice that the error almost exclusively corresponds to the rms error. The bias error is remarkably flat and low. This might be due to a random distribution of the velocities that compensate each other when calculating the mean error.

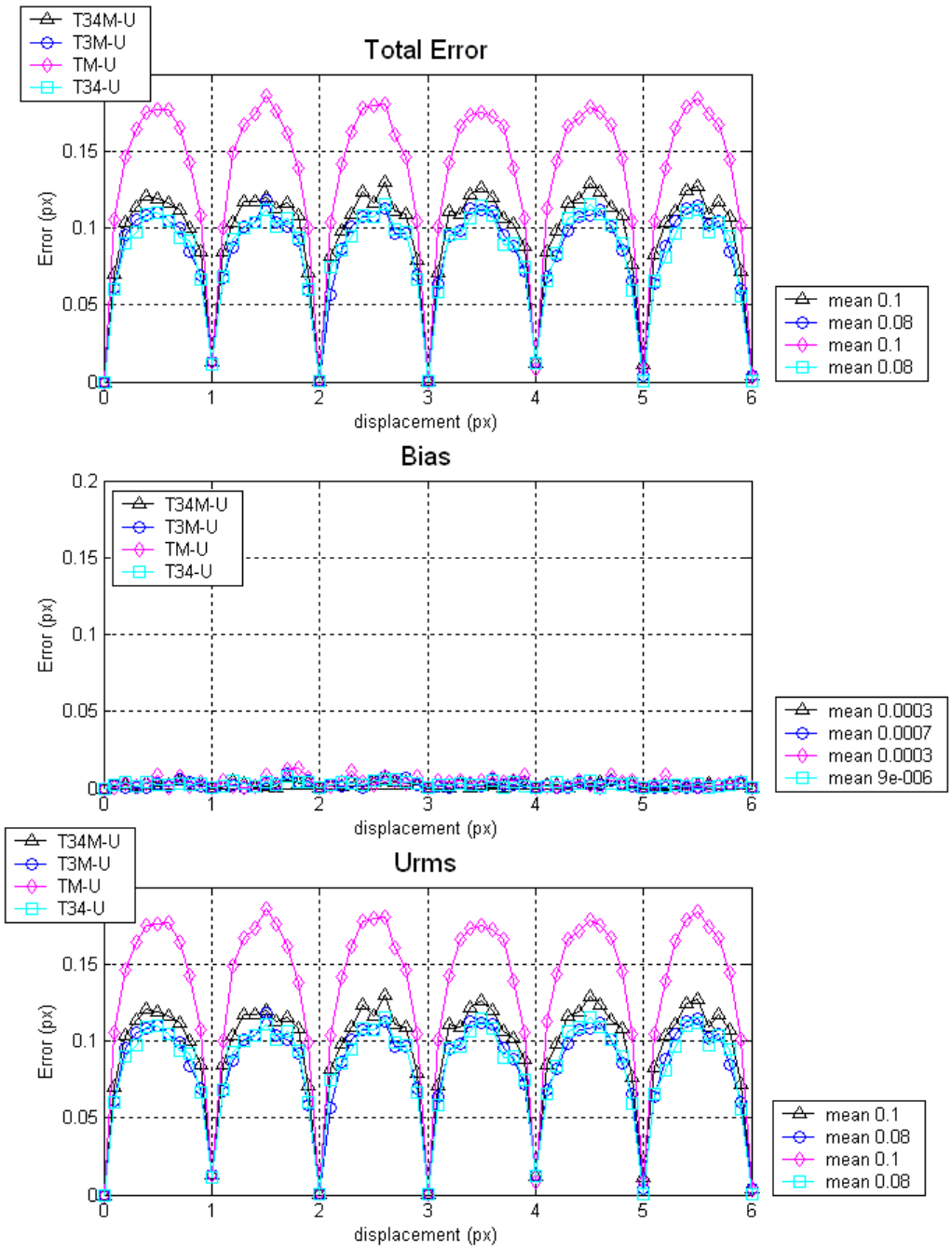

Figure 5.6: Error of several hybrid schemes

5.2.5 Concluding remarks concerning the uniform statistical analyses

In this section, we have seen the uncontestable superiority of schemes that include the dynamic window offset. Our software performs well in every case, although affected by the peak locking effect as shown by the important error that appears for every 0.5 pixels displacement in the Urms error represented in figure 5.5. The peak-locking effect will be discussed later in this chapter. Clearly, Dantec's software presents major implementation weaknesses, although their best results consistently give a better estimation of the flow field. The tracking scheme provides interesting outcomes, even though the centroid estimation might need improvement.

5.3 Comparisons using ALI images

As discussed in chapter two, we chose a graphical approach in order to quantify the error using ALI images. In this case, differences are expected between the different versions. Although rms, bias, and total errors were plotted for two categories of ALI images, the graphical comparison presented here is limited to the total error for ALI images with a maximum displacement of 8 pixels. A table providing the result for all the studied cases is presented in section 5.3.2. The total error was calculated taking into account the x-component of the velocity. Similar results were obtained considering the y-component.

The objective of this type of comparisons was to provide information on both the amplitude of the error and the distribution of this error throughout the flow-field. Indeed, for ALI images, the highest gradient was located in the core of the vortex, so high errors were expected there, as well as at the points were the velocity reaches a maximum, since at this location, the velocity increases, reaches the peak, and then decreases, providing a maximum point along with two different velocity gradients.

5.3.1 Total error

5.3.1.1. OUC (Dynamic adaptive window) scheme

Figure 5.7 represents the error obtained with the adaptive scheme, used by the typical cross-correlation systems. The center of the vortex is easily distinguishable; the error peaks are located at the very center and at high velocity points.

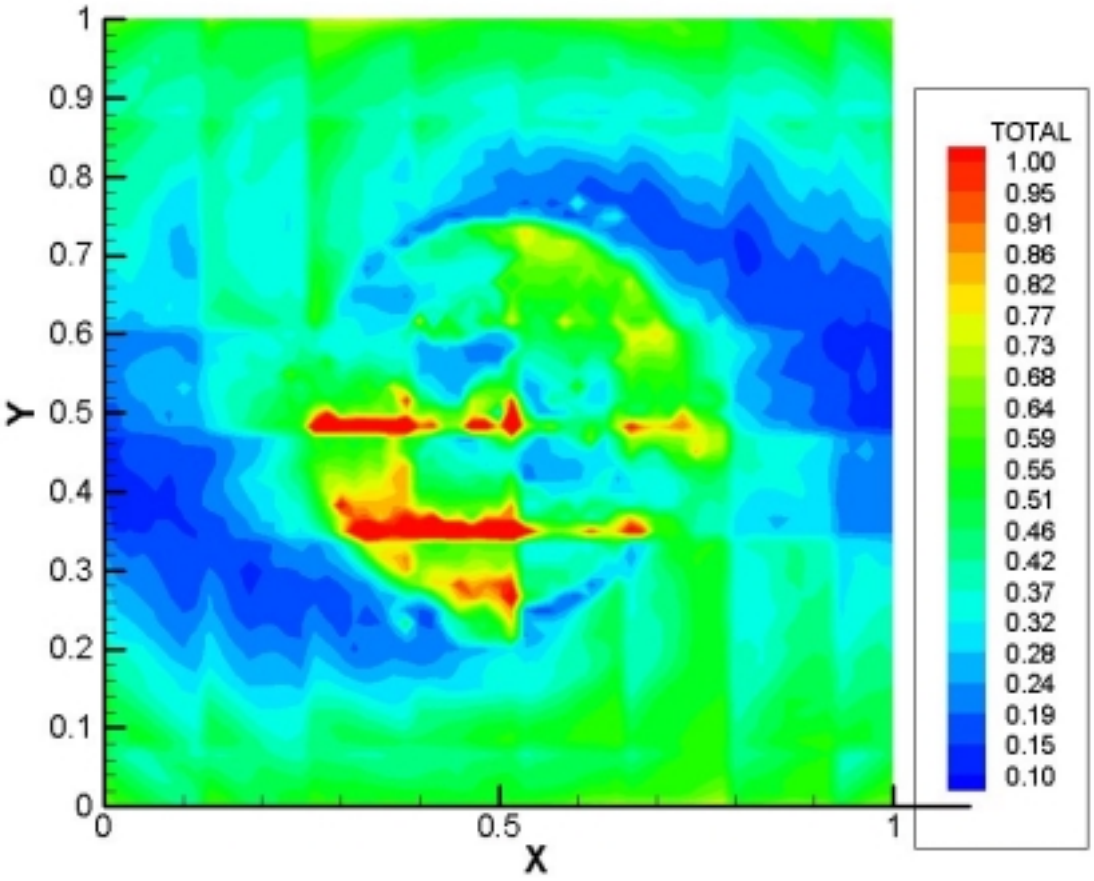

Figure 5.7: Total error with the OUC scheme

Keeping in mind that only the x-component of the velocity is used in this case, the smallest error (blue) is observed where the x-component is small. Indeed for Y=0.5, the expected x-component for the vortex is zero.

5.3.1.2. Error analysis using the DCNH scheme

In this case presented in figure 5.8 the error seems to follow the same pattern as seen above, however it appears to be much higher, especially in the core of the vortex. Curiously, an important error can be observed on the sides of the image, where the velocity gradient is somewhat low and where the velocity is smaller. However, this can be explained considering that the window size used during the first pass is of 64 pixels, which appears to be too big for resolving these small velocities on the sides.

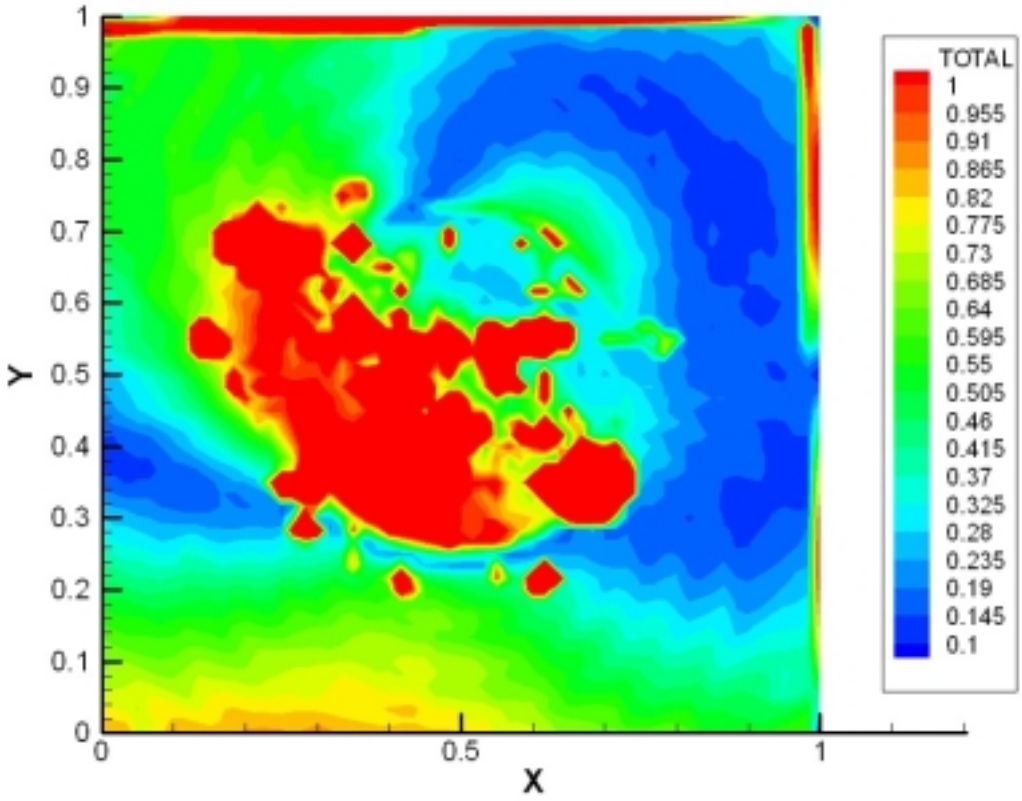

Figure 5.8: Total error for DANH

The error concerning the DCSH scheme although it is not presented here happens to be similar. However, the similarity between the two offsets is probably caused by the implementation mistake pointed out in the first section of the current chapter.

5.3.1.3. Error using the UCN scheme

As shown in figure5.9, this scheme resolves the ALI images much more accurately. The pattern is now somewhat different than that for the two previous cases. This is probably due to the superiority of the "ultimate" scheme, which was expected to outperform the competition for high velocity gradients. The error distribution is astonishingly symmetric, confirming the consistency of the method and the thoroughness of the implementation.

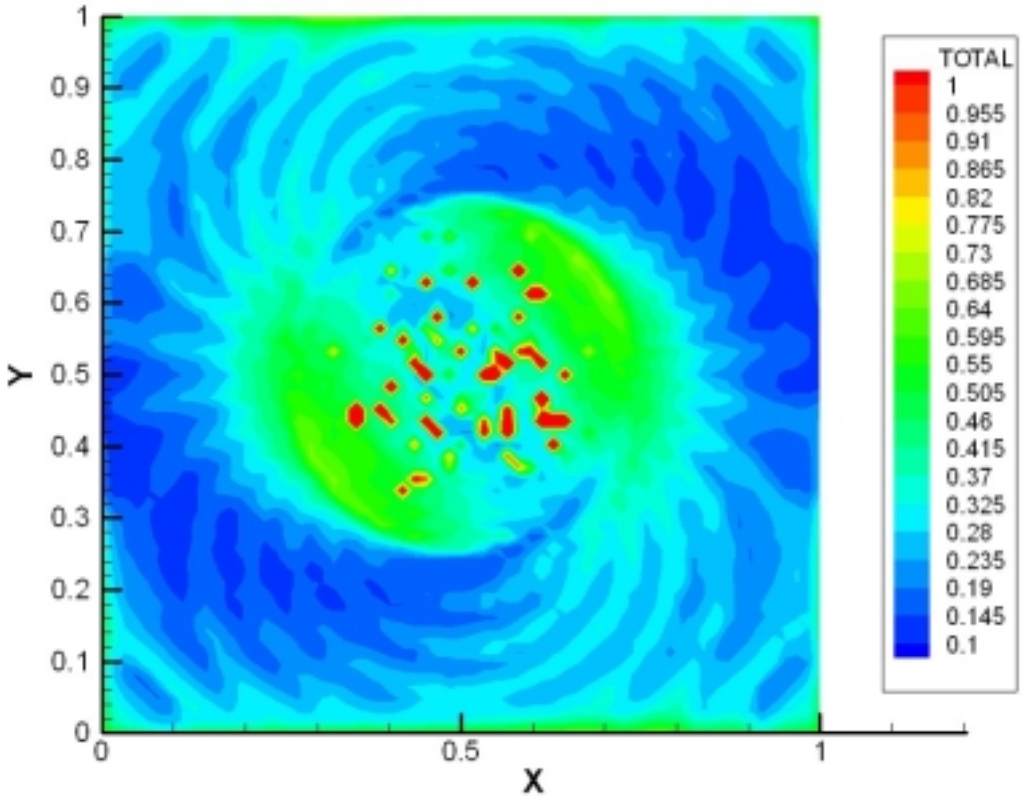

Figure 5.9: Total error for UCN

Some areas with increased error can be noticed in the center of the vortex where the velocity gradient is significant. This reveals the dependence of a method on results from the first window offset. Indeed, in the center of the vortex, the first pass is completed using a size of 64x64 pixels for the interrogation windows. Because of the size of the interrogation window (necessary to resolve the parts of the vortex where the

velocity is high), the first pass cannot resolve small scales that are present at the center of the vortex. Therefore, the first velocity estimation is inaccurate, leading to an error propagation to the final evaluation of the velocity.

5.3.1.4. Total error using the DCSH scheme

This is the scheme that gives the lowest error when averaged over the whole image, as noticeable in figure 5.10. On the sides, the error is similar to the precedent scheme, since they both use the second order offset when the regular one is not applicable. The center of the vortex is recognizable without difficulty, showing that high gradients seriously challenge the cross-correlation schemes.

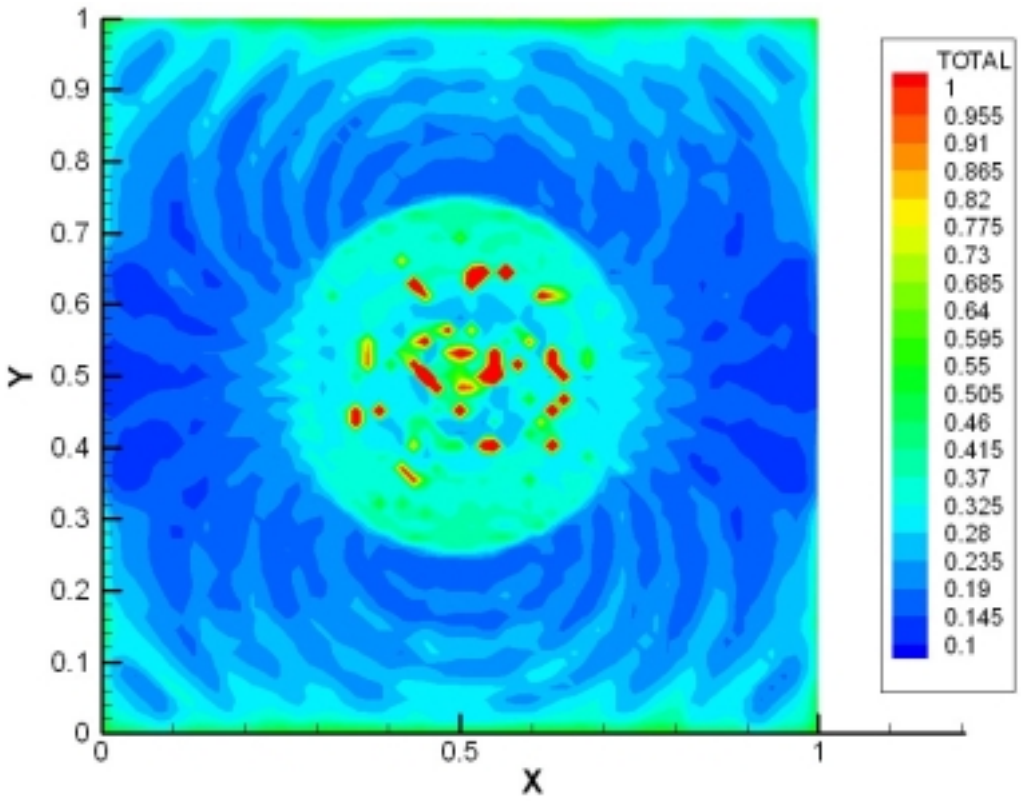

Figure 5.10: Total error for UCS

Overall, the error is very levelheaded, if we disregard some points in the center.

5.3.1.5. Total error using the Hybrid particle tracking

Figure 5.11 establishes the supremacy of the tracking in resolving high gradient flows. The core of the vortex is extremely well defined compared with any other result given by the cross-correlation. Where an error exists around the highest velocity peak, it remains reasonable.

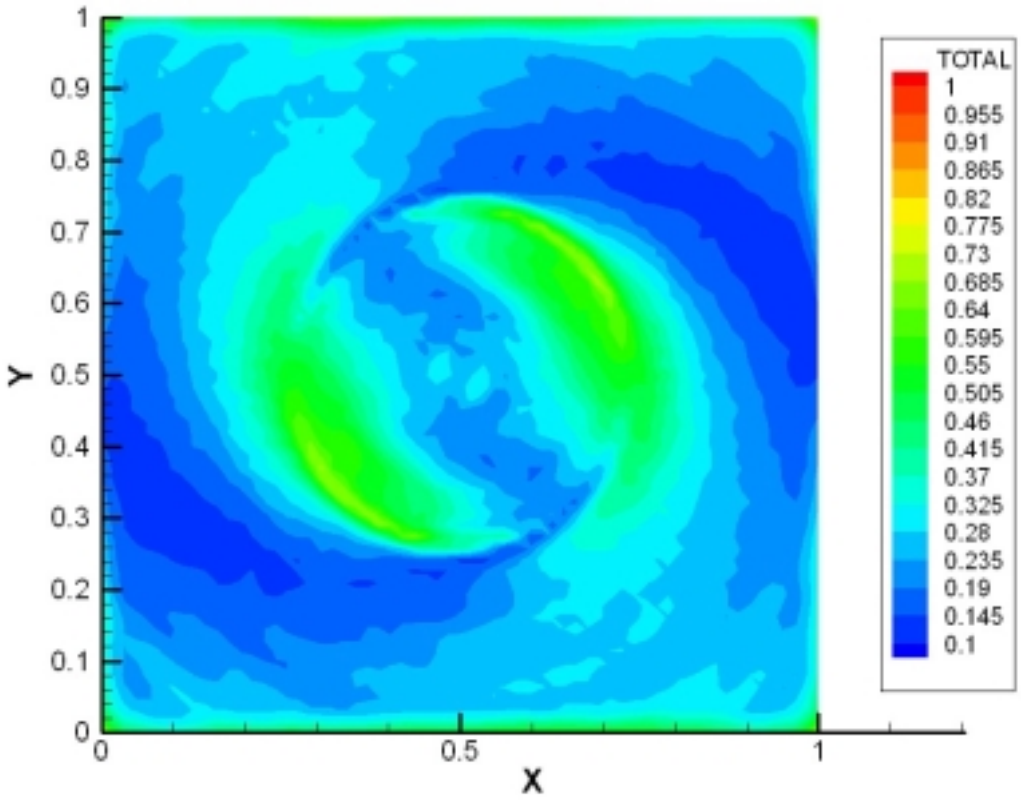

Figure 5.11: Total error with the Hybrid scheme

5.3.2 Overall outcome

Since all the comparisons that were computed could not be inserted in this report, the following tables and figures are aimed to give a global standing of the statistical analyses concerning the ALI images. In these tables, the schemes are sorted by decreasing total error. These results were obtained, as explained in the second chapter of this effort, by averaging the results over the whole flow field, giving a single number that describes the performance of each scheme.

5.3.2.1. ALI images with a maximum displacement of 4 pixels

Table 5.2 presents a collection of the schemes with their corresponding error using ALI images, for a maximum displacement of 4 pixels.

Table 5.2: Errors for several methods

Scheme	RMS	BIAS	TOTAL
GA	0.3383	1.7092	1.7866
DASH	0.1389	0.2059	0.2632
DANH	0.1267	0.2086	0.2584
OUA	0.1312	0.1463	0.2067
UANR	0.1255	0.0918	0.1631
UAN	0.1254	0.0913	0.1627
UAS	0.1253	0.0836	0.1589
T	0.123	0.0889	0.1574

Four groups can be distinguished: the basic cross-correlation, then comes the Dantec's DASH and DANH, followed by the adaptive cross-correlation, and finally, the best results are obtained by the "ultimate" method discussed in this work and the particle tracking. We should point out that the difference principally derives from the Bias error. Therefore, as expected, the "ultimate" strategy seems to significantly improve the outcome of DPIV results in the case of high gradients in the flow.

The highest error (GA standard cross-correlation) was not plotted in Figure 5.12 in order to maintain its clarity.

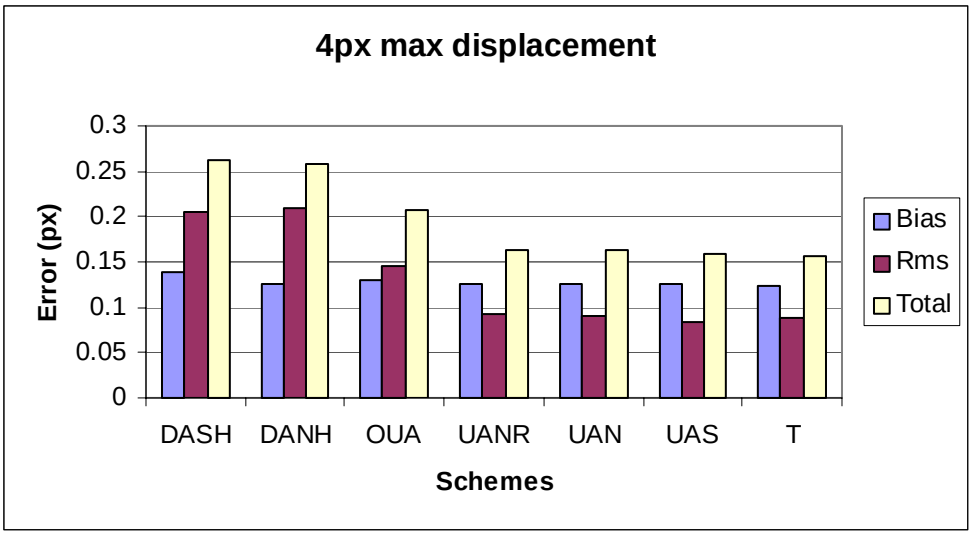

Figure 5.12: Overall error for 4 pixels maximum displacement

Such a plot indicates that neither the second order offset nor windowing strategies seem to present any prevailing breakthrough.

5.3.2.2. ALI images with a maximum displacement of 8 pixels

Table 5.3 confirms the supremacy of the “ultimate” scheme for high velocity gradients. Using images with a higher velocity gradient seems to broaden the gap between the “ultimate” schemes and the previous methods. Indeed, an increase by a factor of three can be observed between the errors given by DCNH and UCS! The adaptive scheme (the core of which is similar to the one used by the ultimate) stands in between Dantec’s and the ”ultimate” methods.

Let’s point out that the second-order offset seems to be prevailing over the standard one, at least when implemented correctly. Therefore figure 5.13 confirms all the expectations that we had during the development of this method: “ultimate” prevails over the standard systems, and the second-order offset performs better than the regular one.

Table 5.3: Error for 8 pixels maximum displacement

Scheme	RMS	BIAS	TOTAL
DCSH	0.3494	0.4364	0.6341
DCNH	0.3576	0.4309	0.6327
OUC	0.2006	0.3245	0.402
UCN	0.1872	0.2178	0.3032
UCNR	0.1853	0.2176	0.3014
T	0.1554	0.2179	0.2775
UCS	0.1872	0.1567	0.2646

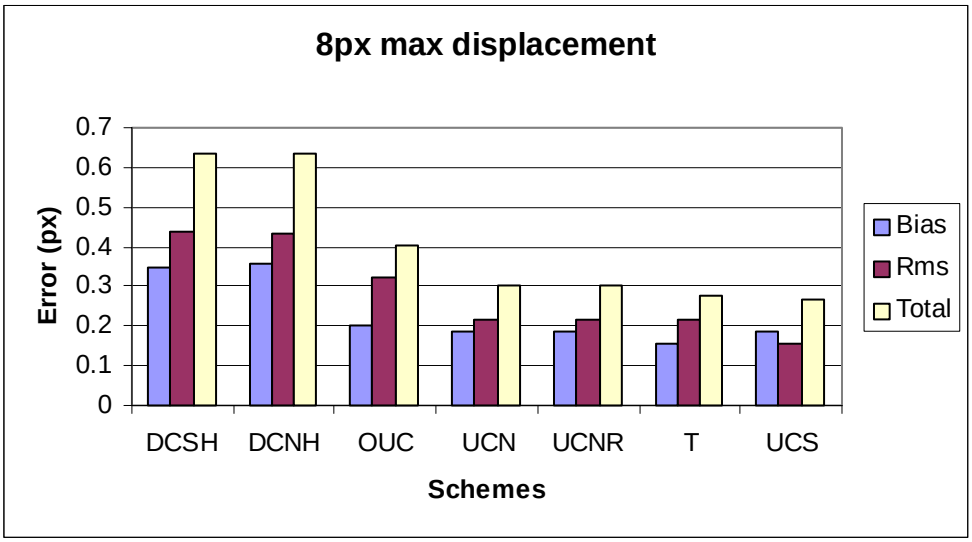

Figure 5.13: Error for 8 pixels maximum displacement

5.4 Peak locking effect

5.4.1 Definition

Right after having cross-correlated two images, it is necessary to estimate the position of the cross-correlation peak in order to determine the displacement. Since a pixel is the smallest unit in a digital image, one could consider reasonable to take the center of the highest intensity pixel as the cross-correlation peak. However, in order to achieve sub-pixel accuracy, not only the highest intensity peak, but also its neighborhood need to be considered. Methods have been developed, like for example Gaussian fit estimators, which provide a better approximation to the peak location. Nevertheless, this last method has a tendency to "lock" on the nearest integer value in the neighborhood of the peak, resulting in erroneous and biased velocity estimations.

Therefore, in order to quantify this effect, we carried out an analysis for our data as well as Dantec's who claim their software is not subject to peak locking.

The procedure for the peak locking estimation is quite straightforward: Based on the results of the uniform displacement images, we scanned each data file for velocities ranging from zero to one pixel displacement. The scale from zero to one pixel was then divided into twenty sections the width of which was 0.05 pixels. The histogram of each velocity value within the intervals was then constructed. Without any peak locking effect, the number of velocities in each section should have been the same.

5.4.2 Results of the analysis

5.4.2.1. Comparison of the general cases

First we performed the analysis considering the general cases: G16, UAN, DANH, and the Hybrid scheme T34M:

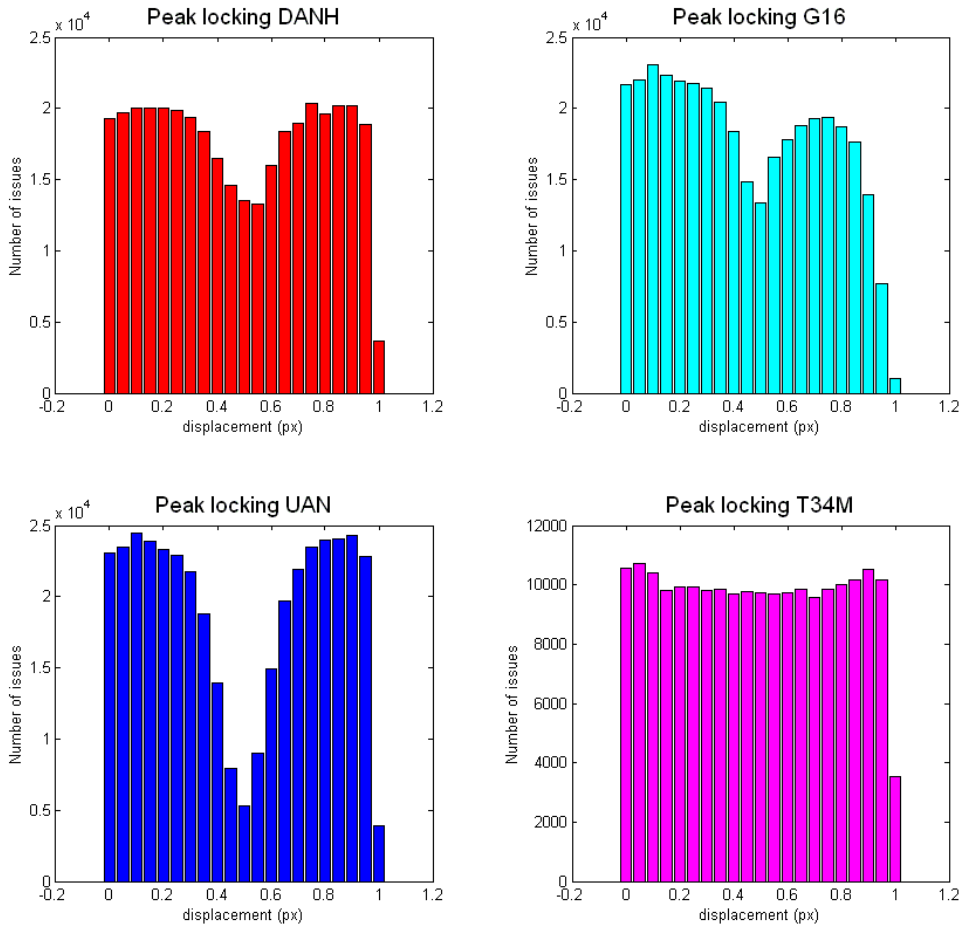

Figure 5.14: Peak locking for general cases

As it can be seen from the above figure, the Ultimate scheme (UAN) is highly affected by the phenomenon, while the hybrid seems totally immune to it, although it uses a centroid estimator as well. The Dantec DANH is also affected, although the high accuracy module was used during this test. Unexpectedly, the basic G16 scheme competes with Dantec's estimation, and performs much better than the ultimate scheme, the core of which is similar to the G16's. Therefore, not only the core of the method, but the whole algorithm seems to affect the peak locking strength. In addition, it can be concluded that the peak locking effect is responsible for the peak found at each 0.5 pixel displacement in the uniform analysis. It also probably explains the differenced between Dantec's results and ours.

5.4.2.2. Comparisons between 16x16 and 8x8

The purpose of this part of the study was to figure out if the peak locking could eventually be related to the size of the interrogation window, as well as to compare different versions of the software.

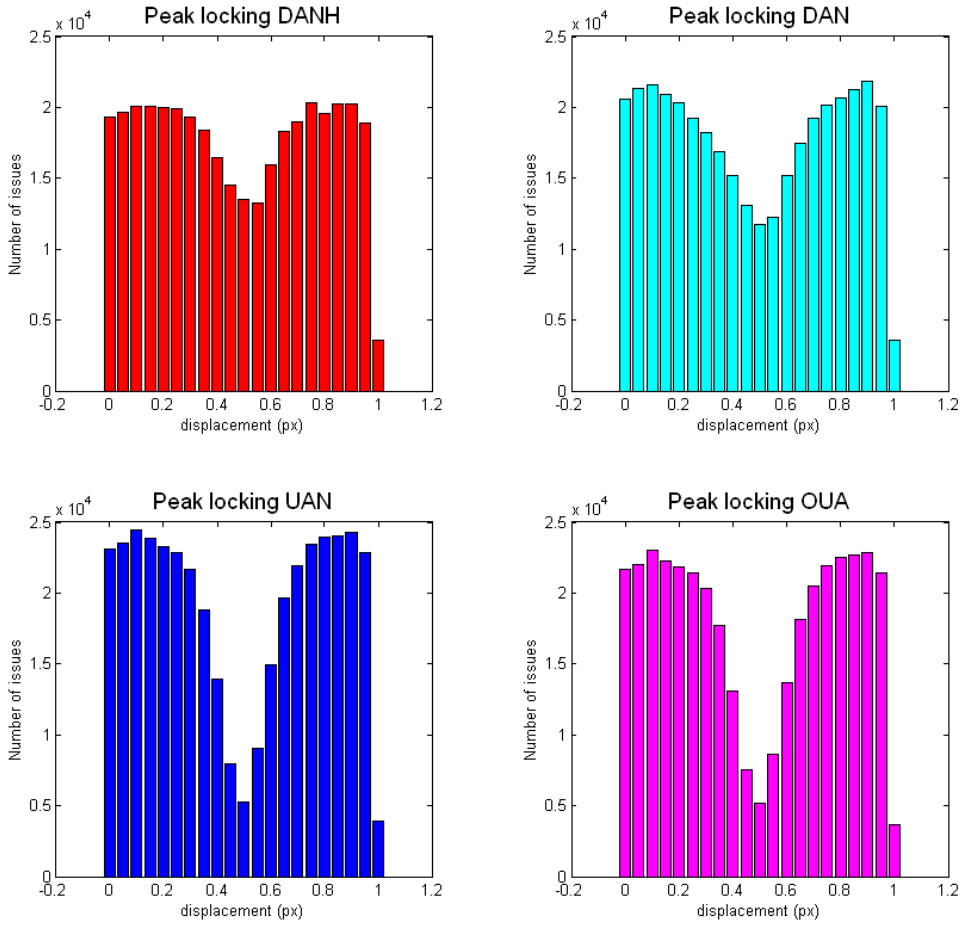

Figure 5.15: Peak locking using16x16 interrogation windows

The plots on the top were obtained using two different versions of the Dantec software. Although the high accuracy module has been advertised as the solution to the peak locking effects, the difference between the two cases seems very small, although the DANH case performs better than the plain DAN.

Comparing our two cases UAN and OUA, practically no difference can be observed, which is consistent since the offset for uniform displacements is the same in both cases. It also shows that this poor performance of our scheme concerning the peak locking is not due to the unique Ultimate scheme, but located in the peak detection algorithm of the correlation peak.

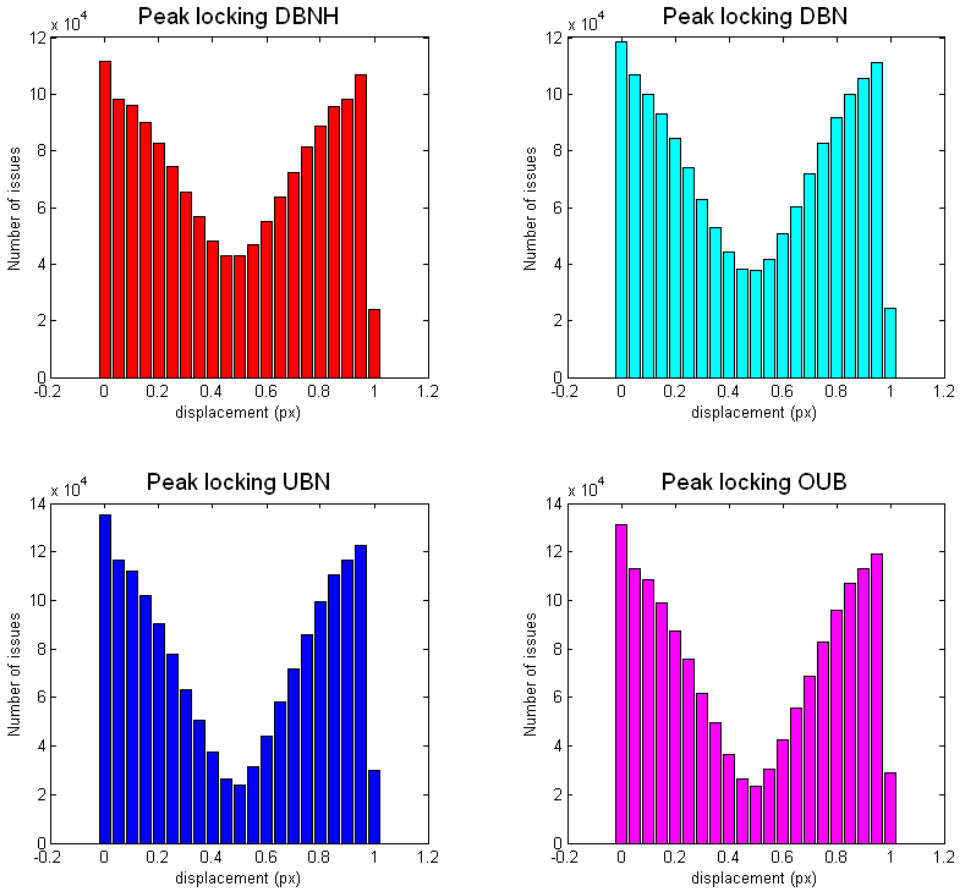

Figure 5.16: Peak locking using 8x8 interrogation windows

The above comparisons could be commented similarly to the prior figure. However, a comparison of these two figures shows that the peak locking effect seems to affect our software equally when using 16x16 and 8x8 windows, while Dantec's schemes don't perform as well using 8x8 windows. Indeed, considering the DANH case (figure 5.15) the maximum number of issues reaches 2.10^4 while the minimum happens to be

$1{,}3.10^4$, giving a ratio of 1.5 from the highest bar to the smallest one. Considering the case DBNH (figure 5.16), this ratio increases up to 3. In the case of our technique,it goes from around 5 for 16x16 windows up to 5.5 for 8x8 windows.

5.4.2.3. Comparison between first and second order offsets

The last comparison we found appealing to develop was between the different offsets. As explained in the third chapter of this work, two different offsets were developed: the plain first order offset, in addition to the second order offset.

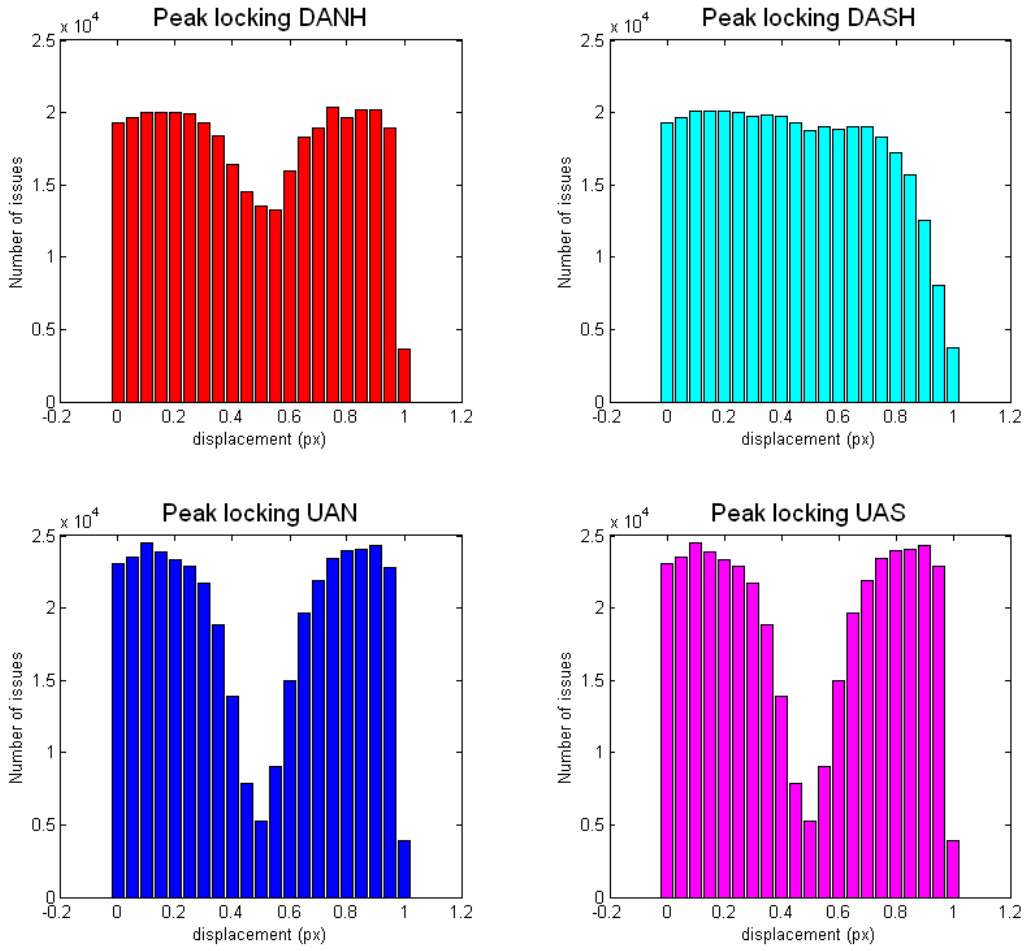

Figure 5.17: Peak locking using normal and second-order offset

The above results show similar results in our case for both offsets. However, in the case of Dantec's, the second offset coupled with the high accuracy module seems to perform remarkably well. However, given the results obtained in the first part of these comparisons, one will remember that the second order offset didn't seem to be well implemented in the case of Dantec's schemes. Therefore, this absence of peak locking might be counter balanced by this error.

5.4.3 Concluding remarks concerning the peak locking effect

In summary, it can be inferred from these analyses that the peak locking effect affects less Dantec's software than our method. In order to reduce the overall current errors of our software,further research in this area might be necessary. Also, velocity evaluation using the tracking is unaffected by this phenomenon, although it also uses a centroid estimator.

Chapter 6 Test cases

6.1 High-speed cavitating Torpedo

6.1.1 Experimental setup

Super-cavitation is a new way to overcome viscous drag resistance and to move underwater bodies with extremely high velocities, sometimes reaching supersonic speeds. The objective is to minimize the amount of wetted surface on the body by enclosing it in a low-density gas bubble. To reach the supercavitating state, high-speed bodies must pass from a first stage of cavitation inception to partial cavitation. Understanding of all phases of cavitation is thus required. Under supercavitating state, a single bubble or supercavity is formed that envelops the moving object completely. With slender axisymmetric bodies, supercavities take the shape of elongated ellipsoids, beginning at the blunt forebody and trailing behind, with the length dependent on the speed of the body. The resulting elliptically shaped cavities soon close up and separate under the pressure of the surrounding water. The flow over a super cavitating projectile involves intrinsically complicated flow structures and the interaction of an unsteady cavity with the surrounding fluid (Scientific American, May 2001)

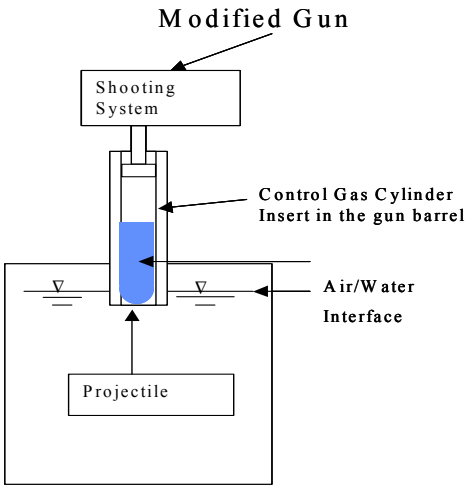

Figure 6.1: Experimental setup.

To improve the understanding of the unsteady behavior of supercavitating flows, we performed an experimental investigation of the flow around an impulsively started underwater projectile This experiment is used to demonstrate the power of the system developed. The experiments were carried out by shooting a fully submerged projectile vertically, in order to avoid any free surface penetration effects. Figure 6.1 shows a schematic representation of the experimental setup. The projectile was fired with initial velocity of approximately 25m/s corresponding to a cavitation index of $\mathbf{C_p}$=0.28 and Reynolds number of 260,000.

6.1.2 Flow visualization

Thanks to the CMOS camera described earlier, the following frames were captured. For this experiment, the frame rate was 10000Hz, however in order to present an optimum displacement of the torpedo within a small amount of frames, we chose to illustrate the phenomenon by means of the following pictures that are separated by 1/5000 sec.

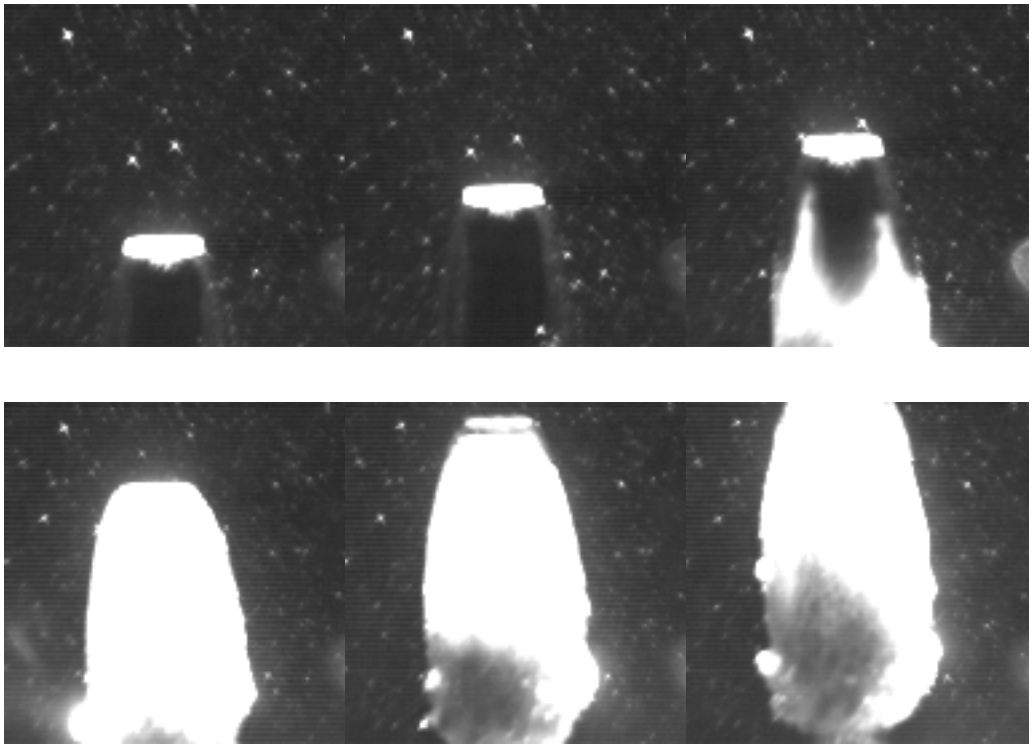

Figure 6.2: High speed cavitating torpedo

Within the above frames, the projectile is clearly visible in the center, surrounded by seeding particles. A cavitation pocket can be distinguished on the bullet's forebody (top of the projectile). On the third frame, the initiation of the supercavitation phenomenon was captured, beginning at the trailing edge. Frame four shows the bullet entirely enclosed in the cavitation bubble. The last two frames presented here give an idea of the cloud left after the projectile has crossed the whole frame.

Several tests were conducted, using different lengths for the bullet, as well as diverse shapes for the forebody, in order to study the behavior of the torpedo under diverse conditions. The above images will be used in order to illustrate the outcome of the cross-correlation scheme. Figure 6.3 illustrate one of the experiments that were carried out.

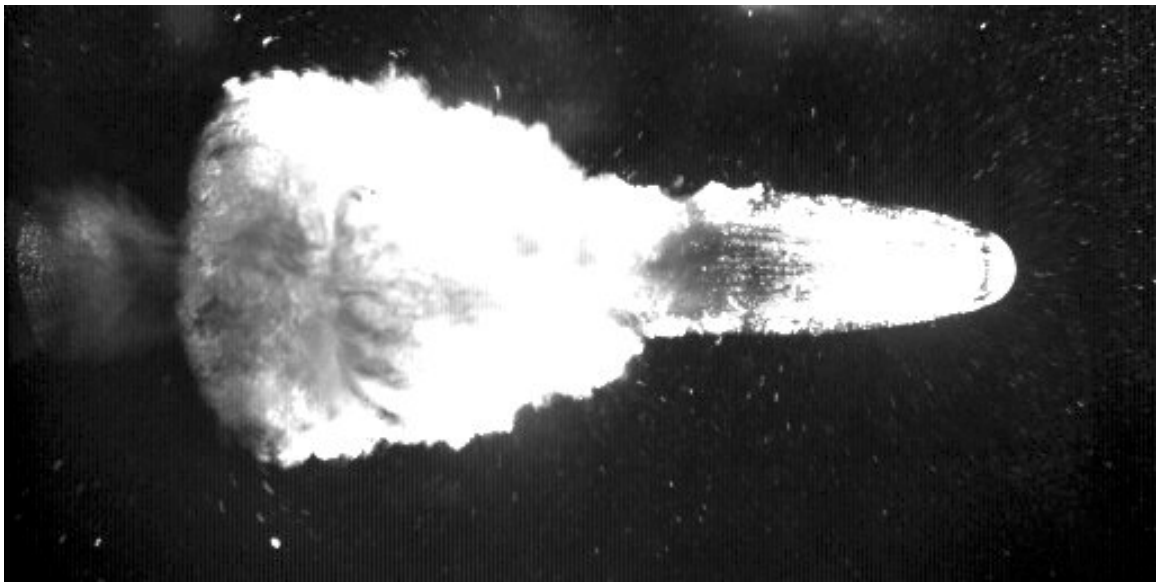

Figure 6.3: Round forebody cavitating torpedo

6.1.3 Cross-correlation using the ultimate off-check scheme

The high- speed, time-resolved Digital Particle Image Velocimetry (PIV) method presented in this work was employed to document the character of the flow with a sampling frequency of 10KHz and a pixel resolution of 256x256 pixels. The ultimate scheme with automatic offset verification was employed to resolve the two-phase flow

velocity distributions and the shape of the cavitation bubble. The speed at which the bullet travels presents a challeng that is accounted for by the CMOS camera. However, the images are hardly fitted for cross-correlation. Indeed, the cavitation phenomenon produces an important amount of steam, that reflects light, introducing noise, clearly visible when comparing the three images at the top of the figure flow visualization presented above with the ones at the bottom. The former appear darker than the latter. Besides the cavitation pocket(s) may introduce erroneous vectors during the cross-correlation process. Pre-processing was employed in the past in order to remove the cavitation bubble. However, this process is delicate in the present case. Indeed, still considering the three top images presented figure 6.2, the forebody of the torpedo is easily detectable; however the same cannot be said about the aft , which is barely different from the rest of the image. Consequently, ordinary cross-correlation systems generate erroneous vectors (that might correspond to the speed of the torpedo itself) that are scarcely detectable by any kind of validation method due to their quantity.

The following flow-fields were directly obtained from the ultimate system with automatic offset validation, without any parasite pre-processing operation. The velocity vectors appear in purple, along with the corresponding cyan streamlines. The presence of saturated pixels due to the large steam pockets, as well as the moving boundaries and the speed of the particles were expected to challenge the method.

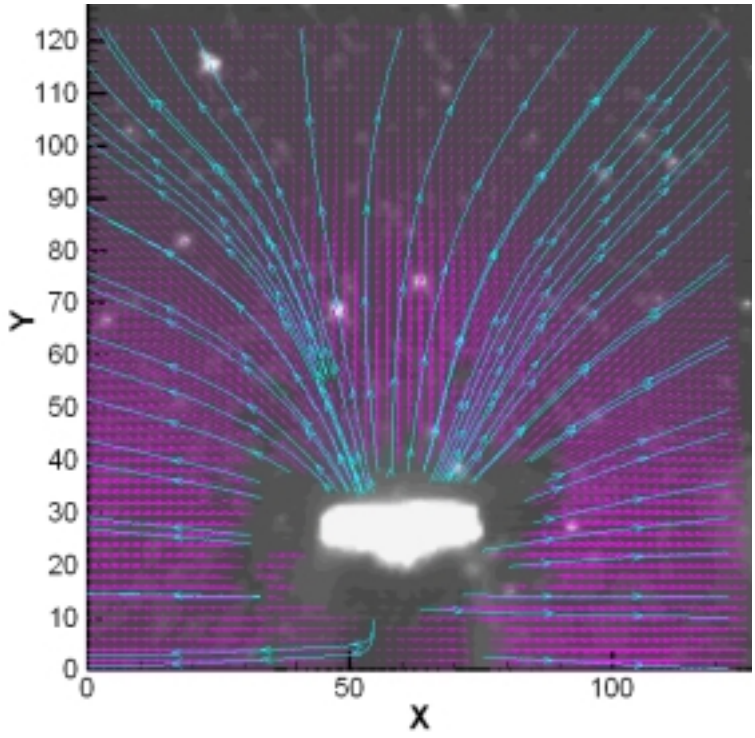

Figure 6.4: Torpedo before it reaches super-cavitation state

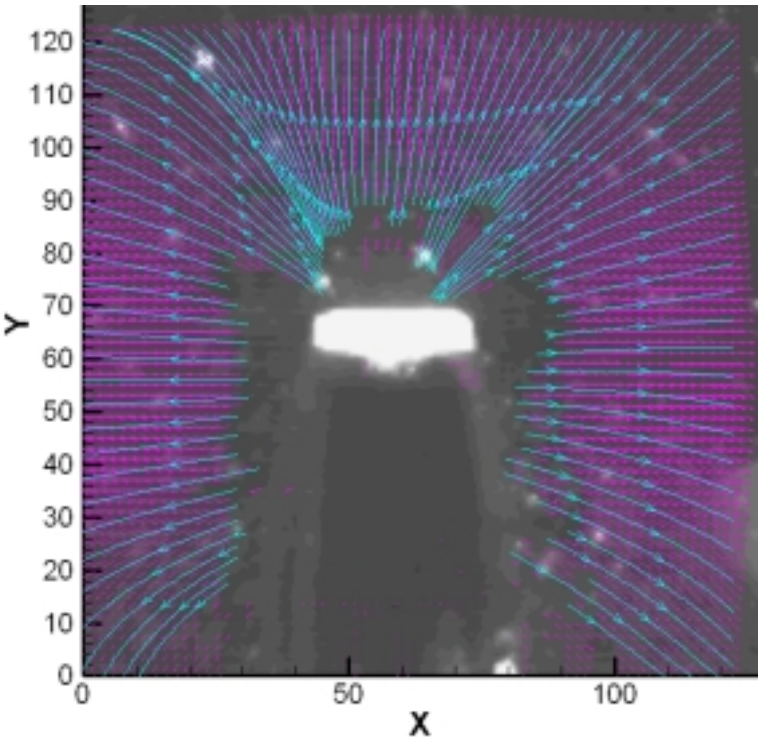

Figure 6.5: Beginning of the curvature of the streamlines

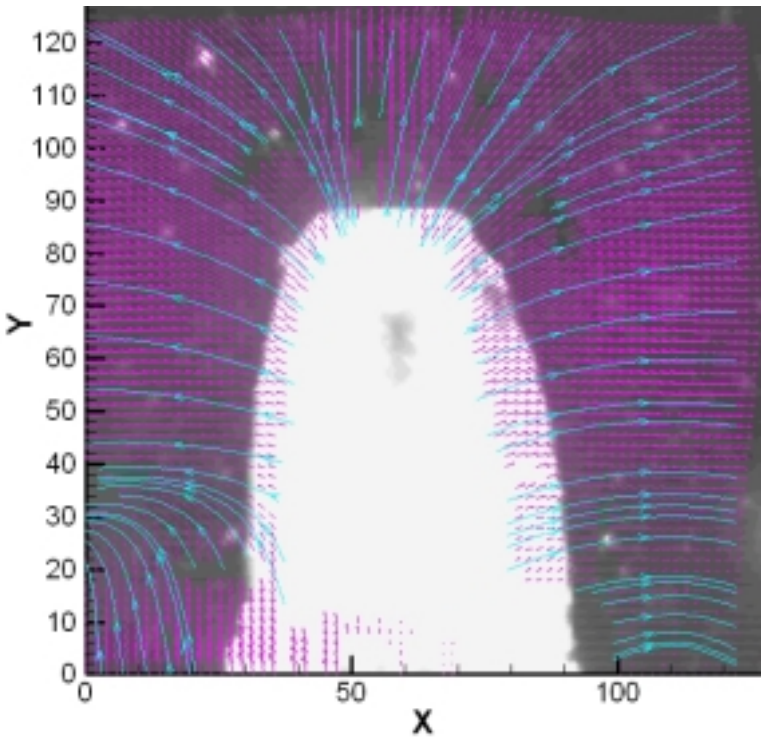

Figure 6.6: Torpedo after it has reached super-cavitation state

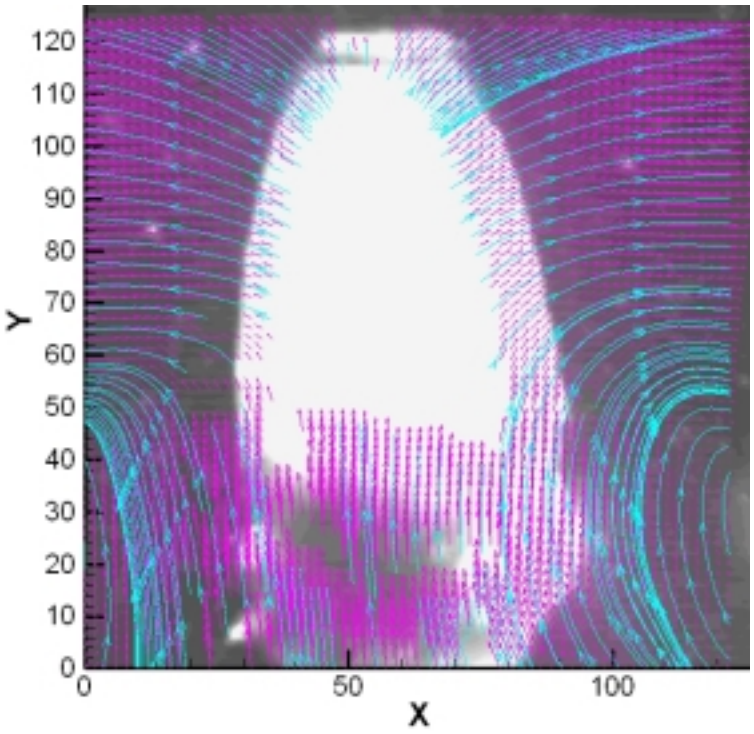

Figure 6.7: Formation of the system of vortices

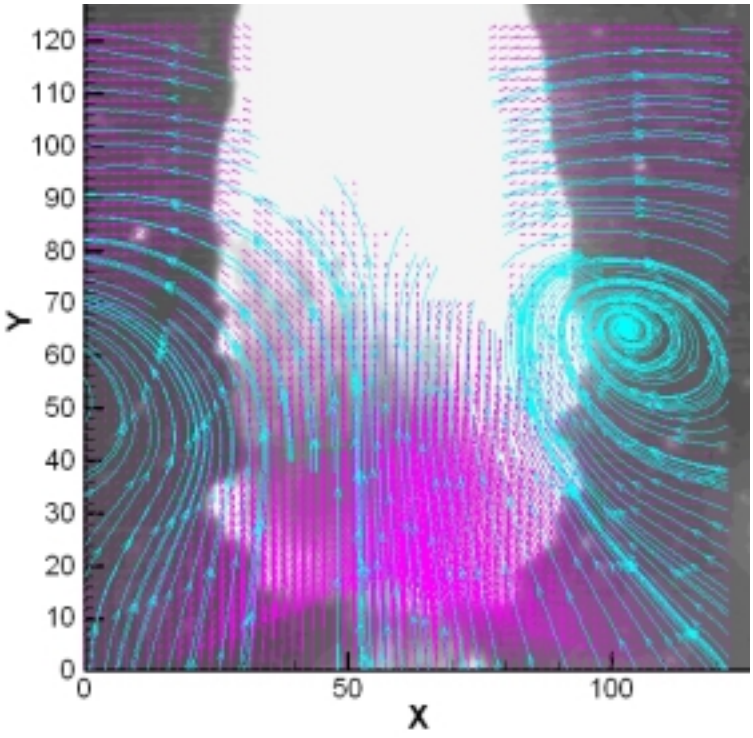

Figure 6.8: The vortices go up and get closer to each other

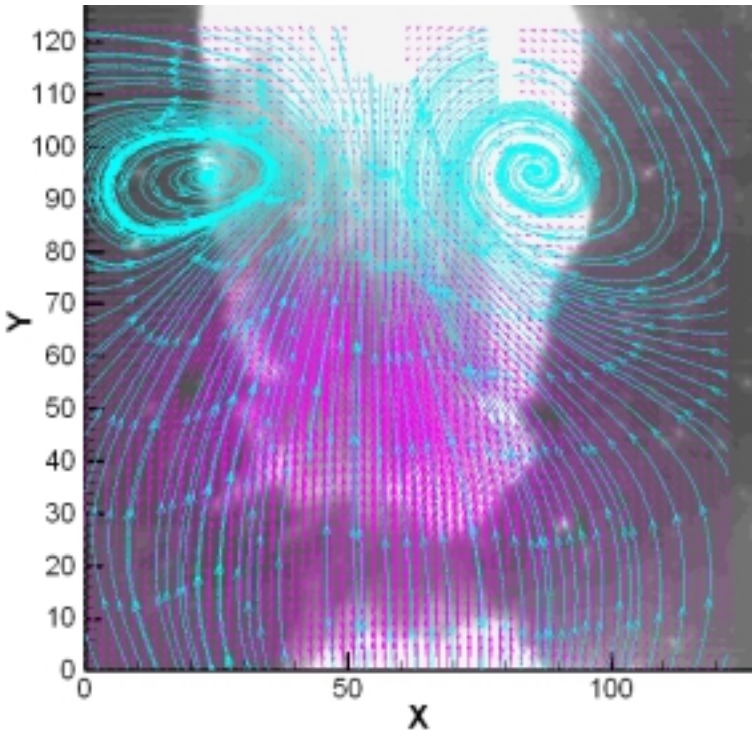

Figure 6.9: Cloud left by the bullet

This experiment shows the power of the proposed methodology, which automatically detects the erroneous offsets due to the presence of steam, in conjunction with an automatic choice of the window size in order to correctly compute the offset value.

6.2 Spray atomization experiment

6.2.1 Experimental setup

The second case is a spray atomization experiment, recorded with 10KHz sampling rate by employing a similar experimental setup. The high-pressure spray was generated using a 60deg cone angle nozzle and a pressure of approximately 10Psi was applied. A low-speed, annular co-flow was introduced but was not seeded. In addition the spray was dynamically driven with a frequency of 10Hz. The objective of this pilot experiment was to demonstrate the ability of the system to resolve a poly-dispersed distribution by resolving the individual velocities of the droplets.

6.2.2 Challenges and corresponding strategy

Due to the feeble amount of tracers (that are the droplets themselves) visible within the original images, together with the presence of parasite elements that both the cone and the spray ligament represent, this experiment was expected to puzzle the cross-correlation. Indeed, when in presence of a small number of particles, only large interrogation windows can be employed in order to obtain a reasonable signal. Therefore, this jeopardizes the resolution of small velocity variation scales. Moreover, and similarly to the case involving the torpedoes, confusion between the cone and actual particles by the cross-correlation can be anticipated, originating erroneous velocities.

Therefore, the following strategy was employed: first, image-processing tools were employed in order to dispose the parasite elements that were background noise, cone and ligaments. Although the number of remaining particles was small, a cross-correlation was performed using these pre-processed images, so as to provide an initialization for the tracking. Finally, the hybrid DPTV was employed with the purpose

of furnishing velocity estimations for most of the particles present in the flow. In this case, DPTV and DPIV are thus applied in favor of a common objective. The only aim of the DPIV process being the initialization for the tracking, while the DPTV method is employed due to its capability of resolving smaller length scales or more exactly of detecting higher velocity gradients in the present case.

6.2.3 Pre-processing of the images

Figure 6.10 shows the original image. The bright pixels at the bottom are not particles but cone and ligaments. A glance at figure 6.11 shows that the original image contains a significant presence of background noise. Using the histogramming method described in chapter two, this background noise is automatically removed, without altering the tracers, and without any guess by the user. This step generates the image shown in figure 6.12

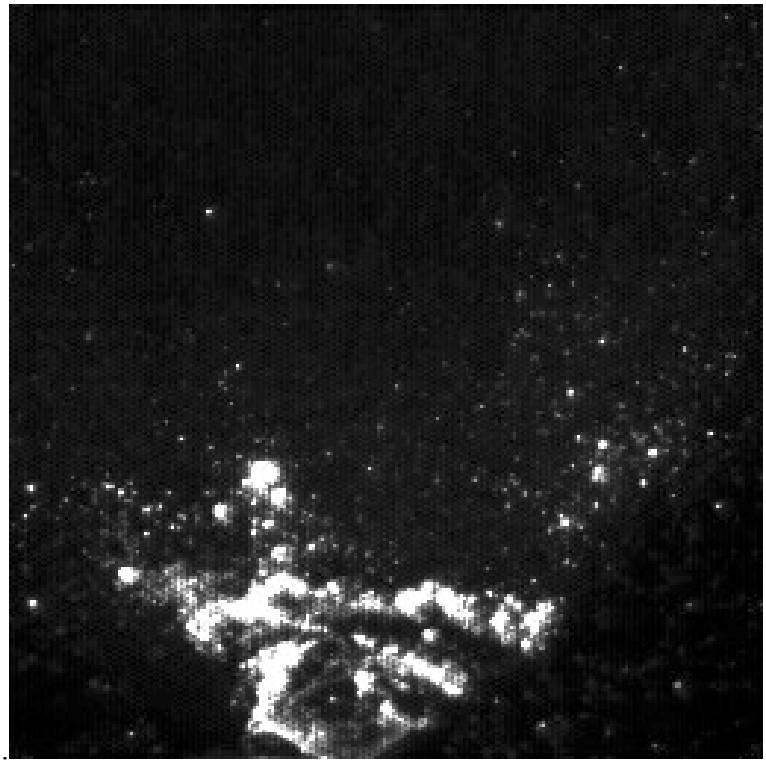

Figure 6.10: Original image

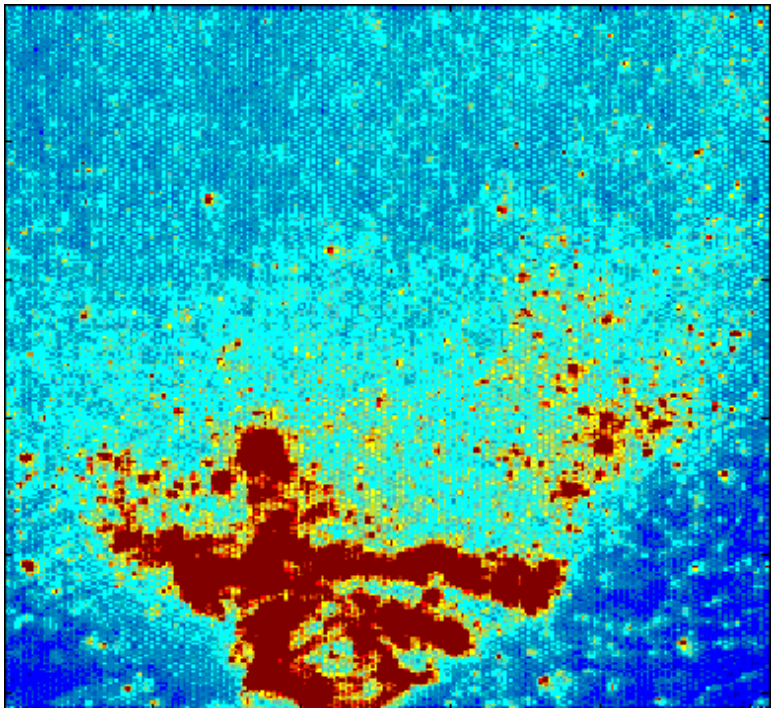

Figure 6.11: Original image (with noise made visible)

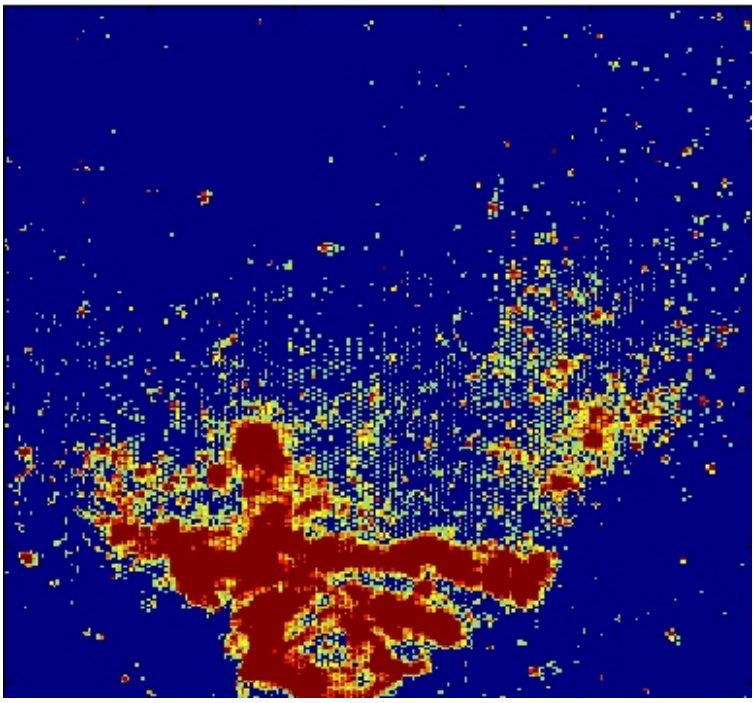

Figure 6.12: Same image after noise removal

The second step consisted in removing the cone and the spray ligament, which appear like a big particle at the bottom of the image. This was performed by taking advantage of the big particle segmentation feature, as well described in the second chapter of the present work. Thus, a final image was obtained, noise free and only containing useful information. This image is presented in figure 6.13.

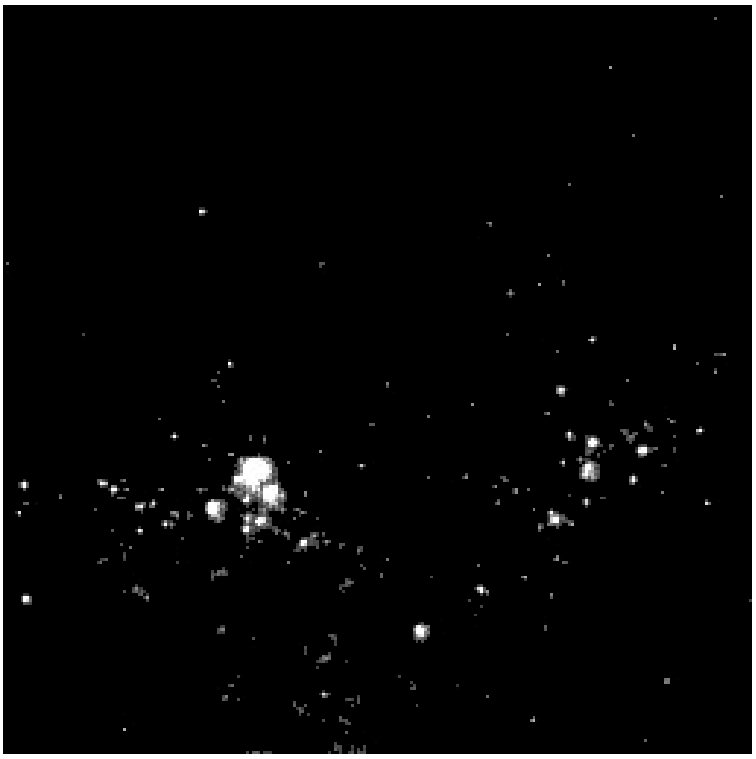

Figure 6.13: Image after pre-processing

Once a pre-processing scheme has been found to properly resolve one image, every image from the same data set can be processed following the same method. This is then performed automatically without any intervention whatsoever by the user, enabling an unbiased result.

6.2.4 Cross-correlation analysis

The pairs of images were then processed using the usual ultimate cross-correlation procedure.

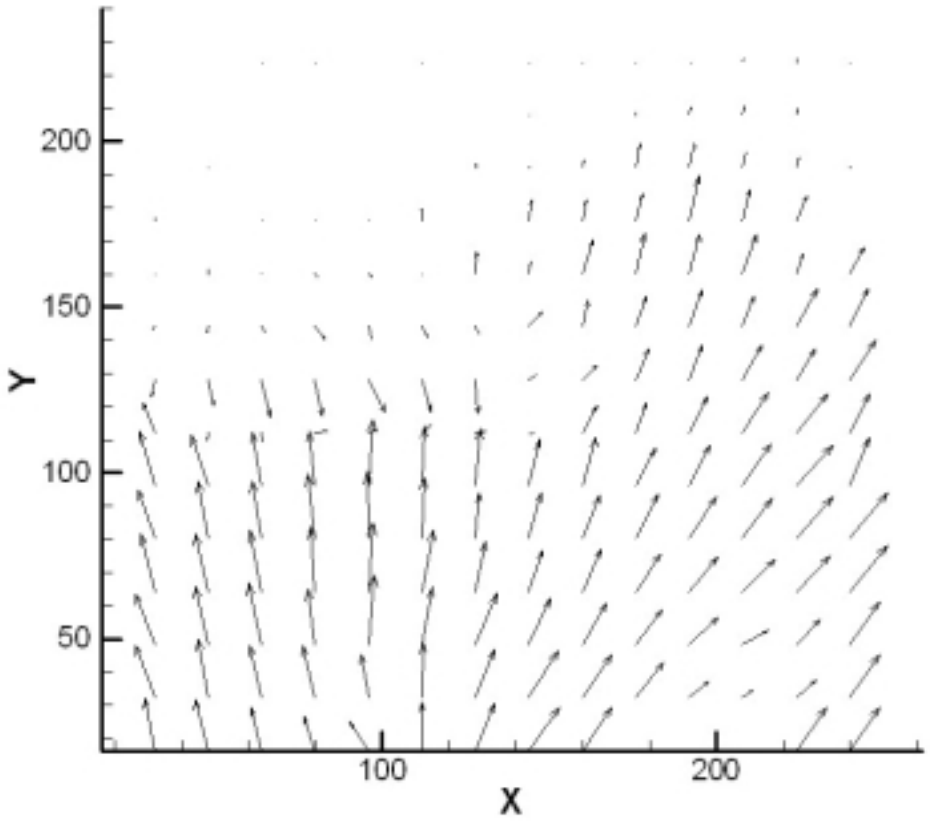

Figure 6.14: Cross-correlation outcome

The first pass interrogation window length was chosen to be 64x64 pixels, due to the lack of particle in the flow-field. A second pass with the same window length was elected (the second pass takes advantage of the dynamic window offset), and a refinement using 32x32 pixels window length finalized the routine. Because of the obligation to use large window sizes due to the lack of particles, the cross-correlation does not resolve small scales, resulting in an imprecise flow-field.

6.2.5 Hybrid DPTV scheme

A flow-field containing few particles can be treated taking advantage of the DPTV technique.

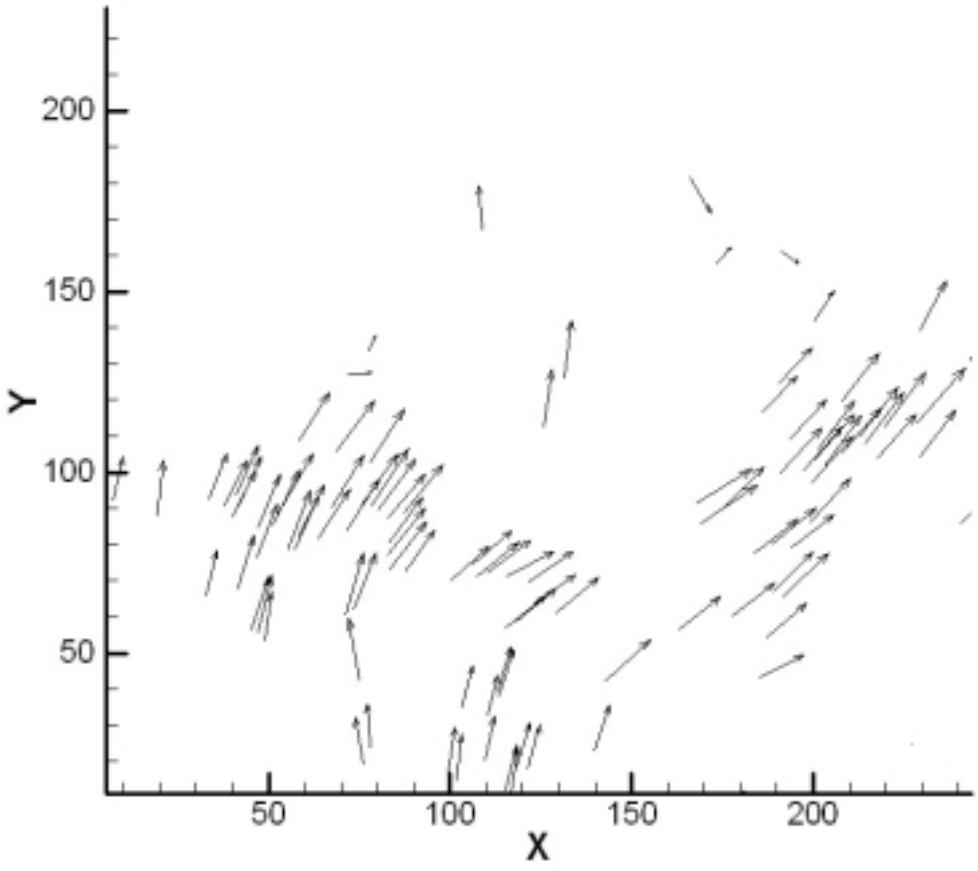

Figure 6.15: Spray results using the particle tracking

The above figure was generated using the previously described hybrid particle-tracking scheme, initialized with the outcome of the cross-correlation showed earlier. The flow appears much smoother and much more consistent than the results given by the cross-correlation. The velocities of all the paired droplets can be plotted with the intensity of the spray overlapped, as shown in the following figure. The vectors are colored with apparent cross-sectional area of the droplet.

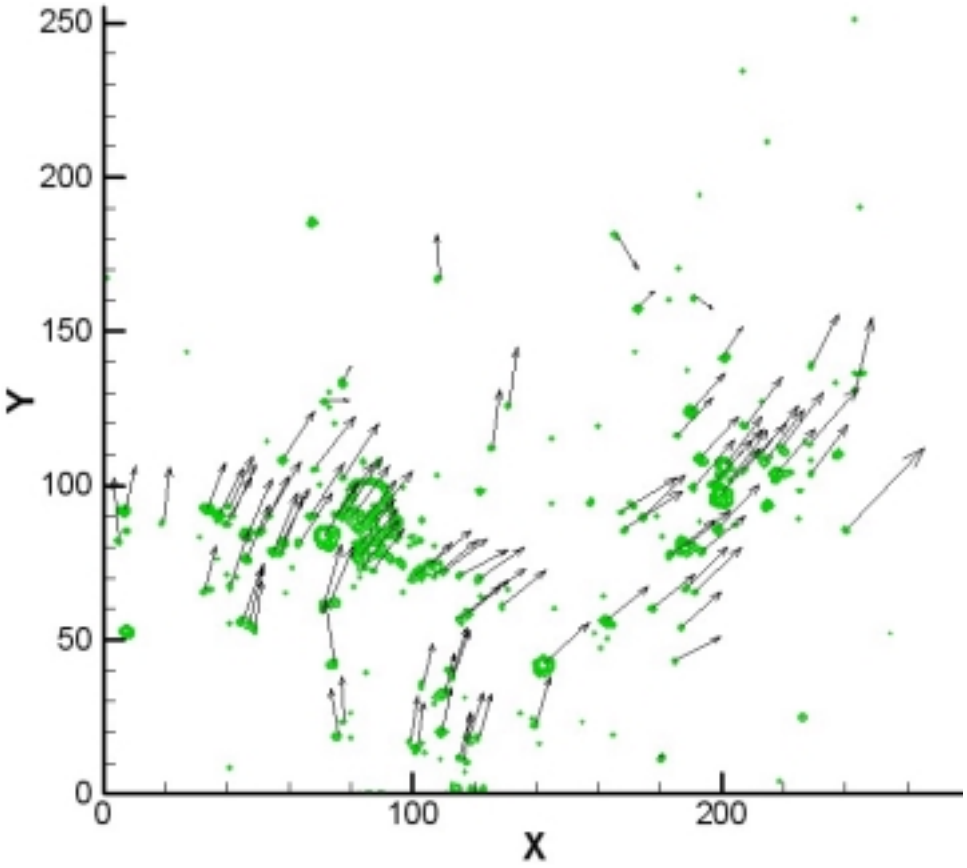

Figure 6.16: Particle tracking

It is worth mentioning that since we were sampling with 10KHz, we were able to measure a 1KHz frequency of the break-up. From these analyses, we deduced that larger droplets appear to have smaller velocities. These results illustrate the feasibility of performing high frequency, time-resolved planar velocity and size measurements with a poly-dispersed two-phase flow.

Chapter 7 Conclusions and future work

7.1 Conclusions

Original methods in terms of Digital Particle Velocimetry and hybrid Particle Tracking Velocimetry have been developed. A new way of implementing DPIV was presented, providing flexibility, transparency, and accuracy to the method.

Starting from a very basic cross-correlation scheme, common features inherent to usual DPIV schemes were implemented, including dynamic window offset and dynamic adaptive windowing, as well as validation, interpolation and smoothing methods, providing a robust and high-performing tool.

Significant improvements were brought to the method when incorporating an arsenal of image-processing tools to the package, thus enabling multiphase-flows to be computed by processing each phase independently. Additional features such as second order offsets were successfully implemented. Moreover, the use of a neural network as a post-processor for validating the cross-correlation outcome represented a considerable advancement.

The major improvements that were discussed throughout this effort have effect at the very core of the DPIV method, which happens to be critical for the global performance of the system, reducing the number of stray vectors thus minimizing the need of validation, data filtering and interpolation schemes. Any sort of interrogation mesh can be generated, making possible to accurately resolve flows containing several phases such as flows with droplets or bubbles. The use of a specific offset at each point of the mesh was proved to provide much better accuracy in addition to limiting the effect of an incorrect offset evaluation. Moreover, a solution was proposed in order to resolve this last issue.

A Hybrid DPTV system was also developed, including standard tracking routines, as well as a cross-correlation-based scheme that enables hybrid Digital Particle Tracking Velocimetry to take place without any interpolation. Using CMOS camera technology, an innovative way of computing particles centroids has been demonstrated, making it possible to determine the centroid of a particle even when in presence of saturated pixels. In addition, using image processing along with a maximum intensity filter, particle identification was made much more precise, enabling one to distinguish clustered particles that an ordinary scheme would not distinguish.

These schemes have been successfully validated by statistical analyses proving that they reach the best levels in DPIV standards. The ability of the method to resolve multi-phase flows a well as challenging high-speed cavitating flows has also been demonstrated.

7.2 Future work

Concerning the cross-correlation, two major points of interest have been identified throughout the completion of this effort: reducing the peak-locking effect, and improving the resolution of multiple length scales in a same flow-field. Although the methods discussed in the present effort tackle this issue, enhancements might be promising in this area.

The first problem might be treated by the completion of a “real offset” instead of an “integer offset”. Indeed, since the smallest scale used in digital imaging is the pixel, it doesn’t seem conceivable to shift an image by a non-integer number of pixels. However, using image re-sampling, it might be possible to do so. The issue is to know if the error introduced by re-sampling the image would be smaller than the error originated by shifting a pixel to the nearest integer instead of the real corresponding displacement. However, if it happened to be so, the peak-locking effect might be alleviated, and at the same time, the overall error would considerably drop.

In order to resolve multiple length scales, it might be useful to try automatically different window sizes in order to define the window offset correctly. Two ways might be

considered. The first and more straightforward way was presented in the scope of this work, but still needs further research and improvement: after having determined the offset from a first pass, the result of the second pass is validated only if the resulting displacement is found to be smaller than one pixel as it should. The second approach would be to compare the cross-correlation peak as an indicator of the success of the cross-correlation.

Regarding the particle tracking, the principal issues at stake remain the particle identification together with the centroid location. An enhancement in the definition of close particles would significantly improve the method.

References

1) Adrian RJ, Yao C-S (1985): Pulsed laser technique application to liquid and gaseous flows and the scattering power of seed materials. *App Optics, 24, 44-52*.

2) Adrian RJ (1991): Particle-Imaging techniques for experimental fluid mechanics. *ARFM, 23, 261-304.*

3) Adrian RJ, Meinhart CD, Barnhart DH and Papen GC (1995): An HPIV System for turbulence research. EP Rood (ed.), *ASME FED, 148,17-21.*

4) Adrian RJ (1996): Bibliography of Particle Velocimetry using imaging methods. *TAM Report. Produced and distributed in cooperation with TSI Inc.*

5) Adrian, R. J. (1996): Strategies for Imaging Flow Fields with PIV. *AIAA 96-1988*

6) Adrian, R. J. (1997): Dynamic Ranges of Velocity and Spatial Resolution of Particle Image Velocimetry. *Meas. Sci. Technol. 8 1393-1398.*

7) Agui J. and Jimenez J. (1987): On the performance of particle tracking. *J. Of Fluid Mechanics vol 185 pp 447-468*

8) Asimopoulos N, Vlachos P. P. Telionis D. P (1999): A high speed, high particle density particle tracking method for turbulent flows. *ASME FEDSM'99-7139.*

9) Boedec T, Simoens S (2001): Instantaneous and simultaneous planar velocity field measurements of two phases for turbulent mixing of high pressure sprays. *Experiments in Fluids, 31, 506-518*.

10) Boillot A. and Prasad K. (1996): Optimization procedure for pulse separation in cross-correlation PIV. *Exp. In Fluids 21 87-93, Springer Verlag.*

11) Carosone F. & A. Cenedese (1996): Image Analysis for velocity evaluation and Neural Networks. *VKI Lecture Series 1996-03*

12) Cenedece A. Paglialunga A. (1990): Digital direct analysis of a multi-exposed photograph in PIV. *Exp. in Fluids 8, 273-280.*

.

13) Cowen B and Monismith S (1997): A hybrid digital particle tracking velocimetry technique. *Experiments in Fluids, 22, 199-211*

14) Dalziel SB (1993): Decay of rotating turbulence: Some particle tracking experiments. FTM Nieuwstadt (ed.). *Flow Visualization and Image Analysis, 27-54*

15) Damaschke N, Nobach H, Tropea C (2002): Optical limits of particle concentration for multi-dimensional particle sizing techniques in fluids mechanics. *Experiments in fluids, 32, 143-152.*

16) Derou & Herault (1994): A new paradigm for particle tracking velocimetry based on graph theory and pulsed neural networks. *7th Int. Symp. Appl. Laser Techniques to Fluid Mechanics, Lisbon, pp: 35.3.1-35.3.8*

17) Dracos Th. and A. Gruen (1998): Videogrammetric methods in velocimetry. *Appl. Mech. Rev. vol. 51, no. 6 1998*

18) Grant I (1997): Particle Image Velocimetry: A Review. *Proceedings Institute of Mechanical Engineers*

19) Grant and Pan (1995): An Investigation of the performance of multi layer neural networks applied to the analysis of PIV images. *Experiments in Fluids, pp 159-166.*

20) Grant I (1994): Selected papers on Particle Image Velocimetry. *SPIE Milestone Series MS99, SPIE Optical Engineering Press, Bellingham, Washington*

21) Guezennec YG and Kiritsis N (1990): Statistical investigation of errors in particle image velocimetry. *Experiments in Fluids, 10, 138-146*.

22) Hammache M. & Gharib M. (1991): An experimental study of the parallel and oblique vortex shedding from circular cylinders. *J. Fluid Mech., vol. 232 pp. 567-590*

23) Hasselinc L. (1988): Digital Image Processing in Flow Visualization. *ARFM 20:421 85*

24) Huang H. T. and Gharib M. (1997): Processing Error in Digital Particle Image Velocimetry. *FEDSM97-3068.*

25) Huang, H. T. D. Dabiri and Gharib, M. (1997): On Errors of digital particle image velocimetry. *Meas. Science and Technology, .8, 1427-1440*.

26) Jahne B. (1991): Lectures in Computer Science. *Spatio-Temporal Image Processing. Springer-Verlag.*

27) Jahne B. (1997): Image Processing for Scientific Applications. *CRC Press*

28) Keane R. D. and Adrian R. J. (1990): Optimization of particle image velocimeters . Part I: Double pulsed systems. *Meas. Sci. Tech. 1 1202-1205.*

29) Keane R. D. and Adrian R. J. (1991): Optimization of particle image velocimeters . Part I: Multiple pulsed systems. *Meas. Sci. Tech. 2 963-974.*

30) Khalitov DA, Longmire EK (2002): Simultanous two-phase PIV by two-parameter phase discrimination. *Experiments in Fluids, 32, 252-268*.

31) Lecordier B and Trinite M (1999): Time resolved PIV measurements for high speed flows. *Third International Workshop on Particle Image Velocimetry. (Santa Barbara, 16-18 Sept 1999).*

32) Lourenco L.M. (1996): Particle Image Velocimetry, *Von Karman Institute Lecture Series, 1996-03.*

33) Meynard R. (1983): Measure de champs de vitesse d' ecoulements fluids par analyse de suites d'images obteneues par diffusion d'un fueillet lumineux. Ph.D Dissertation, Faculte des Science Appliquees, Universite Libre de Bruxelles.

34) Mostafa, N., Nayfeh, A. H., Vlachos, P. P., and Telionis, D. P. (2001): Cavitating flow over a projectile. *AIAA 39th Aerospace Sciences Meeting and Exhibit, Reno, NV*.

35) Prasad A. K. Adrian R. J., Landreth C.C., Offutt P.W.:(1992): Effect of resolution and accuracy of particle image velocimetry interrogation. *Exp. In Fluids 13 105-116, Springer Verlag.*

36) Prasad A.K. and Adrian R J (1993): Stereoscopic particle image velocimetry applied to liquid flows. *Experiments in Fluids 15, 49-60*.

37) Press, Teukolsky, Vetterling, Flannery. (1992): Numerical Recipes in C: The Art of Scientific Computing, Second Edition. *Cambridge University Press.*

38) Raffel M., Willert C.E. and Kompenhans J. (1998): Particle Image Velocimetry: A practical guide. *Series in Experimental Fluid Mechanics. Springer Verlag.*

39) RJ Perkings and JCR Hunt (1989): Particle Tracking in Turbulent Flows. *Advances in Turbulence 2 pp. 286-291.*

40) Robinson O. Rockwell D. (1993): Construction of three-dimensional images of flow structure via particle tracking techniques. *Experiments in Fluids 14, 257-270*

41) Scarano F. Rieuthmuller M.L. (1999): Iterative multigrid approach in PIV image processing with discrete window offset. *Exp. In Fluids 26 513-523, Springer-Verlag.*

42) Upatnieks A., Laberteaux K., Ceccio S. L. (2002):A kilohertz frame rate cinematographic PIV system for laboratory-scale turbulent and unsteady flows. *Experiments in Fluids, 32, 87-98.*

43) Utami T. and Ueno T.(1984): Visualization and picture processing of turbulent flow. *Experiments in Fluids 2, 25-32, Springer-Verlag.*

44) Vlachos P. P, Donnelly M. J. Telionis D. P. (1998): On the Wake of a Circular Cylinder Piercing the Free-Surface. *FEDSM'98-5177.*

45) Vlachos, P. (2000): A spatio-temporal analysis of separated flows over bluff bodies using quantitative flow visualization. *PhD. Dissertation, Department of Engineering Science and Mechanics, Virginia Polytechnic Institute and State University, Blacksburg, VA.*

46) Wereley ST, Meinhart CD (2001): Second-order accurate particle image velocimetry. *Experiments in Fluids, 31, 258-268.*

47) Westerweel J (1997a): The effect of a discrete window offset on the accuracy of cross-correlation analysis of digital PIV recordings. *Exp. In Fluids 23 20-28, Springer Verlag.*

48) Westerweel J. (1993a): Digital Particle Image Velocimetry, Theory and Application. *Delft University Press*

49) Westerweel J. (1993b):Optical Diagnostics in fluid and thermal flow. *SPIE 2005 624-35*

50) Westerweel J. (1997b): Fundamentals of Digital Particle Image Velocimetry. *Meas. Sci. Technol. 8 1379-1392.*

51) Whybrew A, Reeves M, Slagle RL, Boaler JJ, Baughan AK, Nicholls TR, Towers DP, Tavender B, Buckberry CH (1999): Two techniques for all-digital time-resolved PIV. *Third International Workshop on Particle Image Velocimetry. (Santa Barbara, 16-18 Sept 1999)*

52) Willert C E and M Gharib (1991): Digital Particle Image Velocimetry. *Experiments in Fluids 10, 181-193 1991*

53) Wung T. S. and Tseng F. G. (1992): A color-coded particle tracking velocimeter with application to natural convection. *Experiments in Fluids 13, 217-223*

54) Wung T.S (1997): Quantitative visualization of 2D and 3D flows using a color-coded particle tracking velocimetry. *Atlas of Visualization III edited by The Visualization Society of Japan.*

VITA

Claude Abiven was born in January 17, 1977, in Rennes, France. He earned an Engineering degree from the National Polytechnic Institute of Grenoble, France, in July 2000. In the spring of 2000, he completed an internship as a research assistant in the fluids mechanics laboratory of Virginia Tech. This experience led him to enroll in Virginia Tech in the spring of 2001